PREPARATION, CHARACTERIZATION, AND PROPERTIES OF ACTINOSCIRPUS GROSUSS-DERIVED SiO$_2$ NANOPARTICLES

ANUCHIT SAWANGPROM

A Thesis Submitted in Partial Fulfillment of the Requirements for the
Degree of Doctor of Philosophy in Physics
Suranaree University of Technology
Academic Year 2023

การเตรียม การอธิบายลักษณะ และคุณสมบัติอนุภาคนาโนซิลิกอนไดออกไซด์จากกกสามเหลี่ยม

นายอนุชิต สว่างพรม

วิทยานิพนธ์นี้เป็นส่วนหนึ่งของการศึกษาตามหลักสูตรปริญญาวิทยาศาสตรดุษฎีบัณฑิต
สาขาวิชาฟิสิกส์
มหาวิทยาลัยเทคโนโลยีสุรนารี
ปีการศึกษา 2566

PREPARATION, CHARACTERIZATION, AND PROPERTIES OF ACTINOSCIRPUS GROSUSS-DERIVED SiO_2 NANOPARTICLES

Suranaree University of Technology has approved this thesis submitted in partial fulfillment of the requirements for the Degree of Doctor of Philosophy

Thesis Examining Committee

(Prof. Dr. Supree Pinitsoontorn)
Chairperson

(Prof. Dr. Santi Maensiri)
Member (Thesis Advisor)

(Assoc Prof. Dr. Worawat Meevasana)
Member

(Dr. Narong Chanlek)
Member

(Dr. Ittipon Fongkaew)
Member

Yupaporn

(Assoc Prof. Dr. Yupaporn Ruksakulpiwat)
Vice Rector for Academic Affairs
and Quality Assurance

(Prof. Dr. Santi Maensiri)
Dean of Institute of Science

อนุชิต สว่างพรม : การเตรียม การอธิบายลักษณะ และคุณสมบัติอนุภาคนาโนซิลิกอนไดออกไซด์ จากกกสามเหลี่ยม (PREPARATION, CHARACTERIZATION, AND PROPERTIES OF ACTINOSCIRPUS GROSUSS-DERIVED SiO_2 NANOPARTICLES) อาจารย์ที่ปรึกษา : ศาสตราจารย์ ดร.สันติ แม้นศิริ, 131 หน้า

คำสำคัญ: อนุภาคนาโนซิลิกอนไดออกไซด์, การชะล้างด้วยกรดไฮโดรคลอริก, การชะล้างด้วยกรดไนตริก

งานวิทยานิพนธ์นี้มุ่งเน้นการสกัดซิลิกอนไดออกไซด์บริสุทธิ์สูงจากกกสามเหลี่ยม ด้วยการชะล้างด้วยกรดแก่ ได้แก่ ไฮโดรคลอริก (HCl) และกรดไนตริก (HNO_3) การศึกษาครอบคลุมกระบวนการเตรียม การเกิดเฟส ปริมาณความบริสุทธิ์ ลักษณะอสัณฐานของอนุภาคระดับนาโน และรูปร่างของโครงสร้างซิลิกอนไดออกไซด์ ในการทดลองนี้ขั้นตอนการสกัดแบ่งเป็น 2 วิธี คือ 1. การสกัดซิลิกอนไดออกไซด์โดยการชะล้างกกสามเหลี่ยมด้วยกรดไฮโดรคลอริก และ 2. การสกัดซิลิกอนไดออกไซด์ที่มีความบริสุทธิ์สูงโดยการชะล้างขี้เถ้าซิลิกอนไดออกไซด์ด้วยกรดไฮโดรคลอริกและกรดไนตริก

การศึกษาการสกัดซิลิกอนไดออกไซด์โดยชะล้างกกสามเหลี่ยมด้วยกรดไฮโดรคลอริก ใช้ความเข้มข้น 0, 0.1, 0.5, 1, และ 5 โมลาริตี โดยชะล้างที่อุณหภูมิ 90 องศาเซลเซียสในระยะเวลา 3 ชั่วโมง สำหรับการเลือกอุณหภูมิของการเผาแคลไซด์ได้ทำการเลือกโดยใช้การทดสอบการเปลี่ยนแปลงเชิงความร้อนด้วยเทคนิค TGA/DSC ในช่วง 30 ถึง 950 องศาเซลเซียส จากการวิเคราะห์ผล เปลี่ยนแปลงของมวลวัสดุและปฏิกิริยาภายในระหว่างทำการเผาโดยพบว่า เมื่อวัสดุทำการดูดความร้อนโครงสร้างของวัสดุเกิดการสลายตัวของพันธะเคมีโดยแบ่งเป็น 3 บริเวณช่วงอุณหภูมิ ช่วงอุณหภูมิ 30-200 องศาเซลเซียสมีการสลายตัวของ โมเลกุลของน้ำและความชื้นในโครงสร้าง ช่วงอุณหภูมิ 200-500 องศาเซลเซียสพบว่ามีการสลายตัวของพันธะของไนโตรเจน (R-N) และพันธะของคาร์บอน (R-C) และช่วงอุณหภูมิ 500-950 องศาเซลเซียส พบว่ามีการสลายตัวของพันธะของคาร์บอน (R-C) ที่ 635 และ 820-850 องศาเซลเซียสในเทคนิคที่ใช้ในการวิเคราะห์นี้มวลของวัสดุมีการเปลี่ยนแปลงน้อยมาก และเริ่มคงที่ในช่วงอุณหภูมิ 650-950 องศาเซลเซียส ดังนั้นในการทดลองเลือกใช้อุณหภูมิการเผาที่ 700 องศาเซลเซียสในระยะเวลา 3 ชั่วโมง

ลักษณะของโครงสร้างของซิลิกอนไดออกไซด์หลังจากการเผาพบว่า เมื่อทำการศึกษาด้วยการเลี้ยวเบนของรังสีเอกซ์ลักษณะของโครงสร้างมีรูปร่างเป็นแบบอสัณฐานของซิลิกอนไดออกไซด์ในตัวอย่างที่ทำการชะล้างด้วยกรด และมีการพบเฟสของโครงสร้างที่เป็นผลึกของซิลิกอนไดออกไซด์ เช่น ควอตซ์ และ คริสโตบาไลต์ ในตัวอย่างที่ทำการชะล้างด้วยกรดที่ความเข้มข้น 1 และ 5 โมลาริตี

ความบริสุทธ์ของซิลิกอนไดออกไซด์หลังจากการชะล้างด้วยกรด ทำการวิเคราะห์ด้วยเทคนิคการวัดปริมาณรังสีเอกซ์ฟูออเรสเซนต์ พบว่าความบริสุทธิ์ของมวลซิลิกอนไดออกไซด์ของตัวอย่างที่ใช้ความเข้มข้นของกรด ไฮโดรคลอริก 1 โมลาริตีมีความบริสุทธิ์ อยู่ที่ 96% รูปร่างของอนุภาคนาโนซิลิกอนไดออกไซด์หลังจากการเตรียมจะมีลักษณะเป็นรูปหลายเหลี่ยม และมีขนาดอยู่ในช่วง 50 ถึง 100 นาโนเมตร ซึ่งทำการวิเคราะห์ด้วยกล้องจุลทรรศน์อิเล็กตรอนแบบส่องกราด และกล้องจุลทรรศน์อิเล็กตรอนแบบส่องผ่าน นอกจากนี้พบการกระจายตัวที่ดีของซิลิกอนบนพื้นผิวของอนุภาค เมื่อทำการวิเคราะห์ด้วยการวิเคราะห์องค์ประกอบทางเคมีด้วยสเปกโทรเมตรีรังสีเอกซ์แบบกระจายพลังงาน และสถานะออกซิเดชันของซิลิกอนในอนุภาคมีสถานะออกซิเดชันคือ Si^{4+} ซึ่งการวิเคราะห์โครงสร้างภายในด้วยเทคนิคการดูดกลืนของรังสีเอกซ์

ในการทดลองนี้ ได้ทำการเพิ่มความบริสุทธิ์ของซิลิกอนไดออกไซด์ด้วยการชะล้างกรดไฮโดรคลอริกและกรดไนตริกในตัวอย่างขี้เถ้าซิลิกอนไดออกไซด์จากวิธีการทดลองที่ 1 โดยใช้ความเข้มข้นของกรดไฮโดรคลอริกและไนตริกที่ 0.1, 0.5, 1, และ 5 โมลาริตี และทำการเผาที่อุณหภูมิ 700 องศาเซลเซียส หลังจากชะล้างด้วยกรด ความบริสุทธิ์ของซิลิกอนไดออกไซด์ถูกวิเคราะห์ด้วยเทคนิคการวัดปริมาณรังสีเอกซ์ฟูออเรสเซนต์ พบว่าตัวอย่างที่ใช้กรดไฮโดรคลอริกมีความบริสุทธิ์อยู่ที่ 99.7-99.8% ในขณะที่ตัวอย่างที่ใช้กรดไนตริกมีความบริสุทธิ์อยู่ที่ 97.0-97.3% โดยความแตกต่างของความบริสุทธิ์เป็นผลมาจากปฏิกิริยาการสร้างและสลายพันธะที่แตกต่างกันของไฮโดรคลอริก และไนตริก ผลการชะล้างด้วยกรดทั้งสองชนิดทำให้อนุภาคมีรูปร่างทรงกลมและขนาดของอนุภาคเพิ่มขึ้นตามความเข้มข้นของกรด โดยตัวอย่างที่ชะล้างด้วยกรดไฮโดรคลอริกมีขนาดอนุภาคอยู่ที่ 60-160 นาโนเมตร และตัวอย่างที่ชะล้างด้วยกรดไนตริกมีขนาดอนุภาค 100-150 นาโนเมตร ซึ่งวิเคราะห์ได้จากกล้องจุลทรรศน์อิเล็กตรอนแบบส่องกราดและส่องผ่าน

นอกจากนี้ โครงสร้างภายในของอนุภาคซิลิกอนไดออกไซด์แสดงสถานะออกซิเดชันของซิลิกอนเป็น Si^{4+}ซึ่งยืนยันได้จากการวิเคราะห์ด้วยเทคนิคการดูดกลืนรังสีเอกซ์ในตัวอย่างที่ชะล้างด้วยกรดไฮโดรคลอริกและไนตริก

สาขาวิชาฟิสิกส์	ลายมือชื่อนักศึกษา__________
ปีการศึกษา 2566	ลายมือชื่ออาจารย์ที่ปรึกษา__________

ANUCHIT SAWANGPROM : PREPARATION, CHARACTERIZATION, AND PROPERTIES OF ACTINOSCIRPUS GROSUSS-DERIVED SiO_2 NANOPARTICLES. THESIS ADVISOR : PROF. DR. SANTI MAENSIRI, D.PHIL. 131 PP.

Keyword: SILICONDIOXIDE NANOPARTICLES, ACTNOSCIRPUS GROSSUS ,HYDROCHLORIC LEACHING, NITRIC LEACHING, CHARACTERIZATION, X-RAY ABSORPTION SPECTROSCOPY

This thesis focuses on the extraction of high-purity silicon dioxide from Actinoscirpus Grossus using acid leaching with strong acids, specifically hydrochloric acid (HCl) and nitric acid (HNO_3). The study covers the preparation process, phase formation, purity level, amorphous characteristics of the nanoparticles, and possible structures of silicon dioxide. In this experiment, the extraction process was divided into two methods: 1. Extraction of silicon dioxide by leaching Actinoscirpus Grossus with hydrochloric acid. 2. Extraction of high-purity silicon dioxide by leaching silicon dioxide ash with hydrochloric acid and nitric acid.

The study on the extraction of silicon dioxide from Actinoscirpus Grossus by acid leaching with hydrochloric acid was conducted using concentrations of 0, 0.1, 0.5, 1, and 5 molars, with leaching performed at 90°C for 3 hours. The calcination temperature was determined using thermogravimetric analysis/differential scanning calorimetry (TGA/DSC) tests, which covered a temperature range from 30 to 950°C. Based on the analysis of mass changes and internal reactions during calcination, it was found that as the material absorbed heat, its chemical structure underwent bond dissociation in three distinct temperature regions. In the range of 30–200°C, water molecules and moisture in the structure decomposed. Between 200–500°C, nitrogen (R-N) and carbon (R-C) bonds dissociated, while further dissociation of carbon bonds occurred at 635°C and between 820–850°C in the range of 500–950°C. During this process, the material's mass changed minimally and stabilized within the 650–950°C range. Therefore, a calcination temperature of 700°C for 3 hours was selected for the experiment.

The structure of the silicon dioxide after calcination, studied using X-ray diffraction, revealed that the material exhibited an amorphous structure when leached with acid. In samples leached with 1 and 5 molar concentrations of acid, crystalline phases of silicon dioxide, such as quartz and cristobalite, were detected. The purity of silicon dioxide after acid leaching was analyzed using X-ray fluorescence (XRF), and it was found that samples leached with 1 molarity of hydrochloric acid had a silicon dioxide purity of 96%. The shape of the silicon dioxide nanoparticles after preparation was polygonal, with sizes ranging between 50 to 100 nanometers, as analyzed by scanning electron microscopy (SEM) and transmission electron microscopy (TEM). Furthermore, the silicon particles showed good dispersion on the surface, as determined by energy-dispersive X-ray spectroscopy (EDS), and the oxidation state of the silicon in the particles was Si^{4+}, confirmed through X-ray absorption spectroscopy (XAS).

In this experiment, the purity of silicon dioxide was enhanced by acid leaching with hydrochloric acid and nitric acid, applied to silicon dioxide ash samples from experimental method 1. The concentrations of hydrochloric and nitric acids used were 0.1, 0.5, 1, and 5 molars, and the samples were calcined at 700°C. After acid leaching, the purity of the silicon dioxide was analyzed using X-ray fluorescence (XRF). It was found that the samples treated with hydrochloric acid achieved a purity of 99.7–99.8%, while those treated with nitric acid reached a purity of 97.0–97.3%. This difference in purity is attributed to the distinct bonding formation and dissociation reactions of hydrochloric and nitric acids. The acid leaching with both acids produced spherical particles, and particle size increased with acid concentration. Samples treated with hydrochloric acid had particle sizes ranging from 60–160 nanometers, while those treated with nitric acid exhibited particle sizes of 100–150 nanometers, as determined by scanning and transmission electron microscopy.

Additionally, the internal structure of the silicon dioxide particles indicated an oxidation state of Si^{4+}, confirmed through X-ray absorption spectroscopy in samples leached with both hydrochloric and nitric acid.

School of Physics
Academic Year 2023

Student's Signature ____________

Advisor's Signature ____________

ACKNOWLEDGEMENT

The thesis was successfully completed during the period from August 2019 to April 2024 at the Advanced Materials Physics Laboratory (AMPL), Department of Physics, Faculty of Science, Suranaree University of Technology. At the outset, I would like to express my gratitude to Prof. Dr. Santi Maensiri for providing the opportunity, financial support, and valuable suggestions for this work.

I would like to extend my thanks to a committee member for their insightful feedback and suggestions. I extend my appreciation to the Synchrotron Light Research Institute (BL 5.2) and the Office of the Higher Education Commission under the NRU Project of Thailand for granting permission and helpful suggestion for my XAS measurement.

I would like to express my gratitude to my fellow AMPL members for their helpful advice and for organizing weekly gatherings every Friday during my studies.

Finally, I am deeply grateful to my family for their ideas, care, love, and support that I have received from them.

Anuchit Sawangprom

CONTENTS

Page

CHAPTER

CONTENTS (Continued)

LIST OF TABLES

LIST OF FIGURES

LIST OF FIGURES (Continued)

LIST OF FIGURES (Continued)

LIST OF FIGURES (Continued)

LIST OF FIGURES (Continued)

Figure Page

LIST OF ABBREVIATIONS AND SYMBOLS

TG	Thermogravimetric
DSC	Differential scanning calorimetry (TG-DSC)
XRD	X-ray Powder Diffraction
EDXRF	Energy Dispersive X-ray Fluorescence
FT-IR	Fourier transform infrared spectra
FE-SEM	Field emission scanning electron microscope
EDS	Energy dispersive spectrum
TEM	Transmission electron microscopy
XAS	X-ray absorption spectroscopy
XANES	X-ray near edge structure (XANE)
EXAFTS	Extended X-ray absorption fine structure
SAED	Selected area (electron) diffraction
JCPDS	Joint Committee on Powder Diffraction Standards
LS-HCl	Treatment Actinoscirpus grossus with hydrochloric sample
DHCl	Treatment SiO_2 with hydrochloric sample
$DHNO_3$	Treatment SiO_2 with nitric acid sample
AG	Actinoscirpus grossus
BOD	Biochemical oxygen demand
COD	Chemical Oxygen Demand

LIST OF ABBREVIATIONS AND SYMBOLS (Continued)

HCl	Hydrochloric acid
HNO_3	Nitric acid
ΔH	Enthalpy of reaction
Cp	Specific heat capacity
s_0^2	Amplitude reduction term
N_j	Coordination number of neighbour atom
R_j	Distance to neighbouring atom
$f_j(k)$	Photoelectron scattering properties of neighbouring atom
$\mu(E)$	Energy absorption spectrum
σ_j^2	Mean-square disorder of neighbor atom

CHAPTER I

INTRODUCTION

1.1 Background and significance of the study

The most abundance of element in the earth crust can be classified into ten elements: Oxygen (46.60%), Silicon (27.72%), Aluminium (8.13%), Iron (5.00%), Calcium (3.63%), Sodium (2.83%), Magnesium (2.09%), Potassium (2.59%), Titanium (0.44%), Hydrogen (0.14%), and other element (0.83%) (Fleischer, 1953). The Si metal is the second most abundant element after the oxygen element (Kuhlmann, 1963). Generally, silicon on the earth's surface was a shape in the form of silica structure. Silica is a bonding between silicon and oxygen. The structure of Si-O bonding is mostly the form of the tetrahedral with the symbol SiO_2. Structure of SiO_2 has a widespread benefit in human industrials, which can be classified into six types by industrial demand such as the electronic, automotive, energy, pharmaceutical, food, and cosmetic.

In the electronic industry, electronics contain SiO_2 is the most commonly used in manufacturing transistors, computer chips, and integrated circuits. The SiO_2 structure for electronic is in the form of fused silica (quartz). Fused silica is a good dielectric and insulating property used for refractory material in electronic devices (Lines, 2001). For automotive industry, SiO_2 is mostly used for improvement of scratch resistant, surface hardness, and durability of automotive part after silica coating (TOGWT, 2014). Moreover, the enhanced energy efficiency of SiO_2 leads to many products in industrials demand such as solar cells and thermoelectric devices. The good semiconductor and mesoporous properties of SiO_2 help for improving energy performance. The properties of SiO_2 help to decrease a thermal conductivity in thermoelectric devices (Budak, Parker et al., 2013) (Wu, Wei et al., 2017) and light trapping in solar cell device (Chandrasekhar, Dubey et al., 2018) (Mohan, Shimomura et al., 2012). However, the properties of SiO_2 are good as a glidant and an anti-caking for use in pharmaceutical products and food products. For the cosmetic industry, SiO_2 is used as ingredients of toothpaste, body washes, facial cream, and cosmetic cream (Rashid, Daraghmeh et al., 2011). Hence, SiO_2 is found in many products of our daily life.

However, industrial silica products can be classified into two categories by the source: silica in geology (Geo-silica) and silica in biology (Bio-silica). Geo-silica is SiO_2 in rock, soils, and sand, which is mostly used in industrials for synthesis of high-purity silica. The structure of SiO_2 in Geo-silica is in the form of crystalline. The most nature crystalline of SiO_2 is the quartz and cristobalite structure (Zurowski, Zepchło et al., 2021).

Similarly, Bio-silica is one of the sources for silica synthesis of industrial silica products. The silica in Bio-silica is found in all monocots and all dicots, such as husk rice, sugar cane, wheat straw, corn cab ash, coconut husk, and bamboo leaves (Irzaman, Oktaviani et al., 2018). In addition, the types and amount of silica in Bio are controlled by types of plants. Generally, the type and the amount of silica or silica body are related to the phytolith shape on the surface of the leaf and stem. In 2018, Bakhat et al. reported that silicon accumulates in plants. The high silicon content accumulates in grass families such as rice husk, horsetail, sugarcane, and wheat (Bakhat, Bibi et al., 2018).

At the present, the SiO_2 synthesis from Bio-silica is favouring industrial silica because SiO_2 has a simpler synthesis than SiO_2 preparaedfrom Geo-silica. Moreover, the trend of the global rice husk ash market is expected to be 4.7% for market growth from 2021 to 2028 owing to the increasing industrial demand of rice husk in many countries as shown in Figure 1.1.

Figure 1.1 Global rice husk ash market – industry trends and forecast to 2028 (market, 2021).

From Figure 1.1, the trend of rice husk ash is illustrative the trend of SiO_2-increased industrial demand in many countries. Hence, the study of the SiO_2 synthesized from Bio-silica by using an Actinoscirpus grossus (AG) is of research interest. The AG is a monocots plant in the family Cyperaceae. The Cyperaceae are a graminoid family (grass-like). This plant is found across East and South Asia (Simpson, Muasya et al., 2007). Interestingly, the ability of this plant is rapid growth, high metal absorbance, and the shapes of the leaves are grass-like and rice but the size AG bigger than grass and rice. In 2016, lemon grass was studied in the synthesis of silica by the acid leaching. The lemon grasses can be extracted the silica from leaves, which is obtained highly pure SiO_2 (>98%) (Firdaus, Osman et al., 2016). Similarly, rice is one of the plants in the Poaceae family as the same lemon grasses. Mostly, part of rice for SiO_2 synthesis is the husk.

Generally, rice husk is used acid leaching for the synthesis of SiO_2because this method is easier and lower cost than other methods. The chemical synthesis of SiO_2 is mostly a strong acid and functions for the removal of soil. Normally, one most common strong acid for synthesis is hydrochloric acid (HCL) due to HCL acid being able to remove alkaline metal from material (Nayak, Nandi, and Datta, 2019). Various alkaline metals in plants are in the form of alkaline metal oxide such as CaO, K_2O, P_2O_5, Fe_2O_3, MnO_2, etc. In the several reports, the obtained structure of the silica after using HCL for Bio-silica leach was found to be high purity. For example, SK S. Hossain et al. reported that Rice husk (RH) was treated by 1M of HCL at 90°C for 2h after washing with DI water. They found a highly pure of SiO_2 (>95%) (Hossain, Mathur et al., 2018). In 2021, Luyza Bortolotto Teixeira et al. reported that highly pure SiO_2 (~95.3%) was obtained from HCL(1M) leach of sugarcane bagasse and leaf ash in the preparation (Bortolotto Teixeira, Guzi de Moraes et al., 2021).

Similarly, SiO_2 from wheat straw, corn cab ash, coconut husk, grasses, and bamboo leaves found a high purity of SiO_2 (>90%) after treated with HCL. Moreover, HNO_3 and HSO_4 are the choice of acids for the synthesis of high-purity SiO_2 as the same as HCL, which has a mass fraction of silica >90% after rice husk treats with HNO_3 and HSO_4 (Matori, Haslinawati et al., 2009). Hence, this work focus on the silica extracted from Actinoscirpus grossus leaves. The silica nanoparticles are synthesized by a simple synthesis using different strong acids of HCL, and HNO_3 as chemical leaching.

The structure of silica nanoparticles will be characterized by X-rays diffraction (XRD), energy-dispersive x-ray fluorescence (ED-XRF), energy dispersive spectrum (EDS), and fourier transform infrared spectra (FT-IR). Similarly, the morphology of silica nanoparticles will be studied by mapping and field emission scanning electron microscope (FE-SEM). The thermal effect of silica nanoparticles will be explained by thermogravimetric/differential scanning calorimetry (TG-DSC). The detailed morphology of the synthesized silica nanoparticles will be explored by high-resolution transmission electron microscopy (HR-TEM). Finally, the defect of SiO_2 structure will be considered by a X-ray near edge structure (XANE) and Extended X-ray absorption fine structure (EXAFS) analysis.

1.2 Objectives of this work

In this study, focus is given to the characterization of SiO_2 from Actinoscirpus grossus. This material has been investigated in terms of the synthesis-property-structure approach. Primary goals of this work are 98-99% of SiO_2 purity from Actinoscirpus grossus via simple synthesis method. Furthermore, there are sub-objective of this work, which are classified into seven parts:

1.2.1 To synthesize the SiO_2 from Actinoscirpus Grossus (AG) by acid-leaching method

1.2.2 To study the effects of the hydrochloric acid (HCl), and nitric acid (HNO_3) concentrations on the formation of SiO_2

1.2.3 To characterize the SiO_2 nanoparticles derived from the prepared SiO_2 ash

1.2.4 To produce high-purity SiO_2 from SiO_2 ash using an acid etching method

1.2.5 To characterize the synthesized high-purity SiO_2 nanoparticles

1.2.6 To study and describe the behavior of mechanism of high-purity SiO_2 growth

1.3 Scope and limitations

The first part of the scope and limitations focuses on the extraction of SiO_2 nanoparticles from Actinoscirpus grossus via a one-time acid etching method. The preparation process involves using hydrochloric acid as a chemical catalyst in the synthesis of SiO_2, with the boiling temperature fixed at 90°C for 3 hours. The second part of the scope and limitations focuses on the synthesis of high-purity SiO_2 from Actinoscirpus grossus ash or SiO_2 ash via a one-time acid etching method. The synthesis process utilizes two acids, hydrochloric and nitric acid, with concentrations ranging from 0.1 to 5 molarity.

1.4 Output and outcome of this work

1.4.1 Output

In the thesis, we will learn about Actinoscirpus grossus's synthesis method for SiO_2 nanoparticles and the SiO_2 products will acquire be high-purity SiO_2 that is just as pure as SiO_2 from the industry.

1.4.2 Outcome

The benefit of this study will be new alternative way of alternative source for SiO_2 products.

1.5 Thesis outline

The thesis comprises six chapters, as follows: Chapter I provides background information and discusses the significance of the research. Chapter II presents a review of relevant literature related to the thesis topic. Chapter III outlines the methodology, including procedures, measurement instruments, and characterization techniques used for SiO_2 ash and high-purity SiO_2 synthesis. Chapter IV presents the characterization results of SiO_2 ash, covering aspects such as phase composition, SiO_2 mass, nanostructure, and type. Chapter V discusses the characterization results of high-purity SiO_2, including SiO_2 mass, nanostructure, growth, and type. Finally, Chapter VI discusses the summarize of this work and recommendations for further work.

CHAPTER II

LITERATURE REVIEWS

In this chapter, we focus on the properties, sources, synthesis methods, and characterization of SiO_2 structures. First, we describe the properties of Si and SiO_2 structures and the types of SiO_2 found in nature. Second, we provide an overview of SiO_2 sources, including SiO_2 in plants and Actinoscirpus grossus. Third, we explain the preparation and trends in high-purity SiO_2. Finally, we discuss the theoretical background for the characterization of SiO_2 after synthesis.

2.1 The properties of SiO_2

Silicon (Si) is an element in period 3 with atomic number 14 in the periodic table and is the second most abundant element after oxygen (O). Si metal is a crystalline solid with a blue-grey metallic luster (Figure 2.1a). Silicon metal is characterized by its hardness, brittleness, high melting point of 1414°C, and high boiling point of 3265°C, as shown in Table 2.1. When Si interacts with O, the resulting compound is silicon dioxide (SiO_2), commonly referred to as silica, an inorganic chemical compound. Silica appears as a white nano-powder, as illustrated in Figure 2.1b. In nature, more than 90% of the Earth's surface is composed of silicon in the form of silica minerals. The discovery of silica dates back to 1787 by Antoine Lavoisier, who was unable to reduce the oxide and isolate the element due to the high chemical affinity between Si and O (Har, Irzaman et al., 2019).

a) b)

Figure 2.1 The characteristic of a) silicon (Wylezich 2022) and b) silicon dioxide powder (Corporation, 2022).

Table 2.1 Basic parameters of Silicon (Tilli and Haapalinna, 2020).

Properties of Si	Parameters of Silicon	
Atomic number of Si	14	
Atomic mass of Si	28 (92.23%)	29 (4.67%), 30 (3.1%)
Crystal structure	Diamond	
Lattice constant	0.5431	nm
Si atoms	5×10^{22}	atoms$\cdot$cm^{-3}
Melting point	1687	K
Specific density	2.329	g$\cdot$cm^{-3} at 298 K
Specific density (liquid)	2.57	g$\cdot$cm^{-3}
Thermal conductivity	149	W$\cdot$m^{-1} K^{-1}
Coefficient of thermal expansion	2.56×10^{-6}	m^{-1} K^{-1} (at 298 K)
Specific heat capacity	19.79	J$\cdot$mol^{-1} K^{-1}
	0.705	J$\cdot$g^{-1} K^{-1}

Table 2.1 Basic parameters of Silicon (Tilli and Haapalinna, 2020) (Continued).

Young's modulus	150	GPa
Speed of sound	8433	$m \cdot s^{-1}$
Hardness	7	Mohs
Hardness	850	$kg \cdot mm^{-2}$ (Knoop hardness)
Volumetric compression coefficient	1.02×10^{-8}	kPa^{-1}
Index of refraction (varies with temperature and λ)	~3.54 ~3.48	λ 1.1 μm, RT λ 2 μm, RT

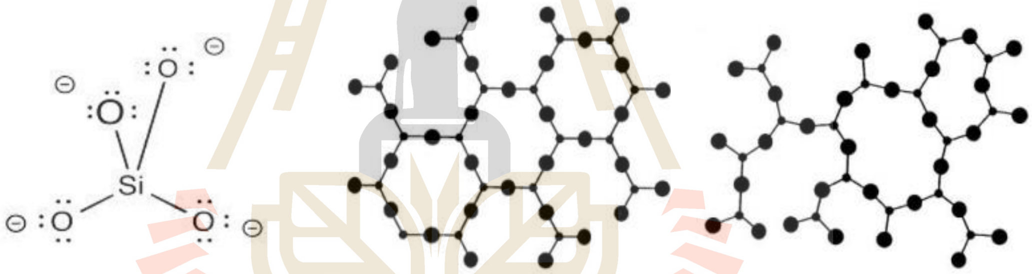

a) b) c)

Figure 2.2 Structure of silica: a) molecular structure of silica, b) crystalline structure of silica, and c) non-crystalline structure of silica (Pratt, 2015).

In 1808, Sir Humphry Davy successfully synthesized silicon from flint and Latin silex (Davy, 1808). Three years later, Gay-Lussac and Thénard were succeeded to prepare pure-amorphous silicon (Gay-Lussac and baron Thénard, 1811). Thereby, the silicon structure can be divided into a crystalline and non-crystalline

.

2.2 Silica in soils

In the soil, the silica structure can be classified into two types by mechanism in structure such as crystalline and non-crystalline (Zhou, Ma et al., 2022) (Figure 2.3).

2.2.1 Crystalline silica

Crystalline silica possesses a symmetrical silica structure characterized by a specific crystalline model. This particular model of silica structure can be categorized into three types based on its form: quartz, cristobalite, and tridymite (see Figure 2.3). Quartz, a robust silica mineral, exhibits a continuous framework of tetrahedral-shaped atoms, with oxygen atoms shared between two hexagonal units. Quartz is widely distributed in the Earth's crust, including sedimentary and igneous rocks, as well as pockets of soil.

Cristobalite represents another silica structure, featuring atoms arranged in a continuous tetragonal framework formed at very high temperatures. Cristobalite is typically found in acidic volcanic rocks. Tridymite, the third silica structure, assumes a unique half-solid and half-liquid form. Its continuous framework is rhombohedral, and tridymite is commonly present in volcanic rocks (Secretariat, 2018). Quartz, cristobalite, and tridymite collectively fall under the term 'silica polymorphs,' and they exhibit distinct properties, as illustrated in Table 2.2.

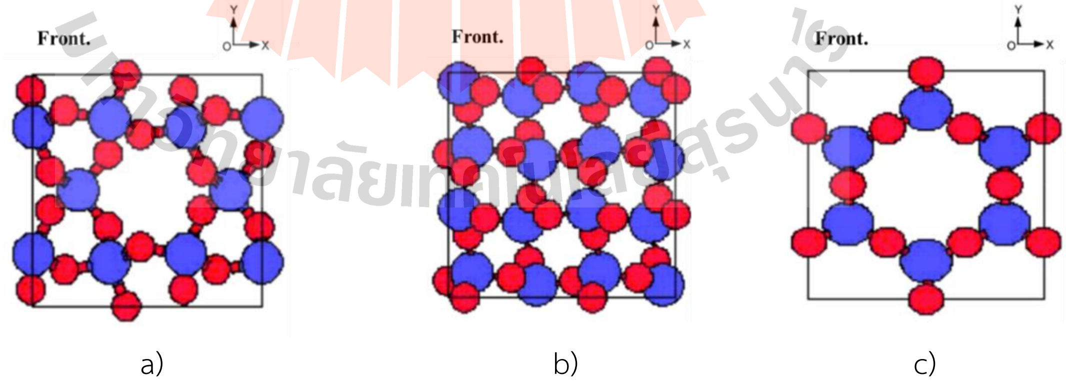

a) b) c)

Figure 2.3 The models of SiO_2: a) α-quartz, b) cristobalite, and c) tridymite. (Key-Schwartz, Baron, Bartley, Rice, and Schlecht, 2003).

Moreover, polymorph transformation or polymorphism is the ability of silica crystalline to exist in more than one form. The polymorph transformation can occur after increasing thermal in silica. The study of polymorph transformation was proposed in 1961 by A. C. D. Chaklader and A. L. Roberts. They found that heat affected the polymorph transformation. The polymorph transformation occurred from the thermal increase of quartz in the range of 1400°C to 1650°C. After that, the density of an intermediate phase transition from quartz to cristobalite was found to be 2.30±0.005 gm. per cc (Chaklader and Roberts, 1961). Moreover, the chemical composition is one of the parameters in thermal transformation for crystal-changed. In 1961, Holmquist reported that the quartz mixed with Na_2O, K_2O, and Li_2O was affected the thermal transformation for crystal-changed. Quartz/Na_2O, Quartz/ K_2O, and Quartz/ Li_2O could be converted to tridymite with temperatures of about 872 883, and 1005°C (Holmquist, 1961), respectively. Similarly, Jusnes et al. also reported the transformation of quartz to cristobalite. They found that the transition of quartz to cristobalite depended on quartz types. In their experiment, quartz from different localities was used. The transition of quartz to cristobalite is a different heat-utilized (Jusnes, Tangstad et al., 2018).

Table 2.2 The physics properties of silica polymorph (Key-Schwartz, Baron et al., 2003).

Silica Polymorph	Crystal Structure	Index of refraction	Specific gravity	Other properties
Quartz	Hexagonal	1.544	2.645-2.660	Mol.Wt. 60.08 m.p.°C 1610
Cristobalite	Tetragonal	1.487	2.32	Mol.Wt. 60.08 m.p.°C 1723
Tridymite	Rhombohedral	1.469	2.26	Mol.Wt. 60.08 m.p.°C 1703

2.2.2 Non crystalline silica

Non-crystalline silica exhibits an asymmetrical structure compared to crystalline silica. This asymmetrical structure is commonly referred to as amorphous silica. Amorphous silica manifests various structures in nature, including fused quartz, fumed silica, silica gel, and aerogels (int, 2019). Amorphous silica can occur naturally or be synthesized, and it is commonly found in general soils, unicellular organisms, and diatoms, including specific parts of plants.

In soil, silica typically exists in two states: solid and solution. In its solid state, amorphous silica takes the form of a white powder, as depicted in Figure 2.1b. This white silica powder is a porous material with varying pore density depending on the soil type. Additionally, amorphous silica solution is generated by introducing water to thermally treated silica, usually at temperatures around 800°C, to replace Si–O–Si linkages with Si–OH groups. These Si–OH groups, or $Si(OH)_4$, are commonly referred to as silicic acid (Pauling, 1960) (Figure 2.4). Silicic acid is predominantly sourced from oceans and soils in nature. More than 70% of Earth's surface is covered by oceans, making the production of silicic acid through the reaction of silica and water quite accessible. Silicic acid is also present in Earth's crust within soils like clay, sand, and mold.

Numerous articles have reported the benefits of silicic acid, as it serves as one of the acids that benefit plant growth by enhancing plant strength and reducing ATP consumption in membrane cells. However, after plant uptake, silicic acid can transform into polysilicate compounds. Interestingly, natural plants can further convert polysilicates into siloxanes (Si-O-Si), silanes (Si-H), and organic silicon compounds (Si-C-R) or (Si-O-R)."

Formula of weak acid	Chemical structure image
$SiO_2+2H_2O \rightarrow Si(OH)_4$	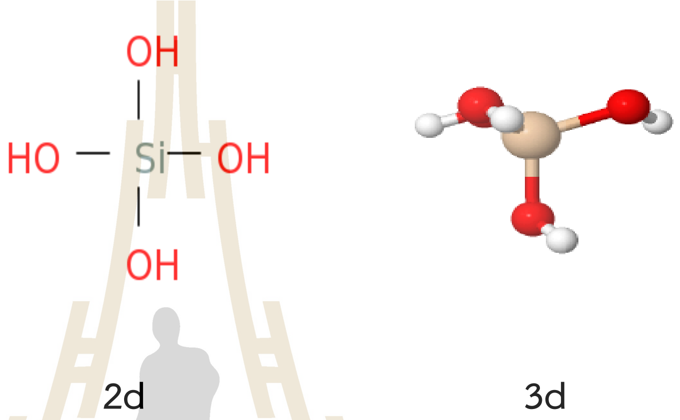

Figure 2.4 The formula acid and chemical structure of silicic acid (in 2D and 3D) (ChemEssen, 2019).

2.3 Silicon in plants

Elements present in the soil serve as nutrients for plants, and they come in various types, including potassium (K), nitrogen (N), phosphorous (P), and silicon (Si). These elements play distinct roles in supporting plant growth. For instance, potassium (K) is an indispensable nutrient for plants and serves four key functions. First, it plays a crucial role in the generation of Adenosine Triphosphate (ATP). Second, it facilitates osmoregulation in plant tissues and cells. Third, it is a vital component in the synthesis of proteins and starch. Lastly, it helps regulate the opening and closing of stomata, thereby enhancing photosynthesis (Tajer, 2016). Nitrogen (N), on the other hand, offers several benefits, including (i) aiding in the production of chlorophyll, (ii) promoting the growth of essential plant tissues, (iii) strengthening plant DNA, and (iv) assisting in the photolysis process (Miller, 2021). Phosphorus (P) accelerates maturation, stimulates tillering, and enhances plant resilience (Wise, 2012). Additionally, silicon dioxide is another vital nutrient that contributes to increased strength in plant stems, shoots, and leaves.

2.3.1 Silicon uptake and accumulate in plants

Typically, plants are unable to directly absorb elements present in the soil, such as silicon dioxide (Mitani, Ma et al., 2005). Consequently, the process of silicon uptake commences with solid silica transforming into soluble silica. The soluble form of silica is known as silicic acid, with concentrations typically ranging from 0.1 to 0.6 mM (Tubaña and Heckman, 2015, Imtiaz, Rizwan et al., 2016) and the pH of the acid is maintained at less than 9 (Khan, Khan et al. 2019). Once absorbed by plants, silicon is distributed throughout various plant parts, including the roots, stems, leaves, and shoots. Generally, plants accumulate silicon in the range of 1 to 100 g/Kg, with the amount depending on their capacity to translocate and accumulate Si (Souri, Khanna et al., 2021). The efficiency of silicon translocation and accumulation largely depends on the plant species.

Silica uptake can be roughly divided into three key steps. In the initial stage, plants absorb monosilicic acid and convert it into disilicic acid (dimer anion) through the roots. Subsequently, the silicic acid is transported via the root xylem to all parts of the plant (Ma and Yamaji, 2008) in the second step. Within the leaf xylem, silicic acid takes on a polymeric form. In the final step, the polymeric silicic acid (nH_4SiO_4) in the leaf xylem undergoes transformation into silica gel ($nSiO_2 \cdot nH_2O$) (Imtiaz et al., 2016) and accumulates within phytoliths, as illustrated in Figure 2.5 of the silicic acid to amorphous silica transformation. These phytoliths are commonly referred to as silica bodies, with their specific shapes varying based on the plant family. Similarly, the quantity of silica present is linked to the plant's botanical family.

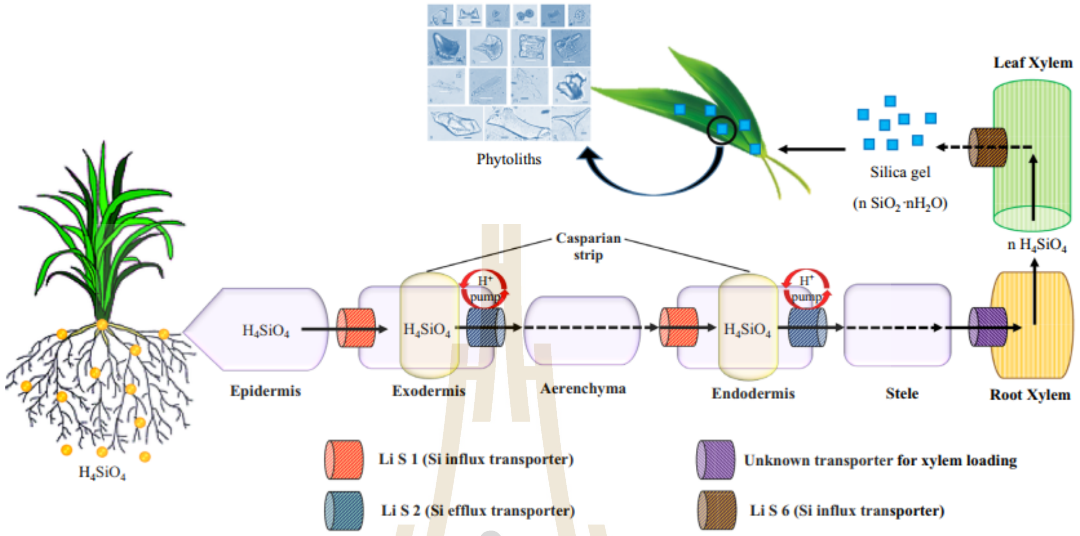

Figure 2.5 Schematic representation of the silicon uptake system in rice (Souri et al., 2021).

In 2015, Harley et al. explained the silica deposition and the silica shape on the different surfaces of the grass leaves. They reported that silica was found within the harsh (i.e., feeling rough to the touch) texture greater than the soft one of the leaf surfaces. In the harsh and soft texture, the silica was accumulated within leaf spines (red circle in Figure 2.6a and Figure 2.6b) and the shape of silica was a short cell.

SEM EDX SEM EDX

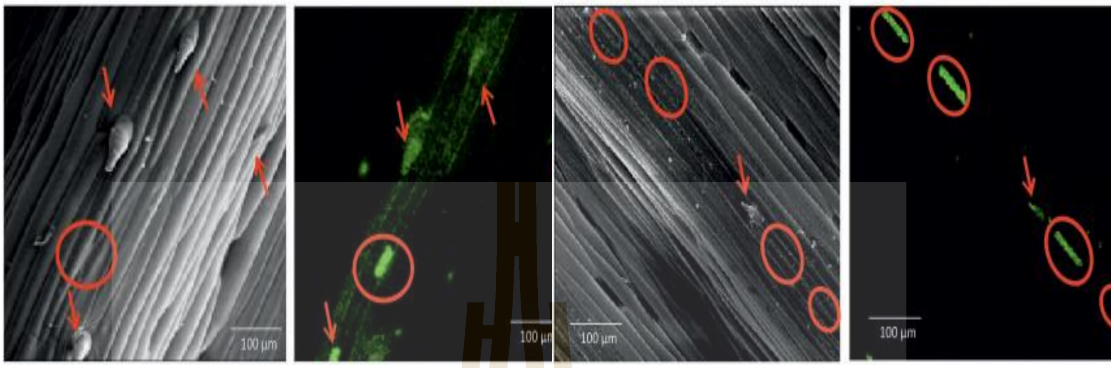

(a) (b)

Figure 2.6 (a) Harsh variety abaxail surface (x200 magnification), (b) Soft variety abaxail surface (x200 magnification). SEM represents by grey images. EDX represents by black and green images; green intensity indicates Si concentration. Red circles indicate trichomes with Si deposition. Red arrows indicate silica short cells (Hartley, Fitt et al., 2015).

Moreover, grass family can be found phytoliths in cell wall, the stem, leaf sheath, stoma (Currie and Perry, 2007, Ju, Wang et al., 2017), and leaf blade surface (macro hair, long cells, shot cells, and micro hair) (Kumar, Soukup et al., 2017). Moreover, the different phytoliths depended on a grass family. The phytolith shapes of grass family are revealed in Table 2.3. The amount of silicon in plants depends on the type of plants and silicon within the soil, which is described above. In Table 2.4, Bakhat et al. (2018) and Khan et al. (2019) reported that the Si uptake capacity in phytoliths was classified into three categories: (i) high silicon accumulator (>1.5%), (ii) intermediate silicon accumulator (1.5%-0.5%), and (iii) non-accumulator (<0.5%). Interestingly, they explained that grass family (rice, horsetail, sugarcane, and wheat) was a group of high silicon accumulator. Later, many articles used a grass family for the synthesis of silica such as rice husk, rice straw, sugarcane, bamboo leaf, and wheat. Thereby, the synthesis of silica which is extracted from Actinoscirpus grossus (AG), one of the grass species, is of interest in this study.

Table 2.3 Phytolith shapes on grass species (Lu and Liu, 2003, Piperno and Sues, 2005).

GPWG Poaceae phylogeny	Phytolith shapes	Morphotypes
Anomochlooideae	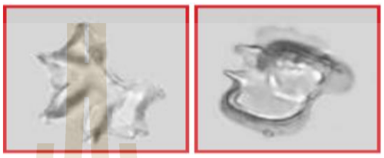	Crescentic
Pharoideae		Rondel/saddle ellipsoid
Bambusoideae		Long saddle and cross
Ehrhartoideae		Short saddle
Pooideae	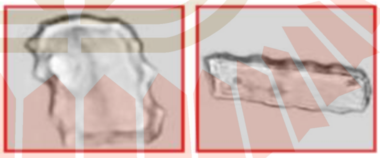	Wavy trapezoid
Aristidoideae		Dumbbell
Chloridoideae		Plateau saddle
Panicoideae	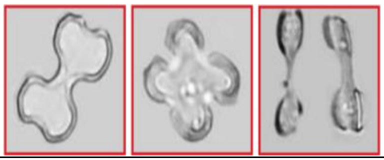	Dumbbell and cross

Table 2.4 Plant categories based on Si uptake capacity (Bakhat et al., 2018; Khan et al., 2019).

(>1.5%) Si high accumulator	(1.5%-0.5%) Si intermediate accumulator	(<0.5%) Si non-accumulator
Rice	Pumpkins	Tomato
Ferns	Cucumber	Pansy
Lentils	Rose	Begonia
Horsetail	Squash	Grapes
Mosses	Chrysanthemums	Sunflower
Sugarcane	Soybean	Gerbera
Conifers	Zinnia	Petunia
Wheat	New Guinea Impatiens	Snapdragon
Spinach	Marigold	Geranium

2.4 Actinoscirpus grosus

Actinoscirpus grossus (AG) is contained in the Cyperaceae family, which is a family of graminoids (grass-like). AG is a monocots plant. The essential characteristics of AG are culm triangle and taller about 1-2 meters after fully grown. The body shape of the leaf is a long, narrow shape, the same as a leaf's blade shape of grass but a size bigger than grass, as shown in Figure 2.7a-2.7b. The long of leaf is about 50-100 centimetres. The growing place of AG can be grown in the wetland. AG has rapid growth from seed germination to mature plants of about 3-4 months and dried plants after a mature plant of about 1-3 months. In Figure 2.7c, AG can be found across East and South Asia such as in China, Malaysia, India, Australia, Japan, Myanmar, Laos, Cambodia, and Thailand (Goetghebeur and Simpson, 1991).

In Thailand, AG can be found in all regions but mostly appeared in the central region, north, and northeast. Interestingly, the AG is used in many products such as folk medicine (a treatment for liver disease) (Ganapathi, Holla et al., 2021), animal feed, and household goods. Moreover, reducing the toxicity in water by AG or grossus family is one of the AG properties for wastewater treatment. For two decades, most articles have studied AG growth and the efficiency of wastewater treatment by AG as shown in Table 2.5.

(a) (b)

(c)

Figure 2.7 Actinoscirpus grossus (AG): (a) part of AG (Kostermans, Wirjahardja et al., 1987), (b) dried AG (D.A.Simpson, 2017) and (c) AG-location (Holm, Pancho et al., 1979).

Many articles are shown the Chemical Oxygen Demand (COD) and Biochemical Oxygen Demand (BOD) of water for study about wastewater treatment. COD is chemical oxygen demand. COD data represent a strong oxidizing agent of chemical under acidic conditions. The strong oxidizing agent of chemical can oxidize almost every organic to carbon dioxide (Merck, 2021). Hence, the measurement of COD commonly represents the degree of organic pollution in water bodies (Li, Luo et al., 2018). Moreover, the mass of oxygen per liter of solution (mg/L) is the measurement unit of COD. BOD is biochemical oxygen demand. BOD data represent amount of oxygen after organic decomposed by bacteria in water. Oxygen mass per liter is a measurement unit of the BOD as same as the COD unit. The total petroleum hydrocarbon is commonly referred to as total Petroleum Hydrocarbon (TPH). TPH represents the amount of hydrocarbon from diesel- contaminated or petroleum-contaminated in water or solution. Normally, TPH is measured the quality of wastewater after petroleum-contaminated. However, the standard of COD, BOD, and TPH depends on the requirements for each country.

Moreover, the AG propagation is one of the favored-research of about 2013-2020. In 2013, A. MAJRASHI et al. described the root system in the rhizomatous plant, Scirpus grossus L. In the experiment, they compared the root changes of AG by using peat and paddy soils. They have also demonstrated that the roots are not significantly different be compared to roots changes in peat and paddy soil. From the results of the experiment, the cause of these results may be due to a slight difference in soils structures (Majrashi, Bakar et al., 2013).

Table 2.5 AG trends research in 2003-2020.

Waste absorbed	Removal eff % of element in water	References
Agricultural wastewater	BOD: 96-99% COD: 91-95%	(Kantawanichkul, Somprasert, Aekasin, and Shutes, 2003) (Kantawanichkul, Somprasert et al., 2003)
Nitrate and ammonium	BOD: 68%	(KBSN Jinadasa, N Tanaka, MIM Mowjood, and DRIB Werellagama, 2006) (Jinadasa, Tanaka et al., 2006)
Wastewater from a student hostel at the University of Peradeniya, Sri Lanka.	BOD: 46.6-69.3%	(KBSN Jinadasa, Norio Tanaka, MIM Mowjood, and DRIB Werellagama, 2006) (Jinadasa, Tanaka et al., 2006)
Diesel-contaminated water	TPH: 91.5%	(Al-Baldawi, Abdullah, Anuar, and Idris, 2013) (Al-Baldawi, Abdullah et al., 2013)
Diesel-contaminated water	TPH: 93.72% in stem and leaf samples	(Al-Baldawi, Abdullah, Anuar, Suja, and Mushrifah, 2015) (Al-Baldawi, Abdullah et al., 2015)
Methylene blue in wastewater	BOD: 25-46% COD: 21-58%	(Almaamary, Abdullah, Hasan, Rahim, and Idris, 2017) (Almaamary, Abdullah et al., 2017)
Batik Wastewater in Indonesia	BOD: 97% COD: 89%	(Tangahu, Ningsih, Kurniawan, and Imron, 2019) (Tangahu, Ningsih et al., 2019)
Sago mill effluent (SME) wastewater	BOD: 93% COD: 88%	(Nash et al., 2020) (Nash, Abdullah et al., 2020)

However, AG plants can grow in wetlands as described above. In 2016, Tangahu has successfully studied the propagation of Scirpus grossus in wastewater (Figure 2.8a).

The experiment took 30 weeks for the study of the propagation. The results demonstrated that the wet and dry weight of plants increased from the first week to week-24 and started decreasing the week after as shown in Figure 2. Figure 2.8b. The decrease of the wet and dry weight of plants is due to the decreasing water concentration inside of plant tissue after week-24 as revealed in Figure 2.8c. Root length and plant height are shown in Figure 2.8d. From Figure 2.8d, they found the increase of root length on week-2 and the same the week after to the end. In addition, the plant height in this experiment was around 120-130 cm.

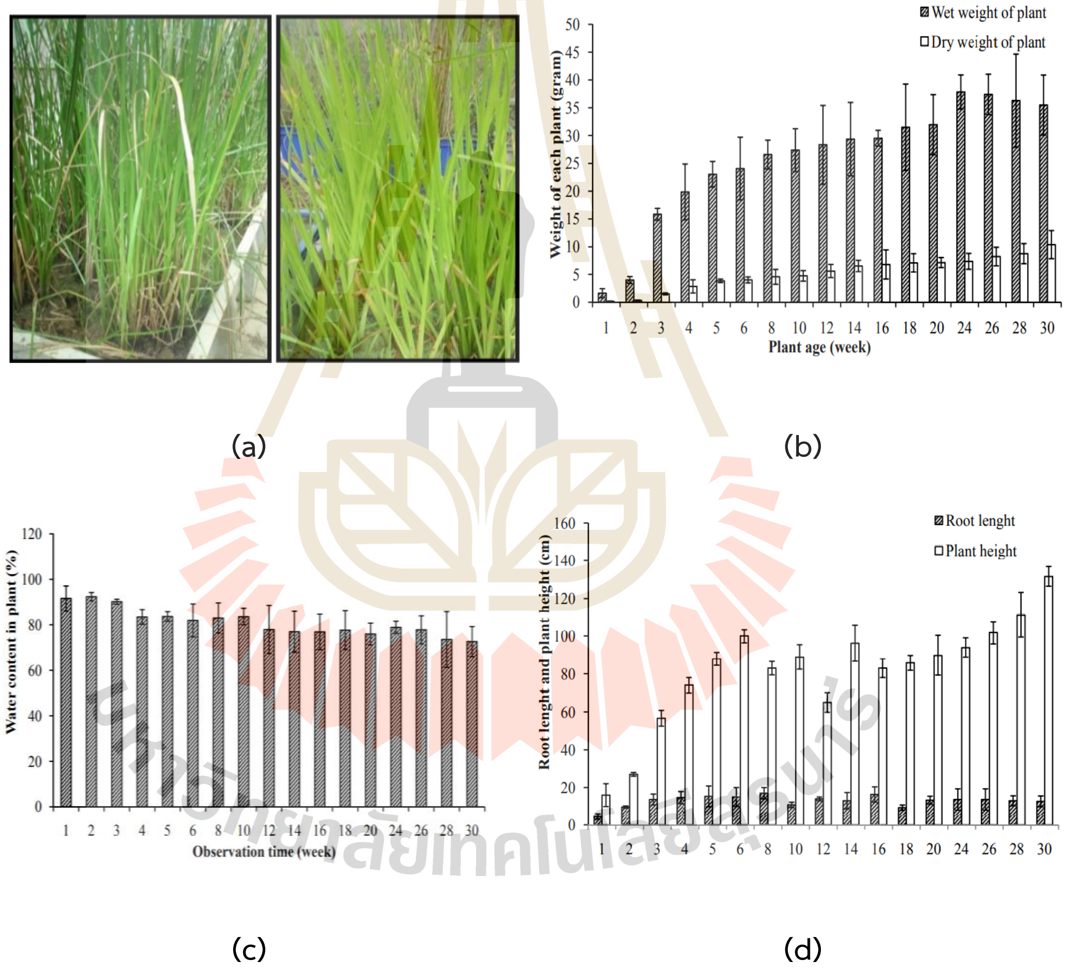

Figure 2.8 Growth data of Acitioscirpuss grossus : (a) scirpuss grossus, (b) wet weight and dry weight of plant during propagation, (c) water content in plant, and (d) root length and plant height during propagation time (Tangahu, 2016).

In 2020, Daniah Ali Hassoon Nash et al. reported that one of the benefit of AG was absorbed high levels of organic and inorganic pollutants and surviving in harsh conditions of water pollution. Moreover, they also found a physicochemical property of wastewater related to good AG growth, which was an average pH of about 4.8-7.2 in water (Nash et al., 2020) (Nash, Abdullah et al., 2020).

At the present, the study about wastewater treatment and the propagation of Scirpus grossus is still available. While the study about the synthesis of high purity of silica has been no reported. Hence, this thesis focuses on the study of SiO_2-extracted from the AG plants. The reasons are as follows: (i), the reporting high purity synthesis of silica from AG is not still available as described above, (ii) the raw material is low cost, and (iii) there are a lot of these plants in all regions of countries as described above.

2.5 The preparation and trend of high purity SiO_2

SiO_2 extraction involves synthesizing high-purity SiO_2 from impure SiO_2. Naturally occurring silica contains impurities such as Al, K, Na, B, Ca, Mg, and P (Khalifa, Hajji, and Ezzaouia, 2012). There are various techniques for producing silicon. In the 20th century, industrial silica was produced using the thermal reduction of silica with CO_2 (Mukashev et al., 2009; Popovich et al., 2008; Raman et al., 2002). However, this method often results in products with undesirable impurities and is very expensive.

To remove impurities and reduce the cost of silicon production, various techniques have been developed, such as reverse flotation (Mowla, Karimi, and Ostadnezhad, 2008) and power ultrasound (Farmer, Collings, and Jameson, 2000). Currently, acid leaching is a widely utilized method due to its low cost, simplicity, and effectiveness in removing impurities. Common acids used in this process include hydrochloric acid (HCl), nitric acid (HNO_3), and sulfuric acid (H_2SO_4). These acids are effective in removing alkaline metal oxides from the silica structure. As a result, high-purity SiO_2, ranging from 90-99%, has been reported in numerous studies using these acids, as summarized in Table 2.6. This thesis focuses on studying the effects of HCl, HNO_3, and H_2SO_4 on the synthesis of SiO_2 from Actinoscirpus grossus (AG).

Table 2.6 The trends of the biological synthesis of SiO_2 (2010-2020).

Materials	Acids-utilized for leaching	% Mass fraction	Production of silica	References
Lemon grass	LS-HCl 5M	67.06-98.59%	Powders	(Firdaus et al., 2016) (Firdaus, Osman et al., 2016)
Wheat hull	LS-HCl 0.1M	93.9%	powders	(Terzioğlu, Yucel, Rabagah, and Özçimen, 2013) (Terzioğlu, Yucel et al., 2013)
Sugarcane Bagasse	LS-HCl 1M	88.13%	Powders	(Norsuraya, Fazlena, and Norhasyimi, 2016) (Norsuraya, Fazlena et al., 2016)
Rice husk	3% HCl, 10% H_2SO_4, 3% NaOH (v/v)	95.14-99.66%	Powders	(Yalcin and Sevinc, 2001) (Yalcin and Sevinc, 2001)
	HCl, HNO_3, H_2SO_4 (1M)	97.2-97.6%	Powders	(Matori et al., 2009) (Matori, Haslinawati et al., 2009)
	HNO_3, NaOH, HCl (1M)	98.3%	Powders	(Salavati-Niasari and Javidi, 2012) (Salavati-Niasari and Javidi, 2012)
	1N MOH, 1N MCO_3(M=Na, and K), 1 N HCl	95.9-99.1%	Powders	(Nayak et al., 2019) (Nayak, Nandi et al., 2019)
	2 M HCl	98.2%–99.7%	Powders	(Azat, Sartova, Bekseitova, and Askaruly, 2019) (Azat, Sartova et al., 2019)
	3N HCl and 3N NaOH	99.714%	Powders	(abualnoun Ajeel, Sukkar, and Zedin, 2020) (abualnoun Ajeel, Sukkar et al., 2020)
Rice straw	3N HCl	85.41%	Powders	(Har, Irzaman, and Irmansyah, 2019)

Bamboo leaf	LS-HCl 0.1M	83.6-93.4%	Powders	(Manurung, Siregar, and Zuhri, 2019) (Manurung, Siregar et al., 2019)
	4N HCl	96%	Powders	(Phomketjan and Wongprayoon, 2020) (Phomketjan and Wongprayoon, 2020)
Bamboo Strips	1N HCl, 1N NaOH	96.9%	Powders	(Yu et al., 2018) (Yu, Du et al., 2018)

Where N is normality and M is molarity. (In these chemical solutions, normality and molarity are equivalent or N = M)

2.6 Effect of thermal treatment on SiO_2 nanoparticles (TG/DTA and DSC)

The variation in chemical composition is the cause of the diverse thermal properties exhibited by different materials. These multiple thermal properties can be characterized using techniques such as thermogravimetry differential thermal analysis (TG/DTA). The effects of thermal properties in TG/DTA can be observed in the spectrum of mass change of materials. Furthermore, the phenomena of mass change can be explained by the differential spectrum of mass change in the curve of the differential scanning calorimetry (DSC), which depends on the effects of reduction and oxidation of the material.

The DSC spectra display both exothermic and endothermic peaks. Exothermic peaks correspond to processes or reactions that release heat. During an exothermic reaction, temperature of the sample will decrease, and the heat released during this process is detected by the DSC instrument. Exothermic peaks on the DSC curve indicate reactions or transitions where energy is released to the surroundings. Conversely, endothermic peaks correspond to processes or reactions that absorb heat. During an endothermic reaction, the temperature of sample will increase. Endothermic peaks on the DSC curve indicate reactions or transitions where energy is absorbed from the surroundings. The DSC curve depicting exothermic and endothermic reactions is shown in Figure 2.9. However, the exothermic and endothermic peaks in the DSC curve help identify and characterize physical or chemical transitions in the samples. Exothermic peaks often indicate processes such as crystallization (exothermic reactions), while endothermic peaks suggest processes like melting (endothermic reactions). In this thesis, we utilize TG/DTA and DSC curves to identify and characterize mass changes and the decomposition of bonds in Actinoscirpus grossus samples.

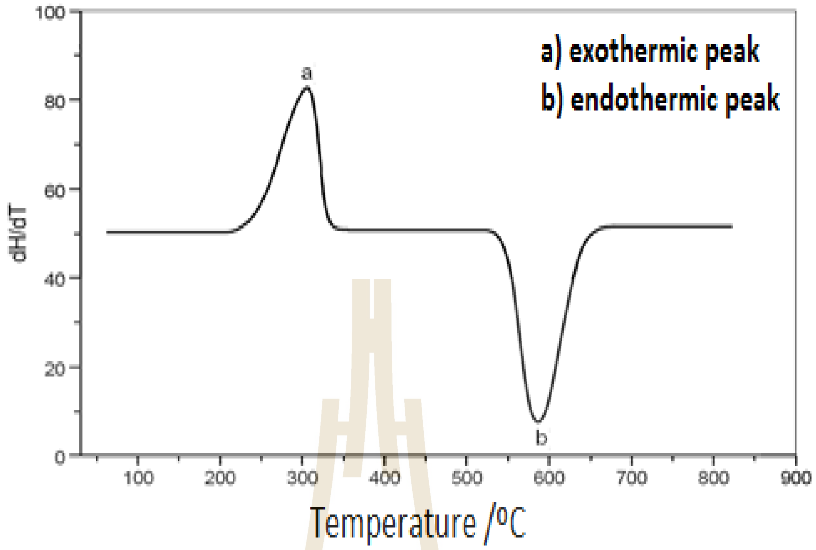

Figure 2.9 Simplified representation of the DTA for an exotherm and an endotherm (Hornung 2018).

The decomposition of chemical bonding will be reported in terms of the enthalpy (H) of energy loss, measured in milliwatts per gram (mW/g). The enthalpy ΔH of DSC spectra can be represented follows (2.1)

$$C_p=(\Delta H/\Delta T)_p \tag{2.1}$$

Where is Cp is specific heat capacity and ΔT is operating temperature scan.

In the differential scanning calorimetry techniques, Cp can be calculated by (2.2))

$$C_{p_s} = \frac{H}{h} \cdot \frac{m_r}{m_s} \cdot C_{p_r} \tag{2.2}$$

Where C_{ps} is C_p of sample, C_{pr} is C_p of reference, ms is weight of sample, mr is weight of reference, H is difference of heat flow of sample and empty pan, h is difference of heat flow of reference and empty pan. Furthermore, the DSC spectra for the enthalpy (H) description revealed in the relation between specific heat capacity and operating temperature scan. The diagram of DSC measurement and data spectrum depicted in Figure 2.10

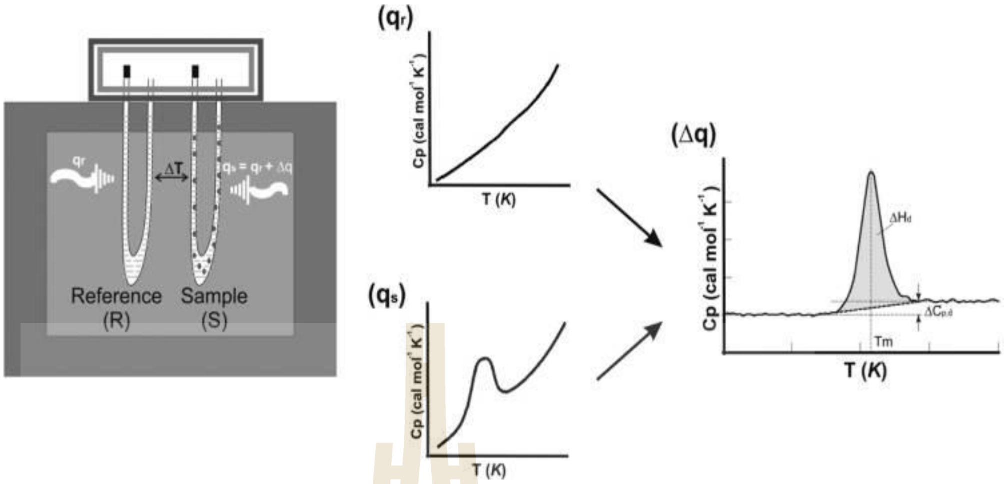

Figure 2.10 Measurement and data spectrum of DSC.

From the DSC spectra, we can be calculated the enthalpy (H) by using average area of peak in spectrum. This experiment, we use the enthalpy in description of dissociation of chemical bonding in Actinoscirpus grossus samples including C-C bond, N-N bond, or/and SiO_2 growth crystal.

2.7 The crystallographic structure and physical properties on SiO_2 nanoparticles

Typically, SiO_2 or glass exists in both amorphous and crystalline forms, which can be confirmed using high-precision measurement tools such as X-ray diffraction (XRD). XRD is a technique utilized for analyzing the crystal structure of materials. When X-rays interact with a crystalline sample, they undergo constructive and destructive interference, resulting in X-ray diffraction patterns as illustrated in Figure 2.11. By measuring the angles and intensities of X-rays, the atomic arrangement within the lattice can be determined. Different patterns in the XRD peaks indicate differences in the structure. The diffraction peaks in XRD patterns are determined by Bragg’s law, represented by Equation (2.3).

$$n \cdot \lambda = d \cdot \sin\theta \tag{2.3}$$

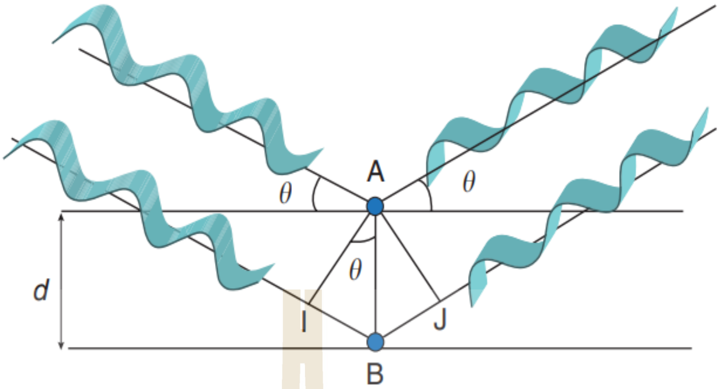

Figure 2.11 Bragg's law in the condition of reflection of X-rays. (Le Pevelen, 2010)

The peak in an XRD pattern can be referred to as the phase composition. The phase composition of amorphous materials refers to a disordered arrangement of atoms within the material, lacking the long-range order characteristic of crystalline structures. Unlike crystalline materials, which exhibit sharp diffraction peaks, amorphous materials produce broad, featureless patterns in XRD spectra. The phase composition of amorphous and crystalline structures of SiO_2 can be found in numerous studies, as depicted in Figure 2.12. From Figure 2.12, it can be observed that amorphous SiO_2 exhibits a broad shape without distinct diffraction peaks, indicating a high purity of the SiO_2 structure.

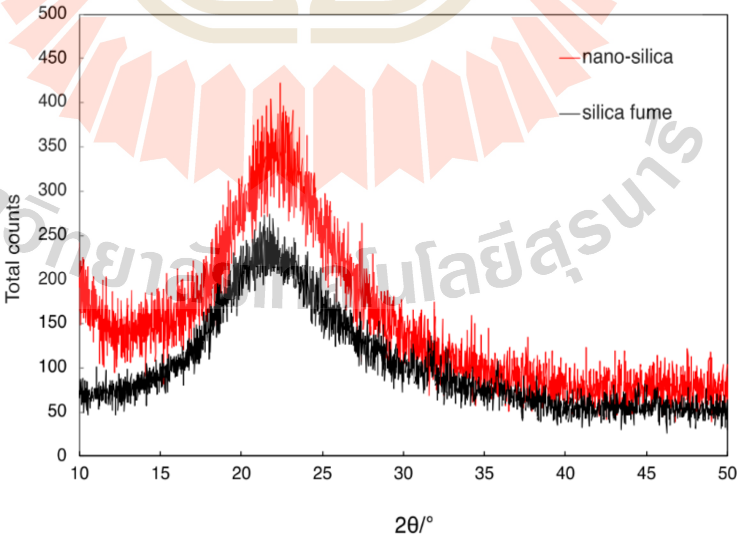

Figure 2.12 X-ray diffraction patterns of amorphous silica fume and nano-silica, showing broad diffuse scattering. (Maddalena, Hall et al., 2019)

2.8 The elemental composition of a material

The element composition of the material is determined by X-ray fluorescence (XRF). XRF operates on the principle that when a material is exposed to X-rays, it absorbs energy and re-emits it as fluorescent X-rays. The energy of these emitted X-rays corresponds to the elements present in the material, as illustrated in the diagram in Figure 2.13. The basic of XRF is break down of the process. When the sample is irradiated with high-energy X-rays, typically from an X-ray tube. This energy excites inner-shell electrons in the atoms of the sample. Some of the inner-shell electrons are ejected from their orbits, creating electron vacancies. Electrons from higher energy levels then fill these vacancies, releasing energy in the form of characteristic X-rays specific to each element. After this process, a detector measures the energy and intensity of the emitted X-rays and the X-ray spectrum is analyzed to identify the elements present and quantify their concentrations in the sample.

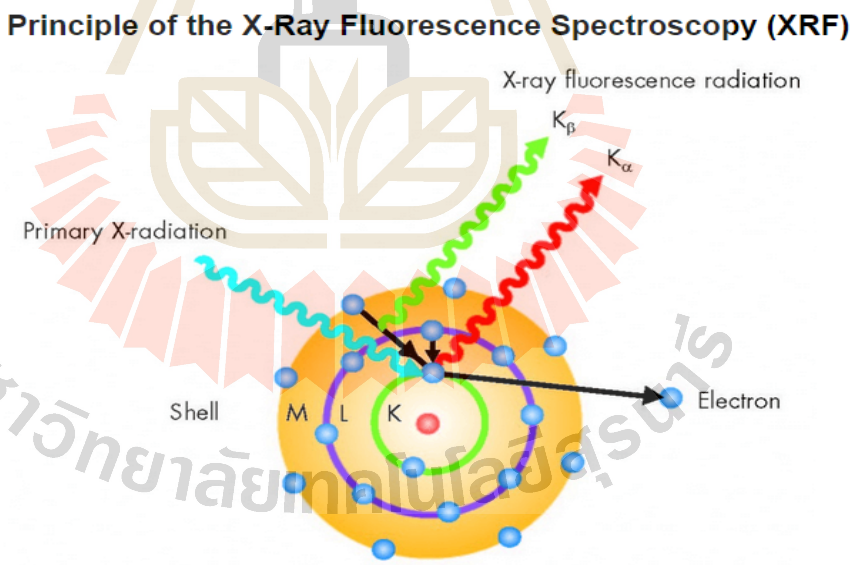

Figure 2.13 Basic principle of the X-Ray Fluorescence (XRF) spectroscopy (Fischer, 2015)

The concentration of the elements is expressed as a percentage of the mass fraction of the element and its oxide in the sample. Various articles utilize XRF to confirm the element concentrations in samples, including composite materials, or to investigate the extraction of pure elements. Example XRF data results can be found in Table 2., which presents the results of XRF measurements for SiO_2 extraction from rice husks in various research studies. In this study, we employed XRF to determine the elemental concentration in Actinoscirpus grossus samples after treatment with acid and calcination. We are focusing on the composition of the white powder of SiO_2 and the transformation of SiO_2 yields obtained from Actinoscirpus grossus. The transformation of SiO_2 yields is described by (2.4).

$$\text{Transformation of } SiO_2 \text{ yields} = \frac{SiO_{2\ \text{HCl etching}} - SiO_{2\ \text{un etching}}}{SiO_{2\ \text{un etching}}} \times 100\% \qquad (2.4)$$

Table 2.7 The elemental composition of a material analysis by XRF.

Composition of materials	SiO$_2$ extraction from rice husk				
	1st(Ghasemi, Younesi et al., 2011)	2nd(Azizi and Yousefpour, 2008)	3rd(Odunlami, Agboola et al., 2022)	4th(Lee, Othman et al., 2013)	5th(Radzali, Farah et al., 2013)
SiO$_2$	95.913	96.080	95.200	95.00	82.000
K$_2$O	0.103	0.510	1.500	1.500	8.100
Fe$_2$O$_3$	0.104	0.140	0.120	0.140	0.470
MnO	-	0.160	0.050	0.054	0.310
SO$_3$	0.044	-	0.100	0.099	0.500
MgO	0.240	0.480	0.450	0.420	2.500
P$_2$O$_5$	0.302	0.330	0.720	0.640	2.000
CaO	0.539	0.240	0.800	0.840	2.500
Al$_2$O$_3$	0.192	0.210	0.240	0.220	0.310

2.9 Infrared absorption spectrum of SiO_2 molecule

The analyzing chemical compositions of SiO_2 after synthesis is studied by Fourier transform infrared spectroscopy (FT-IR). FT-IR provides detailed information about molecular vibration and helping identify functional group in materials. FT-IR operate on the principle that molecules absorb infrared radiation at specific frequency, corresponding to the vibration mode of chemical composition. The FT-IR are the method that involve measurement of interference pattern create when the sample interact with infrared beam. The resulting interferogram is mathematically transform to the produce spectrum displaying absorb peak at characteristic frequencies. These peak shows the information about the molecular structure of organic and inorganic compound. Typically, FT-IR resulting spectrum involves two vibration modes: stretching, bending or torsional. Stretching is changes in the bond lengths, bending is changes in the angles, involves twisting around bond. The two modes of FT-IR reveal in Figure 2.14

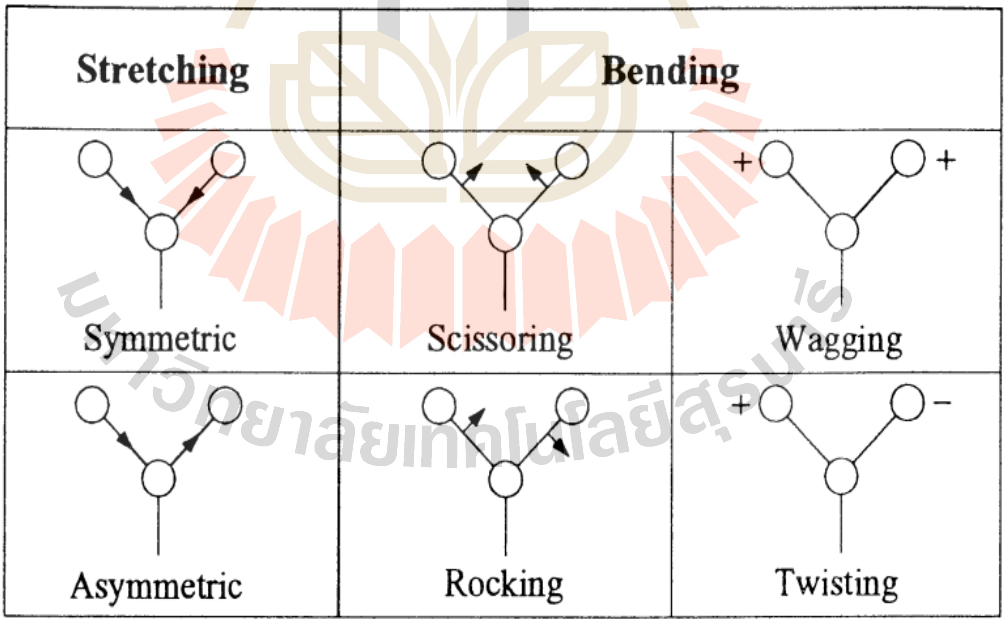

Figure 2.14 The stretching and bending vibrational modes represented in FT-IR spectra. In these modes, the "+" and "-" signs indicate that the atoms move

perpendicular to the plane of the page towards and away from the reader, respectively (Gustafsson 1996)

These modes occur at specific frequencies, providing specific spectral patterns for different molecule in material. The IR-frequency of analyzing measurement classified into two categories: organic (see in Table 2.8) and inorganic. This work, spectrum of inorganic reveals a spectral pattern for Si bond molecule, which is shown in Table 2.9.

Table 2.8 IR-frequency for organic group.

Type of compound	Wavenumber (cm^{-1})	Intensity	Bond
Alkanes	2850-2970	Strong	C-H
	1340-1470	Strong	
Alkanes	3010-3095	Medium	C-H
	675-995	Strong	
Alkynes	3300	Strong	C-H
Aromatic rings	3010-3100	Medium	C-H
	690-900	Strong	
Monomeric alcohols	3590-3650	Variable	O-H
Hydrogen-bonded alcohals	3200-3600		
Monomeric carboxylic acids	3500-3650	Medium	
Hydrogen-bonded carboxylic acids	2500-2700	Broad	
Amines	3300-3500	Medium	N-H
Alkenes	1610-1680	Variable	C=C
Aromatic rings	1500-1600	Variable	C=C

Table 2.8 IR-frequency for organic group (Continued).

Alkynes	2100-2260	Variable	$C\equiv C$
Amines	1180-1360	Strong	C-N
Nitriles	2210-2280	Strong	$C\equiv N$
Alcohols, eters, carboxylic acid	1050-1300	Strong	C-O
Aldehydes, ketone	1690-1760	Strong	C=O
Nitro compounds	1500-1570	Strong	NO_2
	1300-1370	Strong	

Table 2.9 IR-frequency for Si compound (Chen, Jia et al., 2015).

Functional group	Wavenuber(cm^{-1})	bond	Characteristic
$Si\text{-}CH{=}CH_2$	1613	C=C	Stretching vibration
	1410-1390	$CH{=}CH_2$	Scissoring vibration
	1020-1000	Trans C-H	Wagging vibration
	980-950	CH_2	Wagging vibration
$Si\text{-}(CH_3)_3$	1266	CH_3	Symmetrical deformation vibration
	1250	Double peaks CH_3	Rocking vibration
	840	Si-C	Stretching vibration

Table 2.9 IR-frequency for Si compound (Continued).

Si-$(CH_3)_3$	~1260	CH_3	Symmetrical deformation vibration
	855	Shape single peaks CH_3	Rocking vibration
	800		Strong absorption
Si-OH	3390-3200	OH	Stretching vibration
	910-830	Si-O	Stretching vibration
Si-O-Si (linear)	1080	Si-O	Stretching vibration
	1025	Si-O	Strong absorption
Si-O-Si (ring)	~1020	Si-O	Stretching vibration
	1090	Si-O	Strong absorption

2.10 Morphology of SiO_2 nanoparticles

High-resolution image of surface, offering detailed insights the topography and composition of specimens determined by Field Emission Scanning Electron Microscope (FE-SEM). The FE-SEM technique was employed in this study to investigate the morphology of SiO_2 nanoparticles. Pure SiO_2 typically exhibits various shapes, influenced by the structural types formed during the synthesis process. Numerous articles and biosources utilized in the synthesis of SiO_2 depict the pure form of SiO_2 as spherical and the irregular, as illustrated in Figure 2.15.

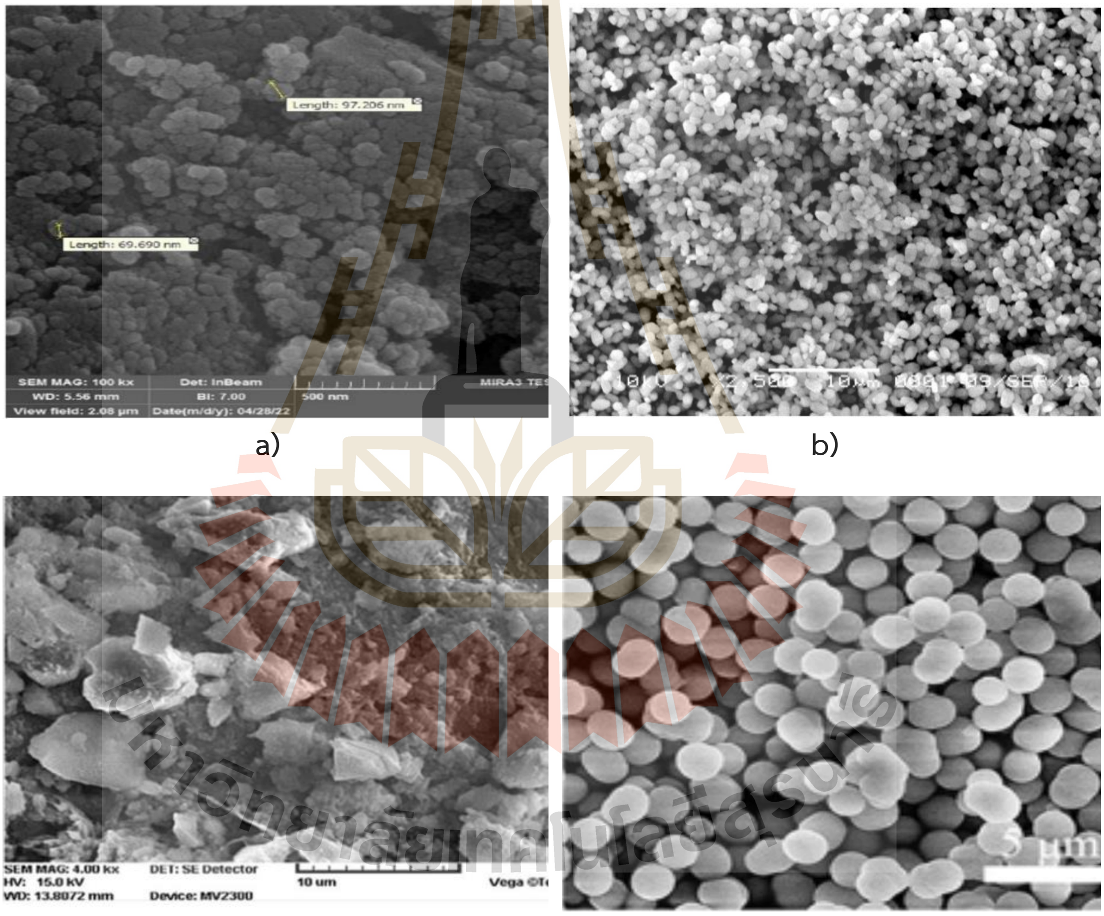

a) b)

c) d)

Figure 2.15 FE-SEM images of a) Silica extracted from rice husk (Shiva, Golmohammadi et al., 2023), T-type zeolite synthesized using bamboo leaves (Setiadji, Sundari et al., 2018), c) sugarcane bagasse (Prabha, Durgalakshmi et al., 2021), and d) SiO_2 nanospheres from rice husk (Cui, Liang et al., 2016).

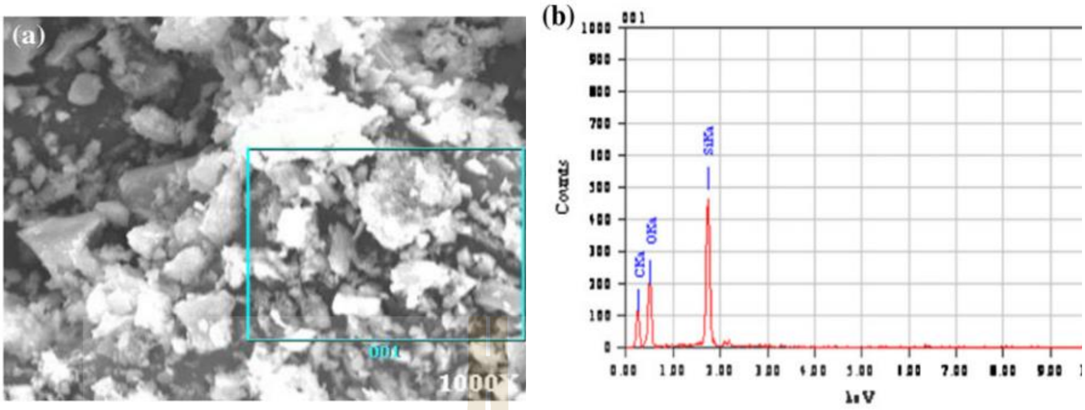

a) b)

Figure 2.16 A SEM image, and b EDS of silica from rice husk (Deshmukh, Bhatt et al., 2012).

However, the SiO_2 distribution on surface of particles able to study with Energy Dispersive X-Ray Spectroscopy EDS and mapping image after take a photo by FE-SEM. Moreover, the EDS and mapping technique were employed in this study to investigate the Si composition and comparison of the Si composition with other technique. The detailed results of material component and element distribution reveal in Figure 2.16 and Figure 2.17.

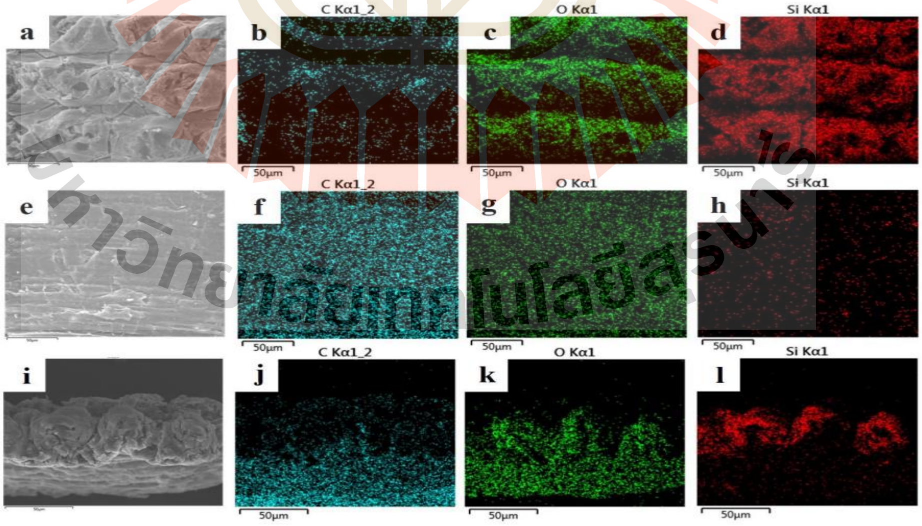

Figure 2.17 SEM-EDX images of treated RH1: (a)-(d) outer surface, (e)-(h) inner surface, and (i)-(l) cross-sectional surfaces (Boonsuk, Sukolrat et al., 2021).

To examine the post-synthesis growth of particles, this study employs a transmission electron microscope (TEM). The TEM technique provides high-resolution imaging of particles by transmitting electrons through them, enabling detailed visualization of the internal structure of SiO_2 nanoparticles, as confirmed in this work. Moreover, the TEM image was used in confirmation the crystalline and amorphous, which is shown in selected area electron diffraction image, as depicted in Figure 2.18.

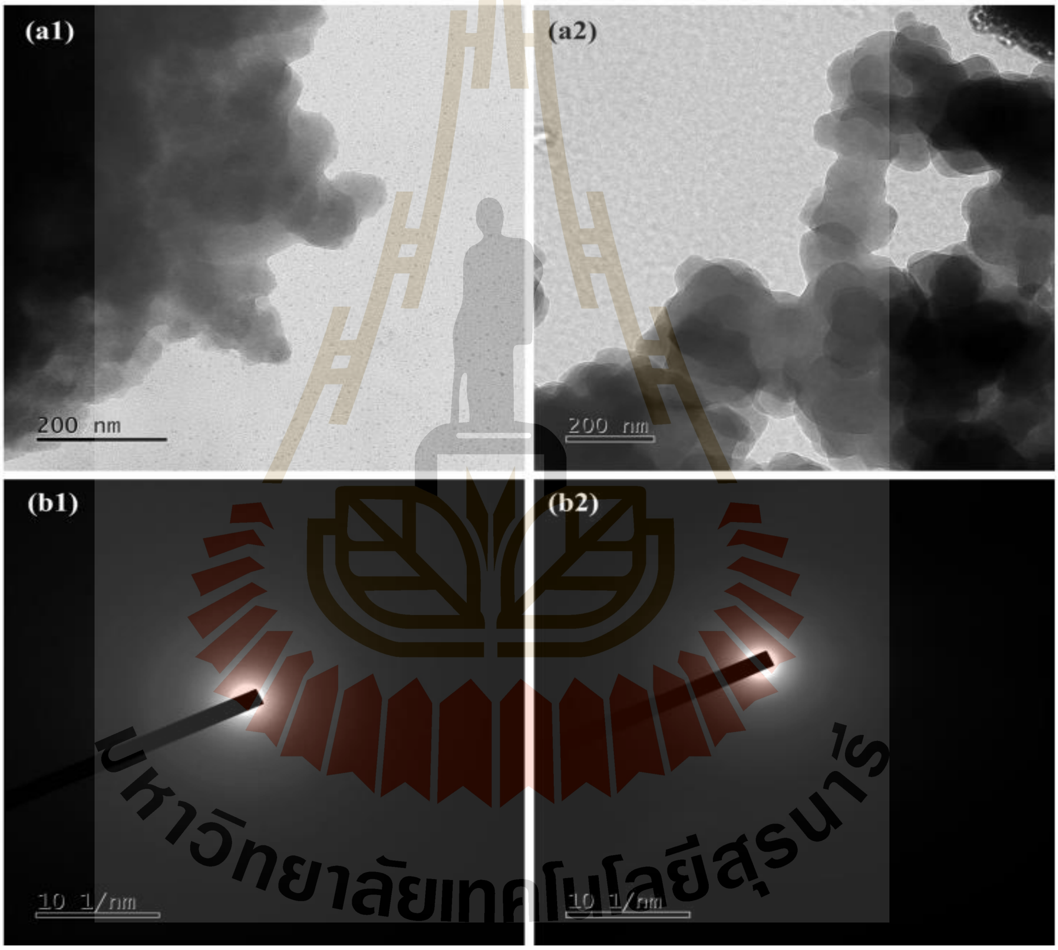

Figure 2.18 a TEM, and b SAED image of RHA-Silica and C-Silica (Nayak and Datta, 2021).

2.11 X-ray absorption spectroscopy (XAS)

To the investigate the electronic and the structural properties of material, this work provide the detailed information about local atomic structure by X-rays absorption spectroscopy (XAS). The X-rays absorption spectroscopy is a powerful analytical technique use for studies of structural properties of materials at atomic level. The XAS theory base on absorption the X-rays energy from the photoelectric effect, where an incident X-ray photon ejects an inner-shell electron, leaving behind a core hole. The core hole level can be divided into three level: K-shell, L-shell, and M-shell (See in Figure 2.19).

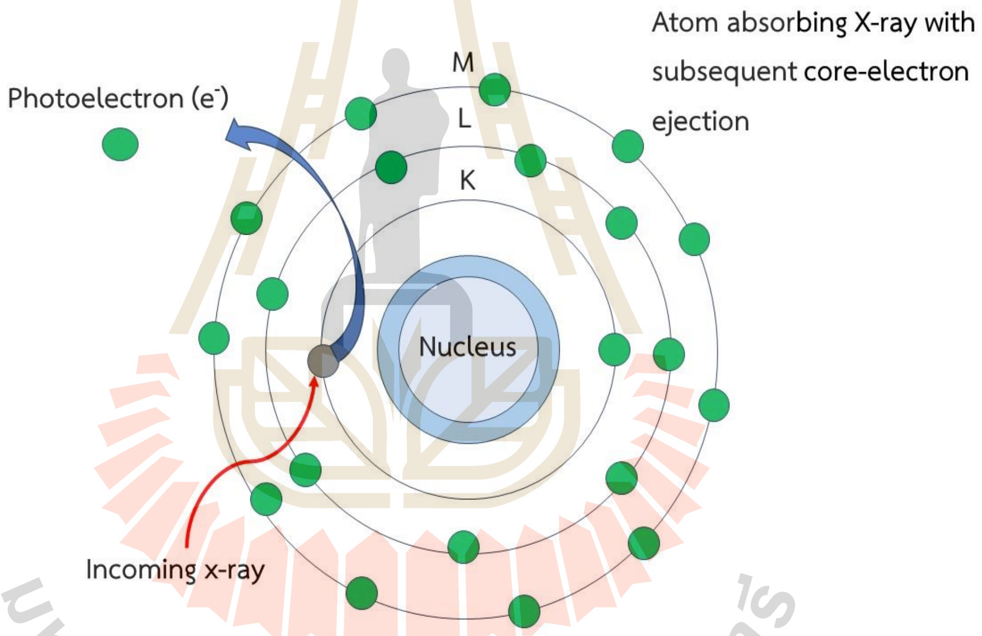

Figure 2.19 The activities of x-ray on electron in K-shell.

The X-ray absorption spectrum typically exhibits a shape increase in absorption at the certain energies, which is called absorption edges. The absorption edges depend on specific electronic transition in atom, typically involving the excitation of an electron from a core level to an unoccupied higher energy level, as illustrated in Figure 2.20

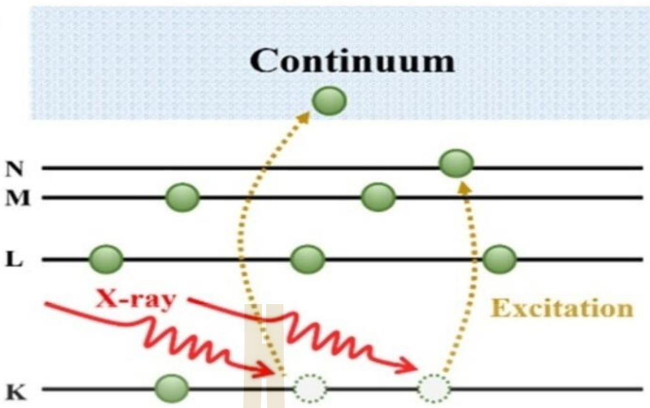

Figure 2.20 Schematic diagram illustrating electrons in an absorbing atom being excited by X-ray (Wu, Sun et al., 2023).

For the spectrum of XAS, can be classifies into two categories: X-rays Absorption Near-Edge Structure (XANES) and Extended X-ray Absorption Fine Structure (EXAFS).

Mostly, XANES used typically provide the information of oxidation state, coordinate environment, and symmetric of the absorbing atom. For EXAFS provides information local atomic structure around the absorbing atom including bond lengths, and coordination geometries. The XANES and EXAFS spectrum was illustrated in Figure 2.21

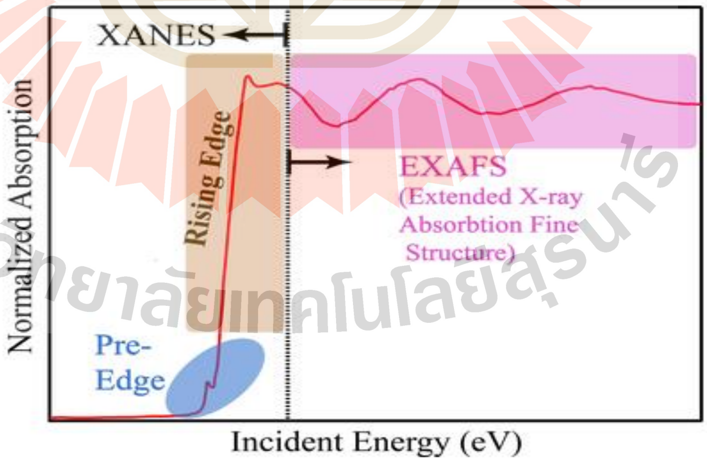

Figure 2.21 A schematic XAS spectrum highlighting the main peak regions and their sources. Two distinct regions, XANES and EXAFS, depict the local electronic structure of materials (Jungho, 2021).

For XAS measurement can be measured into 3 modes: transmission, fluorescent, and electron yields. Transmission mode employed in this study to investigate the information of the electronic and the structural properties of SiO_2 nanoparticles. In experiment, we measure the X-rays intensity: I_0 and I_1, which is in the form of electric current. The I_0 and I_1 were measured by electrometer, it can be represented following Equation (2.5).

$$I_1(E)= I_0(E)e^{-\mu(E)x} \tag{2.5}$$

Where μ is absorption coefficient and x thick of sample. The spectrum of electric current intensity was shown in energy absorption spectrum μ(E).

Moreover, information about the local atomic structure around the absorbing atom was calculated from the interference of photoelectrons, which occurs due to the scattering of neighboring atoms. The local atomic structure is represented by a sine function, as revealed Equation (2.6).

$$\chi(k) = \sum_f \frac{s_0^2 N_j f_j(k) e^{-2k^2\sigma_j^2} e^{-\frac{2R_j}{\lambda(k)}}}{kR_j^2} \sin[2kR_j - \delta_j(k)] \tag{2.6}$$

where s_0^2 is amplitude reduction term, N_j is coordination number of neighbour atom, $f_j(k)$ is photoelectron scattering properties of neighbouring atom, R_j is distance to neighbouring atom, and σ_j^2 is mean-square disorder of neighbour atom.

CHAPTER III

RESERCH METHODOLOGY

3.1 Research Procedure

3.1.1 Materials

3.1.1a Hydrochloric acid (HCl) was purchased from Labscan Limited Co., Ltd

3.1.1b Nitric acid (HNO_3) was purchased from Ajax Finechem Pty, Ltd

3.1.1c Silicon dioxide (SiO_2) was synthesized from Actinoscirpus grossus leaf (AGL) that AGL come from Mahasarakham province in northeastern region of Thailand

3.1.1d Silicon dioxide was purchased from Sigma Corporation of America, Sigma Imaging (UK) Ltd.

3.2 SiO_2nanoparticles preparation

The Actinoscirpus grossus leaves (AGL) were washed with water to remove dirt and dried in sunlight for two days. The dried AGL was cut into small pieces and washed three times with deionized (DI) water. Afterward, the wet AGL was dried in an oven at 125°C for 12 hours. A 37% HCl solution was used for hard dirt leaching with varying acid concentrations. The acids were mixed with DI water under magnetic stirring at concentrations of 0, 0.1, 0.5, 1, and 5 molars. The pH of the HCl solutions was 1 (for LS-HCl 0.1M), 0.3 (for LS-HCl 0.5M), 1 (for LS-HCl 1M), and -0.7 (for LS-HCl 5M). The small AGL pieces were mixed with the acid solution at a weight ratio of 50g AGL to 1000ml acid solution and heated at 70°C for 3 hours on a hotplate. The AGL was then washed three times with DI water and soaked in DI water for 24 hours. After soaking, the AGL samples were filtered using a plastic strainer and dried in an oven at 125°C. Finally, the dried AGL samples were burned at 700°C for 3 hours in a furnace.

Figure 3.1 The step of SiO_2 nanoparticles synthesis by 1st HCl etching.

3.3 Advanced SiO_2 nanoparticles preparation

The advanced synthesis of SiO_2 nanoparticles was achieved using the etching method. After burning the AGL samples at 700°C, the resulting SiO_2 nanoparticles were mixed with an acid solution at a concentration of 0.1 molars, with a weight ratio of 5g to 250ml. The SiO_2 solution was stirred at 70°C for 1 hour on a hotplate and then filtered using filter paper. Finally, the wet SiO_2 on the filter paper was dried in an oven at 100°C for 20 minutes.

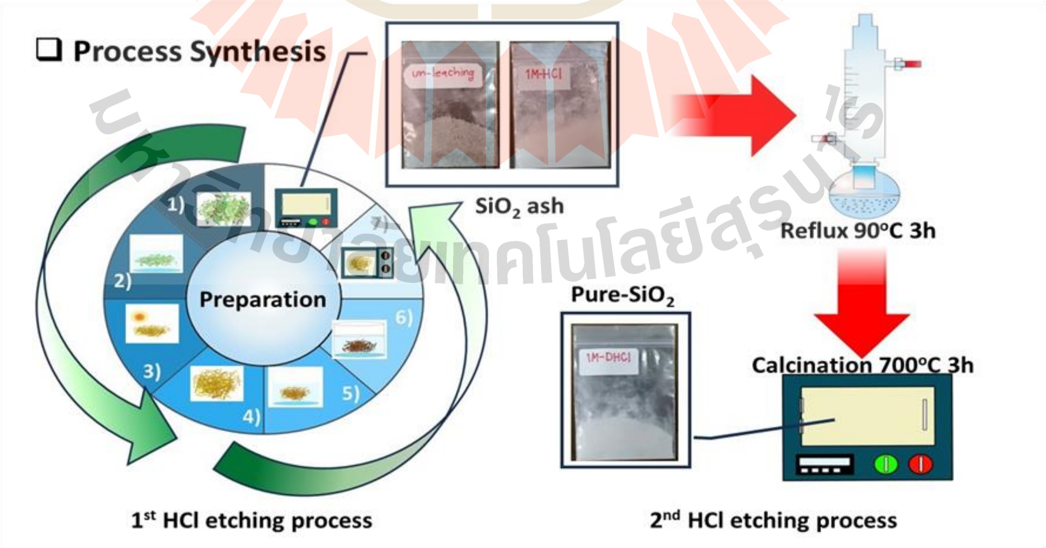

Figure 3.2 The step of pure SiO_2 nanoparticles synthesis by 2st acid etching.

3.4 Measuring instrument and characterized

1) The mass change and thermal effect of silica-powders during heating were determined by thermogravimetric analysis (TGA) and differential scanning calorimetry (DSC). NETZSCH STA 449 F3 Jupiter® were used to analyze the thermal effect that all samples were heated from 30 to 950°C with the heating rate 5°C/min under nitrogen atmosphere. The NETZSCH STA 449 F3 Jupiter® exhibits in Figure 3.3.

Figure 3.3 NETZSCH STA 449 F3 Jupiter® – Thermal Analysis System.

2) The crystallographic structure and physical properties of the materials were explained by the X-rays diffraction (XRD). XRD is diffraction of wave after interference pattern of the wave-occurred. The condition of X-ray diffraction is a related to the following Bragg's Law equation. The instrument in this experiment is model of Bruker D8 ADVANCE at Suranaree University of Technology (SUT). The diffraction angles used in this experiment ranged 20°-80° with time/step of 1.5s per step, as revealed in Figure 3.4

.

Figure 3.4 Powder X-ray Diffraction (XRD), Bruker D8 ADVANCE.

3) Element analysis is explained by X-rays fluorescence (XRF). The mass of atomic element in wide range of material was measured by the X-ray fluorescence (XRF) analysis. The experimental measurement was used Energy Dispersive X-ray Fluorescence (EDXRF), Horiba XGT-5200 X-ray analytical microscope at Suranaree university of technology (SUT), as shown in Figure 3.5. The elements used in this measuring consists of 10 elements: Si, K, Ca, P, Mn, Fe, Cl, Mg, Na, and Mn with the preset time 1500s at 30kV.

Figure 3.5 Energy Dispersive X-ray Fluorescence (EDXRF) XGT-5200.

4) The absorption, emission, and photoconductivity of material can be measured by Fourier Transform Infrared Spectroscopy (FT-IR). FT-IR data show the spectrum of vibration bonds in the material. The vibration bond can be classified into two: stretching vibration and bending vibration. These vibrations will relate to the specific bond of the elemental compound. Hence, organic and inorganic bonds of material can explain by FT-IR. In the thesis, FT-IR was used to explain and study the organic and inorganic bonds of all samples. The wavenumber from 4000 to 400 cm^{-1} in all samples will be used for the study of bonding energy by using Fourier Transform Infrared Spectroscopy (FT-IR), Tensor 27 at Suranaree university of technology (SUT) as revealed in Figure 3.6.

Figure 3.6 Fourier Transform Infrared Spectroscopy (FT-IR), Tensor 27.

5) To capture the morphological image for microstructure of material, Field Emission Scanning Electron microscope (FE-SEM) will be used. In general, FE-SEM image uses the principle of inelastic interaction between electron beam and atom on surface of material. The products of inelastic interaction will release variety of the signal. The signal for taking an image is used an energy secondary electron from electron scattering. The principles of FE-SEM and SEM have a little bit different due to FE-SEM using the electric field for electron beam production whereas SEM uses an electron gun for electron beam production. From these different principles, the FE-SEM image have higher resolution than SEM due to the electron beam of FE-SEM being smaller than SEM. Hence, FE-SEM was used to study the morphology of AG in this thesis. In

addition, the elemental composition at surface of all samples was explained by Energy-dispersive X-ray spectroscopy (EDS). Therefore, Field Emission Scanning Electron Microscope (FE-SEM), Zeiss AURIGA FE-SEM/FIB/EDX at Suranaree university of technology (SUT) as revealed in Figure 3.7. was used for the experimental measurement.

Figure 3.7 Field Emission Scanning Electron Microscope (FE-SEM), Zeiss AURIGA FE-SEM/FIB/EDX.

6) The detailed morphology of the nanoparticles will be studied by transmission electron microscope (TEM). TEM is a technique that used to take a morphological image of nanoparticles as same as FE-SEM technique but the principle is different. TEM use transmission of electron for the creation of image. The tension energy of the TEM technique is 60-300 kV, which is higher than SEM (1-30 kV). Moreover, the type of image is 2-D and magnification is above 50 million times. Thereby, the direct information of local structure at the atomic level of material was exhibited the information by TEM. In this thesis, Transmission Electron Microscope (TEM), FEI Tecnai G^2 20 200kV TEM/STEM/EDX/Tomography at Suranaree University of Technology (SUT) as revealed in Figure 3.8 was used for the experimental measurement.

Figure 3.8 Transmission Electron Microscope (TEM), FEI Tecnai G^2 20 200kV TEM/STEM/EDX/Tomography.

7) The oxidation, the structure of atom, wavelength, and molecular form will be interpreted by X-rays absorption spectroscopy (XAS). XAS data can be divided into two areas by considering edge absorption: X-ray Absorption Near Edge Structure (XANES) and Extended X-ray Absorption Fine Structure (EXAFS). XANE spectrum is absorbed photon energy at about 50 eV, which is used to the oxidation-derived of material. EXAFS spectrum is an emission photon in the absorption process (the range of energy around 500-1000 eV). Thereby, this thesis is interested in the use of XANES and EXAFS for the studying defect of SiO_2 after chemical and thermal treatment. The experiment will be performed at the synchrotron light research institute

CHAPTER IV

RESULTS AND DISCUSSION (PART I): EFFECT OF HYDROCHLORIC ON SIO$_2$ NANOPARTICLE DERIVED FROM ACTINOSCIRPUS GROSSUS

In this chapter, the investigation of the structural properties of SiO$_2$ derived from Actinoscirpus grossus via hydrochloric acid etching. The properties of formation-structure of SiO$_2$ ash are presents in the form of materials purity. Consequently, the point of this chapter, it focuses on the synthesis of SiO$_2$ ash powder and descriptions the effect of hydrochloric on SiO$_2$ ash powders.

4.1 Hydronium ion from hydrochloric

The common name for the cation [H_3O^+] called in name of hydronium ion. Hydronium ion able to prepared from chemical reaction between acids and pure water. In this experiment, the hydronium ion was prepared from hydrochloric acid and DI-water, which the reaction of hydrochloric acid and DI-water able to follow Equation (4.1).

$$H_2O(aq) + HCl(aq) \longrightarrow H_3O^+(aq) + Cl^-(aq) \tag{4.1}$$

From the production of this reaction, it is very important for chemical decomposition in this work. In experiment, hydronium ion was prepared in 1000ml water, which has varying concentrations: 0, 0.1, 0.5, and 5 molarity. From concentration of solutions, we known that the power of hydrogen (PH) of solutions of hydronium ion at 0.1, 0.5, 1, and 5 molarity are 1.0, 0.3, 0, and -0.7, respectively. The PH able to calculate by the formular is:

$$pH = -\log[H^+] \tag{4.2}$$

where [H^+] is the concentration of hydrogen ion

4.2 The production of Actinoscirpus Grossus (AG) ash through hydrochloric acid etching

In this work, hydronium ion from hydrochloric was used into a reagent of chemical reaction for preparing SiO_2 ash. The preparing SiO_2 ash was prepared by acidic etching to varying concentrations of hydrochloric acid: 0, 0.1, 0.5, and 5 molarity. The process underwent boiling with HCl at $90^{o}C$ for 2 hours.

During this process, hydrochloric acid (HCl(aq)) interacted with compounds on the material's surface (surface of AG blade leaf). In the reaction, firstly, element oxide on material’s surface was decomposed a bond of compound, which depends on hydronium ion steals an electron from element oxide to produce a water. In addition, choline was interacted with element after decomposed compound.

After reactions, final products of new compounds were in solution forms. Normally, the element oxide on material’s surface of AG blade leaf, it is normal element oxide from soils, including CaO, K_2O, Fe_2O_3, P_2O_5, and MnO_2. Therefore, mostly, final product of chemical reaction in this step able to follow by Equation (4.3-4.6).

$$CaO(s)+2H_3O(aq)+2Cl(aq) \xrightarrow{90^{o}C\ 3h} CaCl_2(aq)+3H_2O(l) \qquad (4.3)$$

$$K_2O(s)+2H_3O(aq)+2Cl(aq) \xrightarrow{90^{o}C\ 3h} 2KCl(aq)+3H_2O(l) \qquad (4.4)$$

$$Fe_2O_3(s)+6H_3O(aq)+6Cl(aq) \xrightarrow{90^{o}C\ 3h} 2FeCl_3(aq)+9H_2O(l) \qquad (4.5)$$

$$P_2O_5(s)+2H_3O(aq)+6Cl(aq) \xrightarrow{90^{o}C\ 3h} 2PCl_3(aq)+6H_2O(l) \qquad (4.6)$$

$$MnO_2(s)+2H_3O(aq)+2Cl(aq) \xrightarrow{90^{o}C\ 3h} MnCl_2(aq)+2H_2O(l) \qquad (4.7)$$

The effect of HCl on Actinoscirpus grossus samples was compared by dividing them into five groups, each treated with a different concentration of acid, as seen in Figure 4.1.

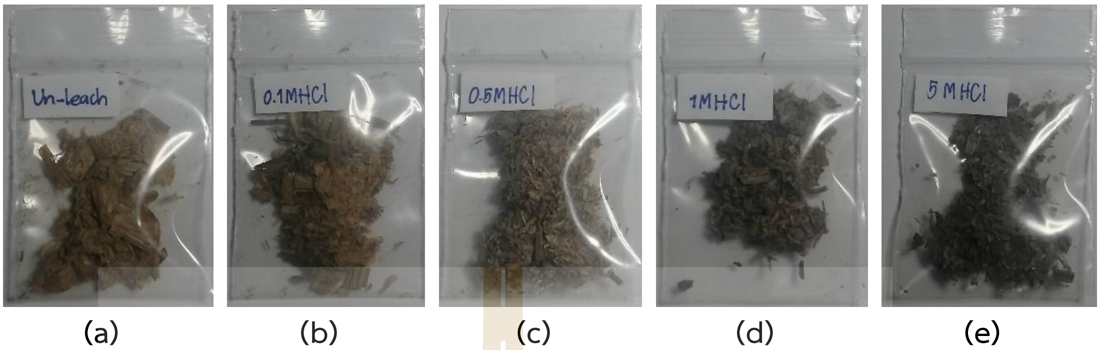

Figure 4.1 Raw material samples: un-leaching, LS-HCl 0.1M, LS-HCl 0.5M, LS-HCl 1M, and LS-HCl 5M.

4.3 The calcination of Actinoscirpus grossus

In the experiment, Actinoscirpus grossus processed through calcination was selected based on data generated by TG/DTA and DSC measurements. During calcination, the thermal properties of the materials revealed the formation of thermal effects on the Actinoscirpus grossus samples. The temperature employed for the measurements ranged from 30°C to 950°C in air, and this range was classified into three sections: A zone (30-200°C), B zone (200-500°C), and C zone (500-950°C). In zone A, the temperature-related chemical decomposition involved the evaporation of moisture (O-H functional group and O-H structure). In zone B, the thermal breakdown of chemicals was observed, mainly involving the degradation of hemicellulose, cellulose (Lee, Othman et al., 2013), nitrogen compounds, long-chain hydrocarbons, aromatic and polyheterocyclic compounds (Trompowsky, de Melo Benites et al., 2005; Zhang, Du et al., 2011; Boguta, Sokołowska et al., 2017). Finally, the chemical decomposition in zone C was related to the cleavage of the C-C bond (Fernández, Hockaday et al., 2008).

Comparative TG and DSC results regarding the influence of HCl on Actinoscirpus grossus samples are shown in Figures 4.2 and 4.3. As illustrated in Figure 4.3, both the HCl sample without leaching and the LS-HCl 1M sample exhibit weight losses below 750°C. The weight losses for both samples begin below 150°C, corresponding to moisture evaporation in the samples' cells. The weight reductions in zone A for the HCl sample without leaching and the LS-HCl 1M sample are 4.08% and 10.22%, respectively. Comparing the two samples after the weight decrease in zone A, the LS-HCl sample shows a more substantial weight reduction than the un-leached sample. Subsequently, there is a much sharper decline in weight from approximately 250°C to 400°C due to the decomposition of fibers, hemicellulose, and cellulose. Additionally, carbon oxides, alkenes (C=C), and nitrogen compounds decompose within the temperature range of 450-500°C, as indicated in zone B. In zone B, the weight losses for the un-leached sample and the LS-HCl sample are 38.48% and 51.87%, respectively.

Additionally, weight loss due to thermal decomposition was observed in zone C at temperatures of 635°C and 820-850°C, corresponding to the cleavage of the C-C bond (Fernández, Hockaday et al., 2008) and the formation of CO_2, respectively. At 950°C, the residual mass of the un-leached sample and the LS-HCl 1M sample is 50.79% and 32.25%, respectively. The higher residual mass of the un-leached sample indicates that it contains a greater number of elemental oxides in its structure compared to the LS-HCl 1M sample after complete calcination.

However, the thermal reaction on TG curve able to confirm with DSC spectra as shown in Figure 4.3. At A zone of thermal range of Un-leaching sample was found small endothermic reaction in 1st and 2nd of state which ΔH is -0.298mW/mg and -0.081mW/mg, respectively. The small endothermic reaction over A zone is confirm a moisture evaporation of O-H structure. Likewise, the state of 3rd, 4th, and 5th shows the combustion of cellulose, N-compound, and C-C bond which ΔH is -0.721mW/mg, -5.082mW/mg, and -6.981mW/mg, respectively.

Likewise, DSC spectra of LS-HCl sample has four state of endothermic reaction which ΔH of endothermic reaction at state of 1st, 2nd, 3rd, 4th is -6.981, -0.738, -0.539, and -5.141mW/mg, respectively. Furthermore, as depicted in Figure 4.4a, an examination of residual mass during HCl leaching at concentrations ranging from 0.1 to 5M reveals that the residual mass after heating from 30 to 950°C falls within the range of 23-32% at 948°C, showing stability beginning at 700°C. Consequently, this experiment aimed to synthesize at a calcination temperature of 700°C. Additionally, the DSC spectra for all samples exhibit slight variations in the decomposition process pattern following HCl treatment, attributed to their similar material purity and minor structural differences, as illustrated in Figure 4.4b.

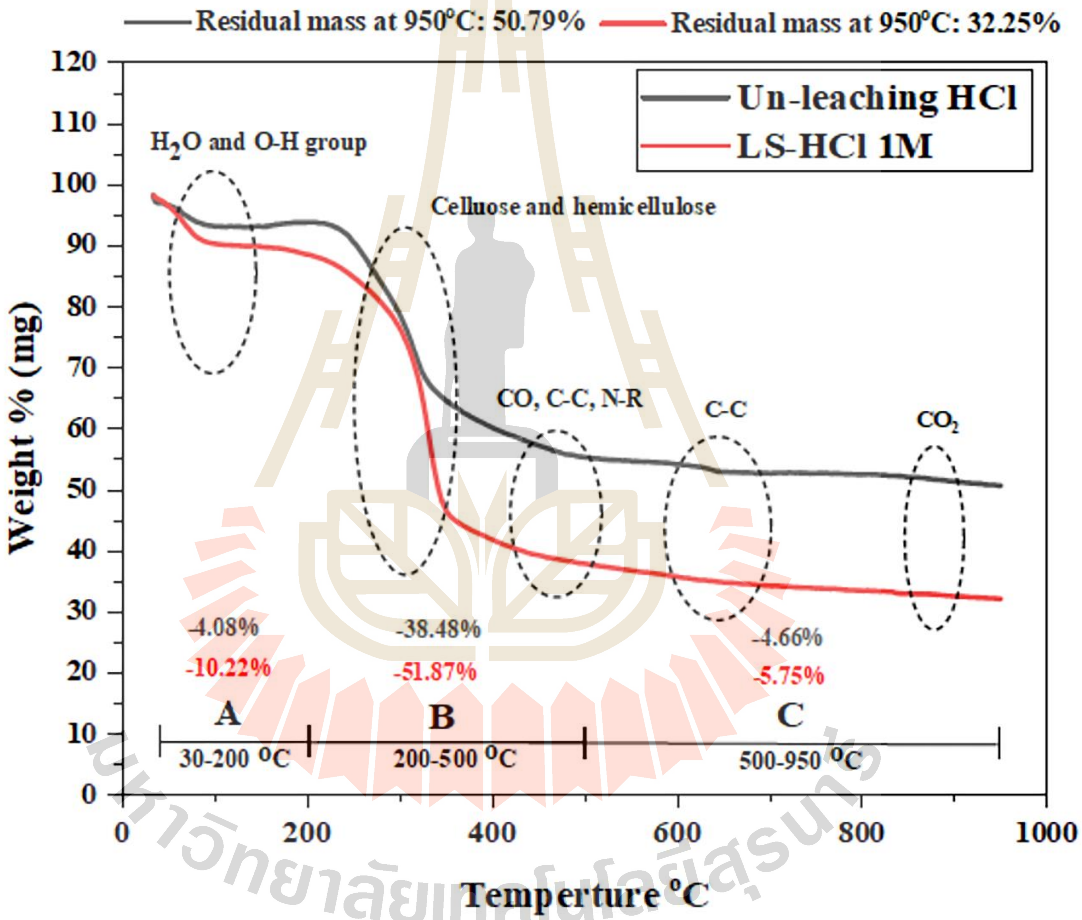

Figure 4.2 TG curve of Actinoscirpus Grossus ash derived via non hydrochloric etching (Un-leaching HCl sample) and hydrochloric etching (LS-HCl 1M sample).

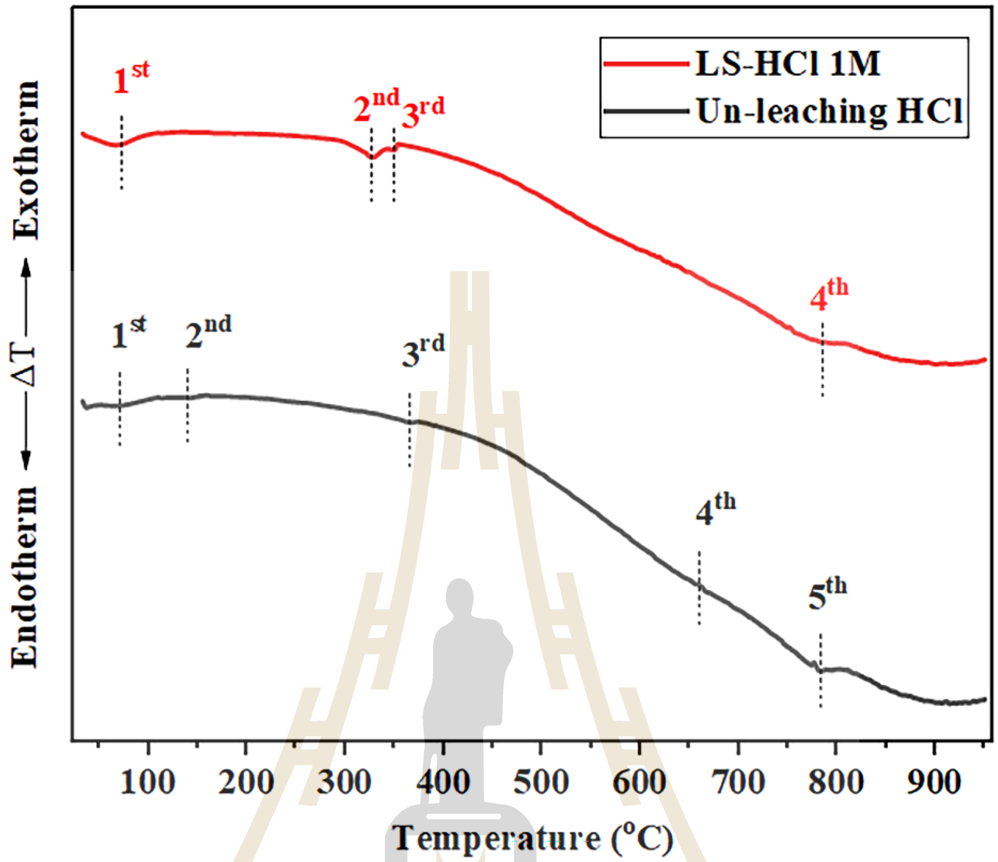

Figure 4.3 DSC curve of Actinoscirpus Grossus ash derived via non hydrochloric etching (Un-leaching HCl sample) and hydrochloric etching (LS-HCl 1M sample).

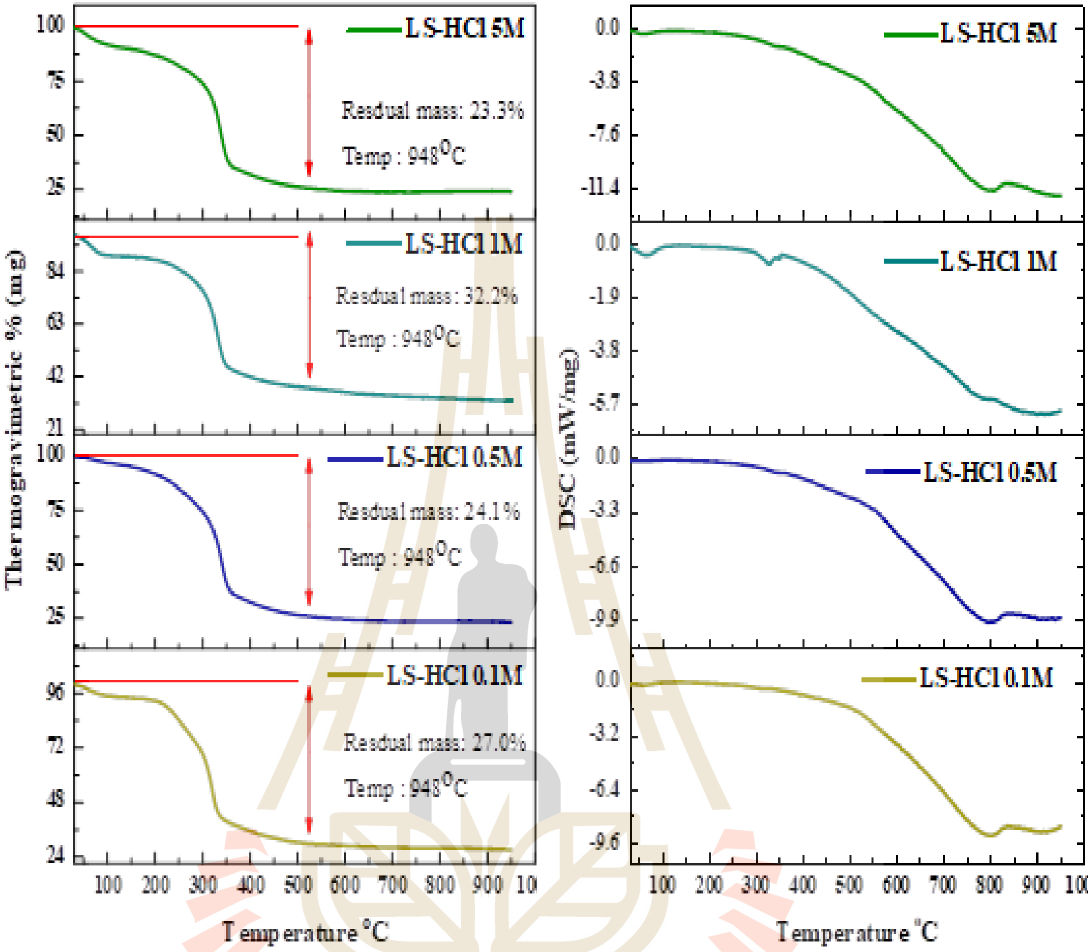

(a) (b)

Figure 4.4 Thermal analysis of SiO_2 nanoparticles a) TGA spectra of (0.1-5 M) LS-HCl and b) DSC spectra of (0.1-5 M) LS-HCl samples.

(a) (b) (c) (d) (e)

Figure 3.5 SiO_2 powders samples: un-leaching, LS-HCl 0.1M, LS-HCl 0.5M, LS-HCl 1M, and LS-HCl 5M.

Furthermore, following calcination at 700°C, the powder exhibits a range of colors, including black, grey, and white. Black and grey were detected in the un-leached HCl sample, while white powder was identified in the sample treated with hydrochloric acid, as illustrated in Figure 4.5. X-ray diffraction (XRD) results revealed the diffraction patterns of the ash powders, indicating various structures in the un-leached samples, as shown in Figure 4.6. The XRD pattern identified the polycrystalline forms of potassium chloride (KCl), calcium manganese carbonate ($CaMn_2CO_6$), and quartz. The patterns of KCl and $CaMn_2CO_6$ were verified using the reference patterns ClK01-075-0296 and C_2CaMnO_6 01-084-1290, respectively. The quartz peaks appeared at 26.6°, 36.4°, and 50.4°, consistent with SiO_2 00-004-0379. However, the polycrystalline peaks of the un-leached HCl sample could not explain all observed peaks, indicating the presence of significant impurities. This result confirms that if the samples are not washed with HCl, alkaline substances cannot be removed, resulting in a greater quantity of impurities in the sample.

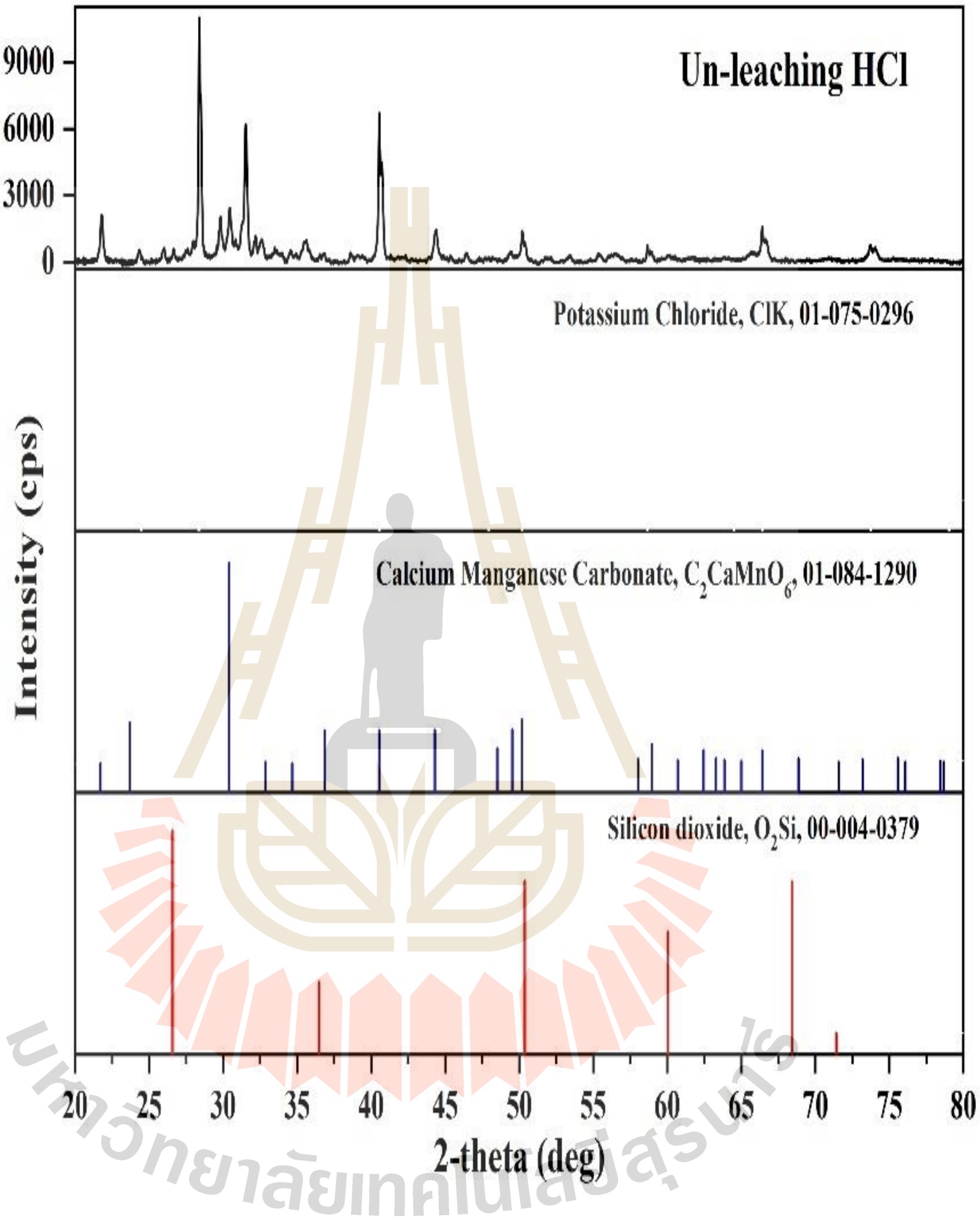

Figure 4.6 XRD pattern of un-leaching HCl and leaching sample by HCl 1M on scan range of 2-theta (20-80 deg).

Moreover, an amorphous form of SiO_2 was observed after the samples were leached with HCl, as shown in Figure 4.7. The XRD pattern in Figure 4.7, for samples treated with HCl concentrations ranging from 0.1 to 5 M, illustrates the emergence of crystalline silica with increasing HCl concentration. The SiO_2 crystalline form is clearly identified as quartz, with distinctive peaks at 20.8° and 26.6°, confirming the presence of quartz (O_2Si, 00-001-0649), consistent with findings reported by Kosmachev et al. (Kosmachev, Vlasov et al., 1800). Additionally, peaks at 21.8°, 28.3°, and 31.6° indicate the cristobalite form of SiO_2, as confirmed by Cristobalite (O2Si, 00-004-0379) and suggested by Ghasemi and Younesi (Ghasemi and Younesi, 2011). The presence of cristobalite and quartz in the structure may be attributed to the simple agglomeration of SiO_2 nanoparticles on the surface following the etching process with HCl and calcination at 700°C for 3 hours.

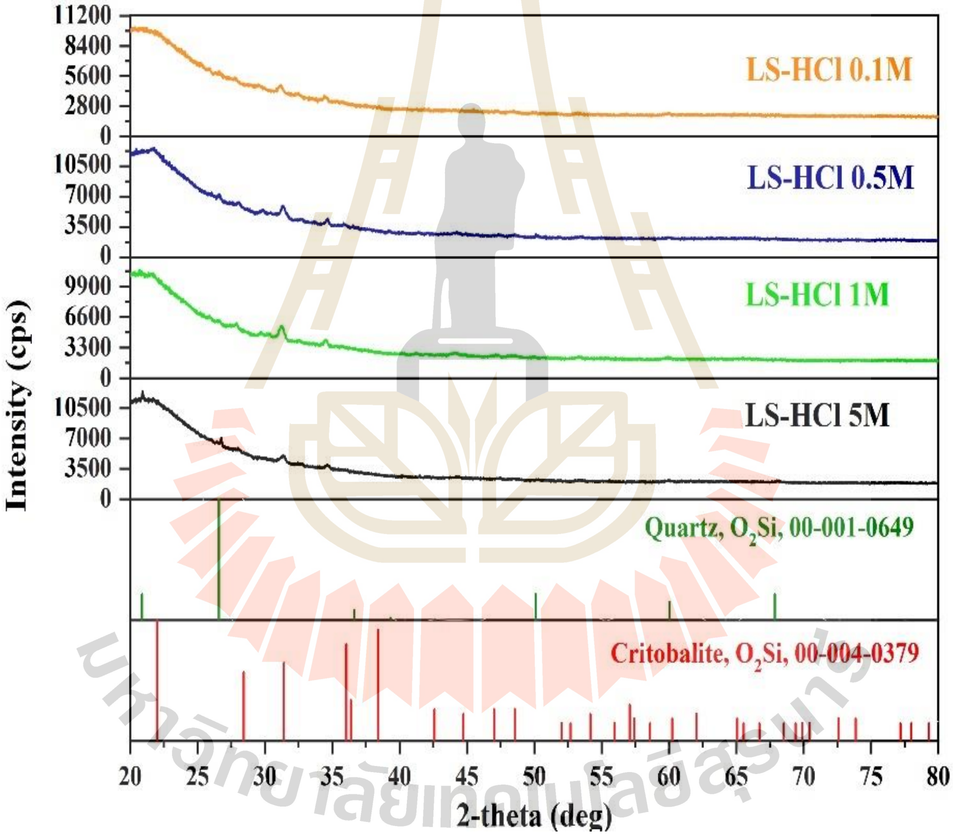

Figure 4.7 The XRD pattern of LS-HCl (0.1-5M) and peaks position of quartz and cristobalite.

In this study, material purity was assessed based on the mass fraction. The elemental composition of all samples was analyzed using ED-XRF, and the mass fractions of elemental oxides in all samples are presented in Table 4.1. Table 4.1 lists eight elements in AGL ash: CaO, K_2O, SiO_2, P_2O_5, Fe_2O_3, MnO_2, SO_3, and Cl. The SiO_2 mass fraction in the un-leached HCl sample is 53%. However, after adding AGL to the HCl solution, the SiO_2 content increased to over 90%, while other elements were reduced to less than 5%. This change is attributed to the decomposition process (Liou, 2004; Tipsotnaiyana et al., 2012), as described in the acid treatment process above. The final product, which is in an aqueous form, shows a decrease in elemental oxides other than SiO2 after filtration. In the experiment, the highest SiO_2 mass fraction achieved was 97.24% with 1M HCl, indicating a high-purity SiO_2 compared to other reports on SiO_2 extraction from plants, as shown in Figure 4.8. Additionally, variations in SiO_2 content can be explained by SiO_2 yield, which increases with higher HCl concentrations. The maximum SiO_2 yield reached 83%, as shown in Table 4.2. This increase suggests that higher HCl concentrations accelerate the decomposition rate of the chemical reaction.

Table 4.1 The percentages of elemental oxide components in all samples derived from AGL ash.

Samples	Mass fraction of the element and element oxide (%)							
	SiO_2	K_2O	CaO	P_2O_5	Fe_2O_3	MnO_2	SO_3	Cl
un-leaching HCl	53.18	8.84	18.31	13.27	0.25	1.36	4.38	0.43
LS-HCl 0.1M	91.37	0.99	1.63	4.38	0.09	0.19	1.36	-
LS-HCl 0.5M	94.36	1.23	1.30	1.65	0.04	0.17	1.26	-
LS-HCl 1M	96.24	0.32	0.24	1.08	0.03	0.07	0.32	-
LS-HCl 5M	96.75	0.45	0.49	1.62	0.02	0.08	0.58	-

Table 4.2 The variation in SiO_2 yields among all samples derived from AGL ash.

Samples	LS-HCl 0.1 M	LS-HCl 0.5 M	LS-HCl 1 M	LS-HCl 5 M
SiO_2 yields	71.8	77.4	82.9	82.0

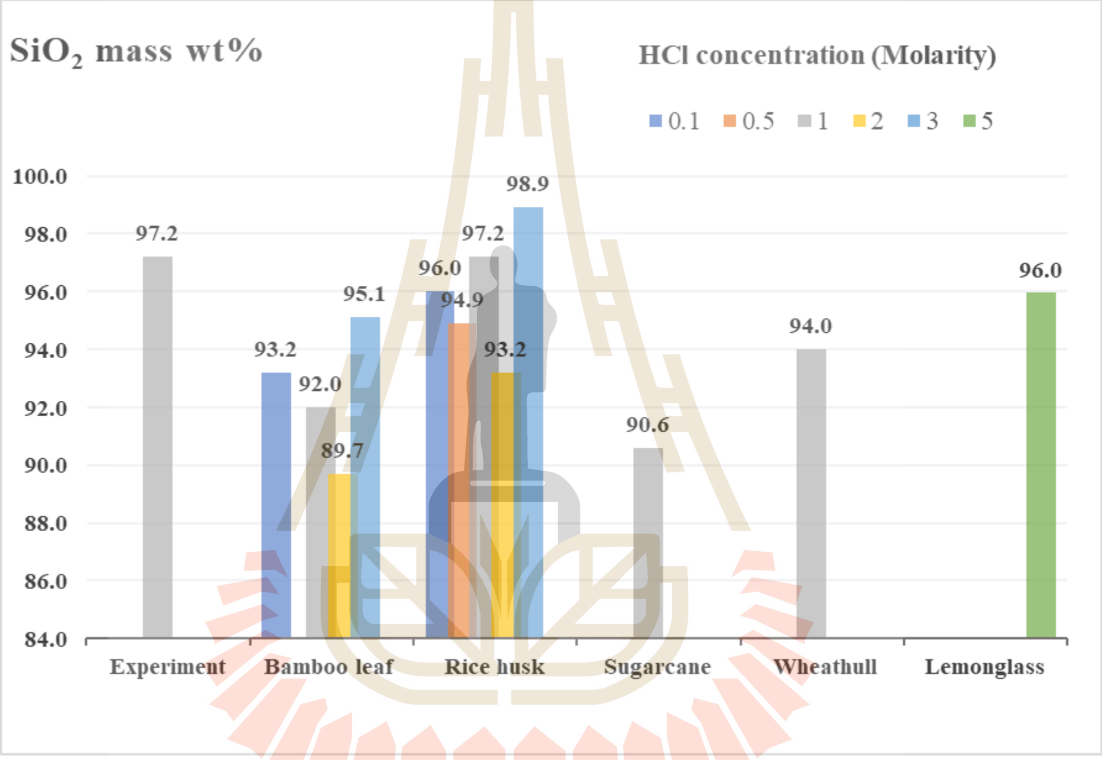

Figure 4.8 The comparison of mass fraction SiO_2 of experiment, bamboo (Manurung, Siregar et al., 2019, Phomketjan and Wongprayoon, 2020), rice husk (Tipsotnaiyana, Jarupan et al., 2012, Nuruddin, Saad et al., 2016, Azat, Sartova et al., 2019, Jamil and Zarib, 2019), sugarcane (Huabcharoen, Wimolmala et al., 2017), wheat hull (Terzioğlu, Yucel et al., 2013), and lemon glass (Firdaus, Osman et al., 2016).

Additionally, FT-IR spectroscopy was employed as a common technique to characterize organic and inorganic components within the material. In this study, FT-IR was utilized to investigate the structure of the white powder post-calcination, as illustrated in Figure 4.9a and 4.9b. Figure 4.9a and Figure 4.9b shows the transmittance spectrum of SiO_2 nanoparticles between un-leaching HCl and LS-HCl. Figure 4.9a reveals an overview of the function group in the range IR spectrum of 400-4000 cm^{-1}. Small peaks at 3627-3730 and 3760 cm^{-1} represent the free O-H group (Belskaya, Danilova et al., 2012) and O-H stretching (Alemdar, Güngör et al., 2005).

Additionally, C-H stretching and C-H bending of SiO_2 nanoparticles were corresponding to the peaks at 2800-3000 and 1462 cm^{-1}(Savchenko, Vorliček et al., 2017). Peaks at 2080, 1987, 1650, and broad peak of 1187-1200 cm^{-1} were shown the stretching vibration of $R\text{–}NH_3^+$ and N-H group of cysteine (Li, Liao et al., 2017), carbonyl (Kaiser and Knör, 2015), and oxygen hydride (Park, Kim et al., 2019), respectively. Furthermore, the IR spectrum of SiO_2 is appeared in the wavenumber under 1100 cm^{-1}, as shown in Figure 4.9b. In the spectrum of SiO_2, three functional groups are observed: asymmetric stretching (at 1090-1030 cm^{-1}, Si-O-Si), symmetric stretching (at 800 cm^{-1}, Si-O-Si) (Liang, Ouyang et al., 2012), and Si-OH bond vibration at 963 cm^{-1} (Yan, Jiang et al. 2014). Additionally, other features in the IR spectrum include C-O stretching (Montazeri-Pour, Ataie et al., 2008) at 914 cm^{-1}, $CaCO_3$ (Reig, Adelantado et al., 2002) at 875 cm^{-1}, and C-H groups (Ibrahim, Yunus et al., 2013) at 860 cm^{-1}.

In Figure 4.10, it can be observed that the symmetric and asymmetric peaks in the SiO_2 spectrum the same position and curve, indicating that the SiO_2 structure remains a little changed after HCl increases. The change of the symmetric and asymmetric peaks considered within absorbance spectrum. The absorbance spectrum able to follow by Equation (4.8).

$$A=-\log_{10}(T) \tag{4.8}$$

where A is the absorbance and T is the transmittance. This equation converts transmittance values to absorbance values.

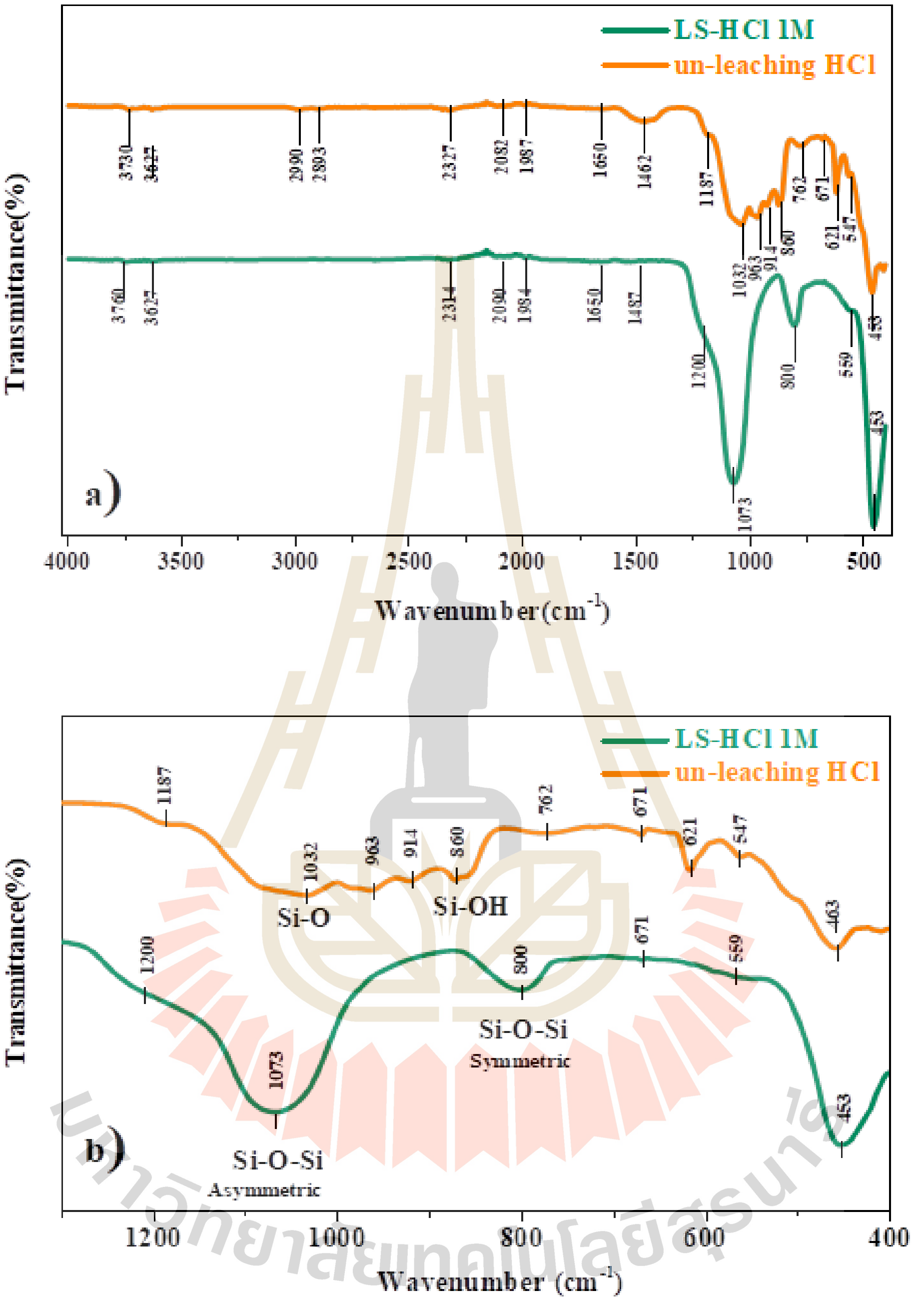

Figure 4.9 FT-IR spectra of SiO_2 nanoparticles between un-leaching HCl and LS-HCl 1M a) FT-IR spectra at 400-4000 cm^{-1} and b) FT-IR spectra at 400-1300 cm^{-1}.

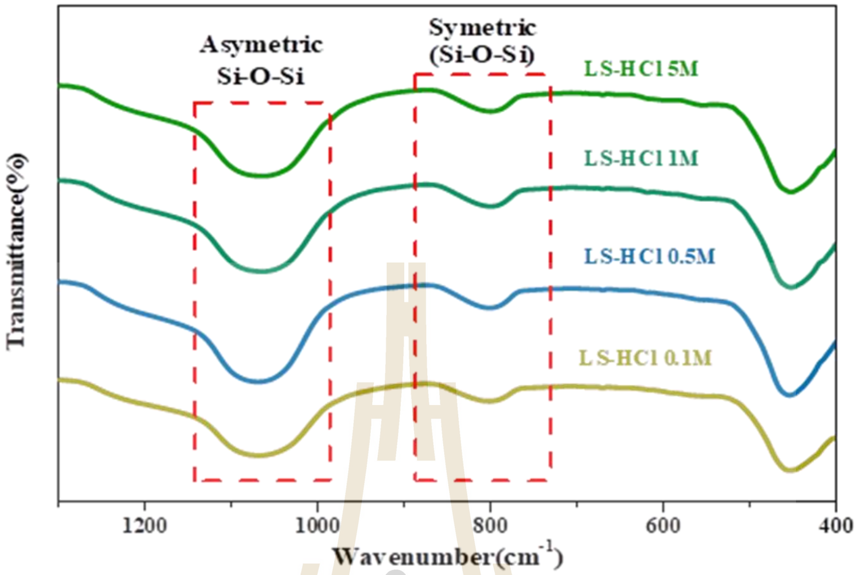

Figure 4.10 FT-IR spectra of LS-HCl 0.1M, LS-HCl 0.5M, LS-HCl 1M, LS-HCl 0.1M, and LS-HCl 5M on the scan range at 400-1300 cm^{-1}.

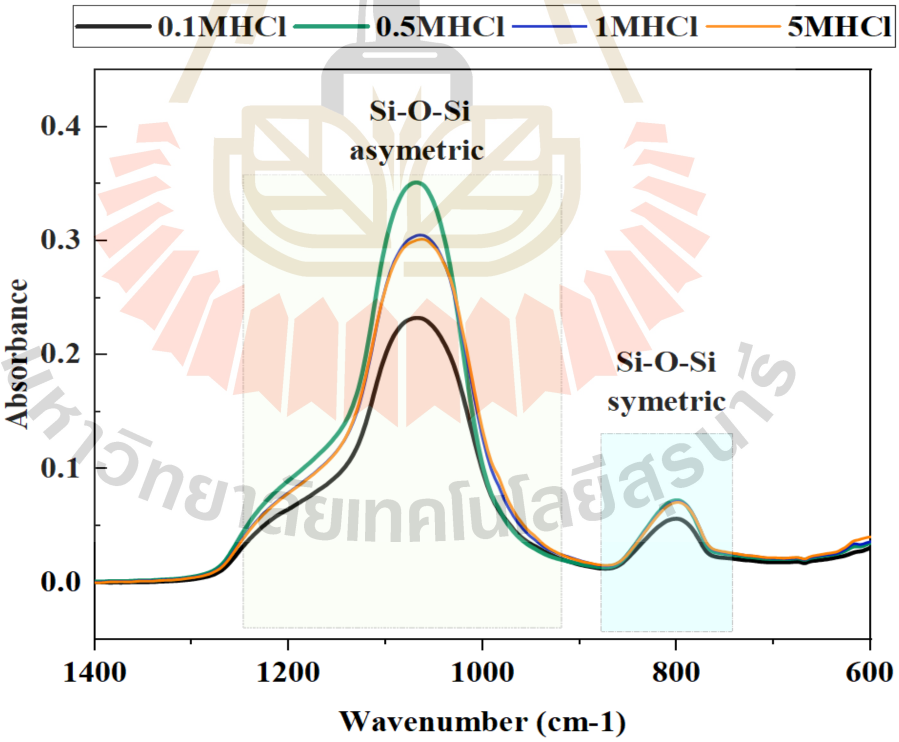

Figure 4.11 Absorbance of FT-IR spectra of LS-HCl 0.1M, LS-HCl 0.5M, LS-HCl 1M, LS-HCl 0.1M, and LS-HCl 5M on the scan range at 600-1400 cm^{-1}.

When comparing the IR intensity between asymmetric and symmetric, it was found that there were differences in intensity. The LS-HCl 0.1M sample has low intensity than LS-HCl (0.5-1) M, as seen in Figure 4.11. In the IR spectrum, changes in intensity depend on the complex structure or defect structure of the sample. As seen in the XRF results in Table 10, LS-HCl 0.1M has a greater number of impurities than the other samples. Therefore, it is possible that the defect of vibration of Si-O-X (X is Mn, K, P, S, and Cl) is more than Si-O-Si on silica peaks of LS-HCl 0.1M. it is result in low intensity at Si-O-Si peaks.

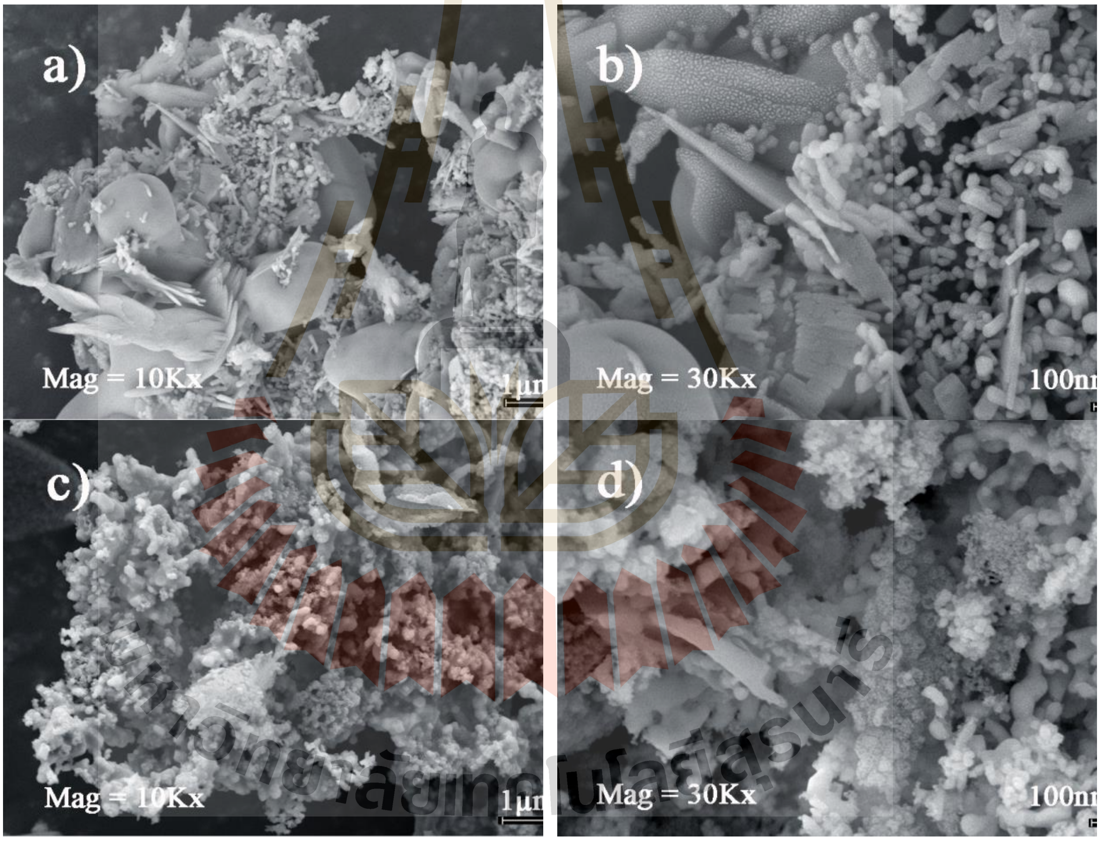

Figure 4.12 FE-SEM image of a) un-leaching HCl 10Kx, b) un-leaching HCl 30Kx, c) LS-HCl0.1M 10Kx, d) LS-HCl 0.1M 30Kx, e) LS-HCl 0.5M 10Kx, f) LS-HCl 0.5M 30Kx, g) LS-HCl 1M 10Kx, h) LS-HCl 1M 30Kx, i) LS-HCl 1M 30Kx, and j) LS-HCl 5M 30Kx.

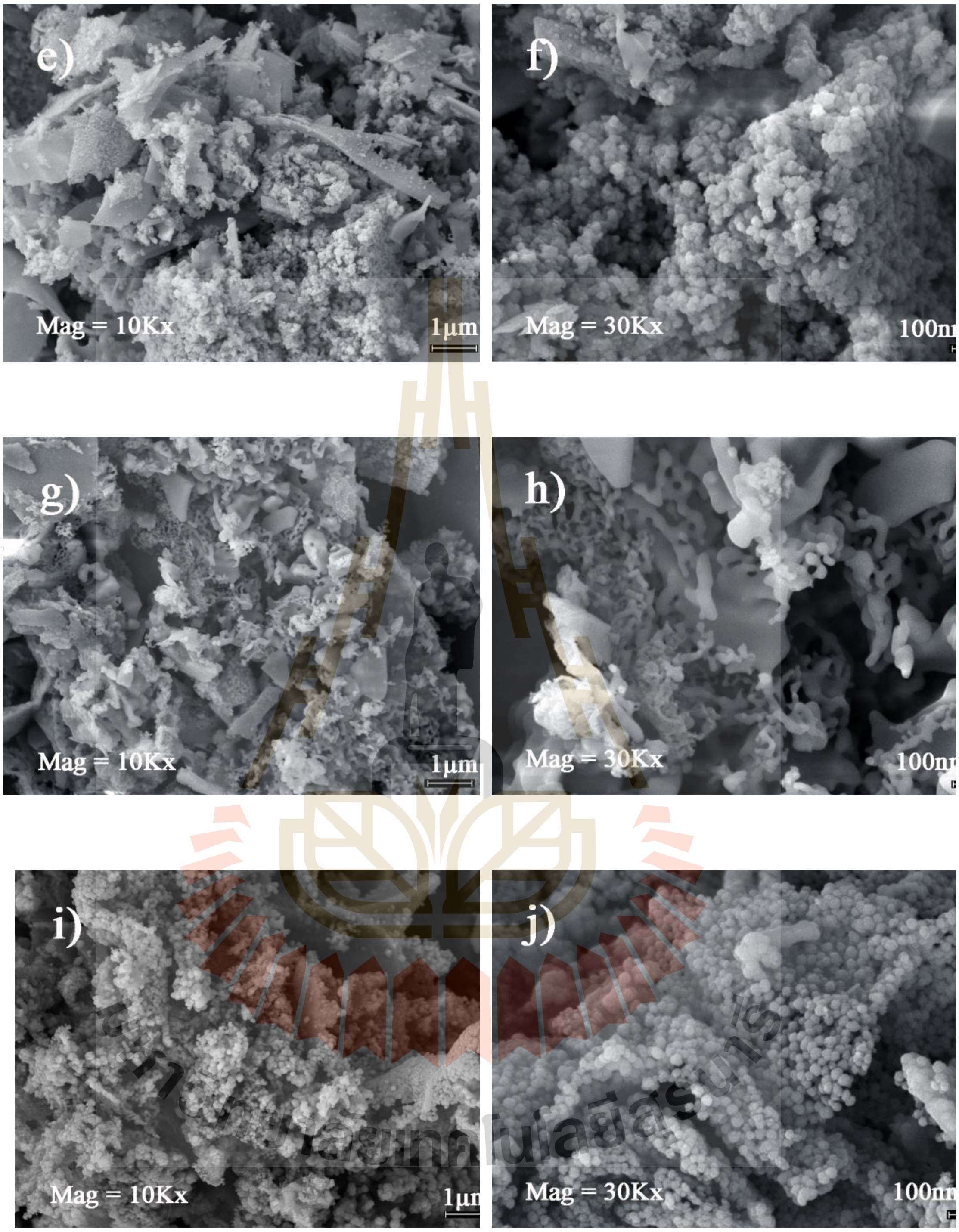

Figure 4.12 FE-SEM image of a) un-leaching HCl 10Kx, b) un-leaching HCl 30Kx, c) LS-HCl0.1M 10Kx, d) LS-HCl 0.1M 30Kx, e) LS-HCl 0.5M 10Kx, f) LS-HCl 0.5M 30Kx, g) LS-HCl 1M 10Kx, h) LS-HCl 1M 30Kx, i) LS-HCl 1M 30Kx, and j) LS-HCl 5M 30Kx (Continued).

Figure 4.12 shows FE-SEM image of SiO_2 nanoparticles prepared at calcination temperature at 700°C. The SEM micrographs use two resolutions for discussing which are 10K and 30K. As shown in Figure 4.12a and Figure 4.12b, the particles of un-leaching HCl reveal the shape to be composed of sphere, rod, plate, and irregular which suggest that particles have many compounds in structure and confirm XRD results. However, we can be seen that the normal form of SiO_2 nanoparticles was produced after treated with HCl, which is found that the SiO_2 particles is in sphere and irregular form with poor agglomerate at low concentration of HCl, as shown in Figure 4.12c-4.12h. Besides, when treated at 5M of HCl concentration, the form of SiO_2 nanoparticles is in only sphere-like and the particle size is less than 100 nm, as revealed in Figure 4.12i and 4.12j.

Thereby, the FE-SEM images is another common way to confirm that the effect of HCl acid helps to reduce an impurity and change the impure SiO_2 structure into the pure SiO_2 structure. The elemental composition of the SiO_2 nanoparticles on the surface of AGL ash was verified by EDS detection as shown in Figure 4.13. Before leaching with HCl, the spectra of samples detect many elements (K, Ca, Cl, Na, Mg, S) and small peak of Si and O, as revealed in Figure 4.13a.

However, the Mg and Na was found in EDS spectra but these elements are not detected by XRF, which may be due to scope of scan difference. After leaching with HCl, the EDS spectra found that Si and O are increased and other elements decrease the intensity (Figure 4.13b-4.13e), indicating that the high purity of SiO_2 was obtained after HCl treated. Likewise, mapping images confirms that Si and O are good dispersion on surface of particles after HCl leaching, as can be seen in Figure 4.14a-4.14o. Thereby, EDS results confirms XRD and XRF results as described above.

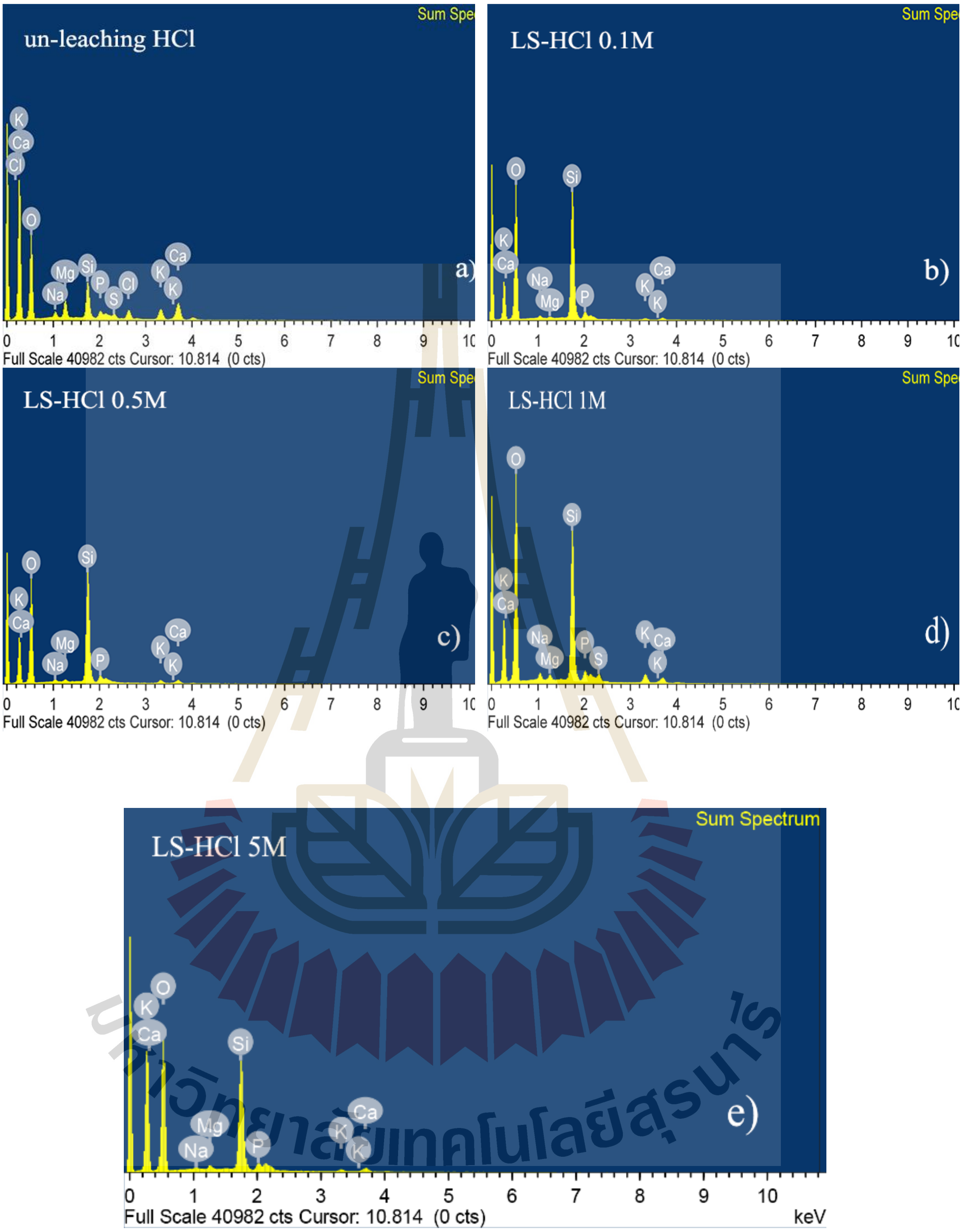

Figure 4.13 EDXS image of a) un-leaching HCl, b) LS-HCl 0.1M, c) LS-HCl 0.5M, d) LS-HCl 1M, and LS-HCl 5M.

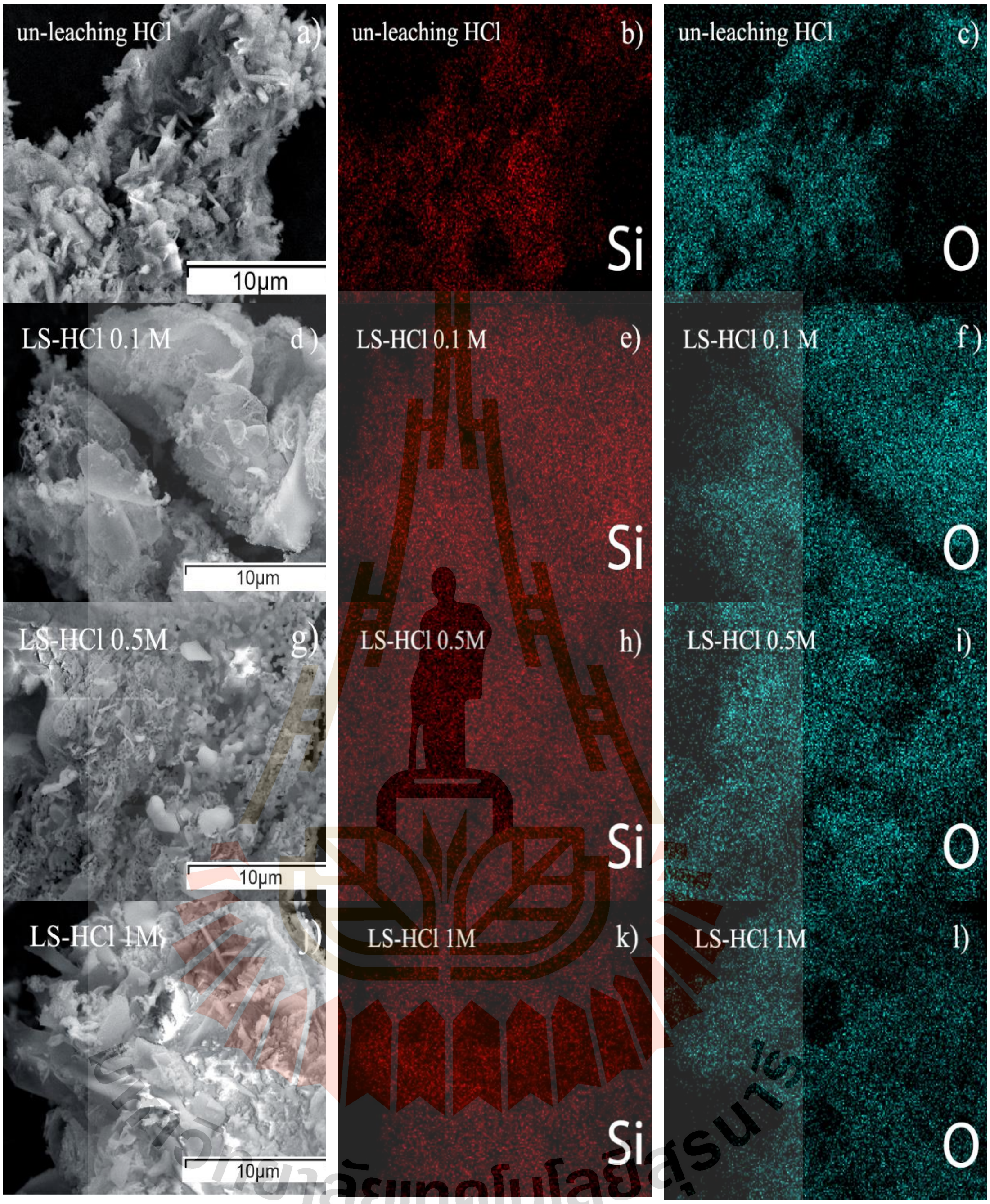

Figure 4.14 Elemental mapping image of a) un-leaching HCl, b) Si in un-leaching HCl, c) O in un-leaching HCl, d) LS-HCl 0.1M, e) Si in LS-HCl 0.1M, f) O in LS-HCl 0.1M, d) LS-HCl 0.1M, e) Si in LS-HCl 0.1M, f) O in LS-HCl 0.1M, g) LS-HCl 0.5M, h) Si in LS-HCl 0.5M, i) O in LS-HCl 0.5M, j) LS-HCl 1M, k) Si in LS-HCl 1M, l) O in LS-HCl 1M, m) LS-HCl 5M, n) Si in LS-HCl 5M, and o) O in LS-HCl 5M.

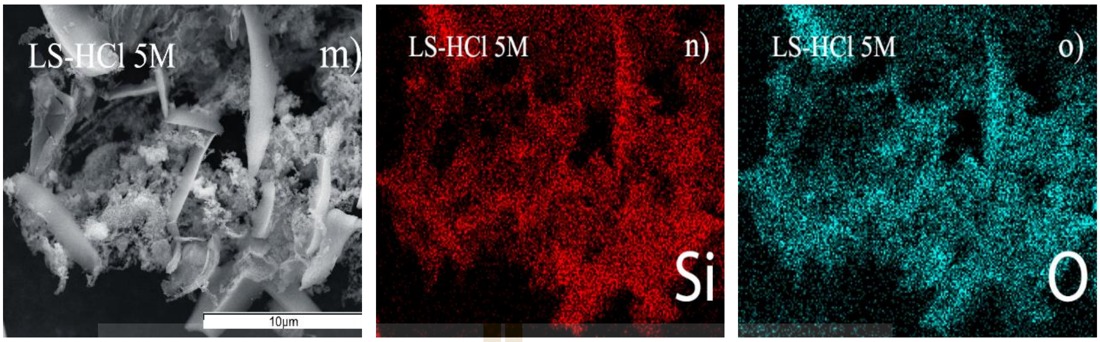

Figure 4.14 Elemental mapping image of a) un-leaching HCl, b) Si in un-leaching HCl, c) O in un-leaching HCl, d) LS-HCl 0.1M, e) Si in LS-HCl 0.1M, f) O in LS-HCl 0.1M, d) LS-HCl 0.1M, e) Si in LS-HCl 0.1M, f) O in LS-HCl 0.1M, g) LS-HCl 0.5M, h) Si in LS-HCl 0.5M, i) O in LS-HCl 0.5M, j) LS-HCl 1M, k) Si in LS-HCl 1M, l) O in LS-HCl 1M, m) LS-HCl 5M, n) Si in LS-HCl 5M, and o) O in LS-HCl 5M (Continued).

The nanostructure and amorphous nature of pure SiO_2 were confirmed with TEM image and selected area electron diffraction. TEM image is shown in part a-e of Figure , It can see that the nanostructure of un-leaching samples has variety of the shape and found crystal structure from SAED, which confirm XRD, ED-XRF, FE-SEM, and EDS spectra that the ash has more metal oxide elements as shown in Figure 4.14.

Moreover, part b-e of Figure 4.15 shows the shape of pure SiO_2, which revealed sphere-like particles of SiO_2, and the SiO_2 size is smaller than 100 nm after leaching with HCl acid. However, electron diffraction remains slightly in LS-HCl samples, as revealed in the SAED image. Little electron diffract was consistent with the XRF results, as described above. Because in LS-HCl samples, components other than SiO_2 are still present. The other components of element oxide able to show in green box square, as depicted in Figure 4.15a-4.15e.

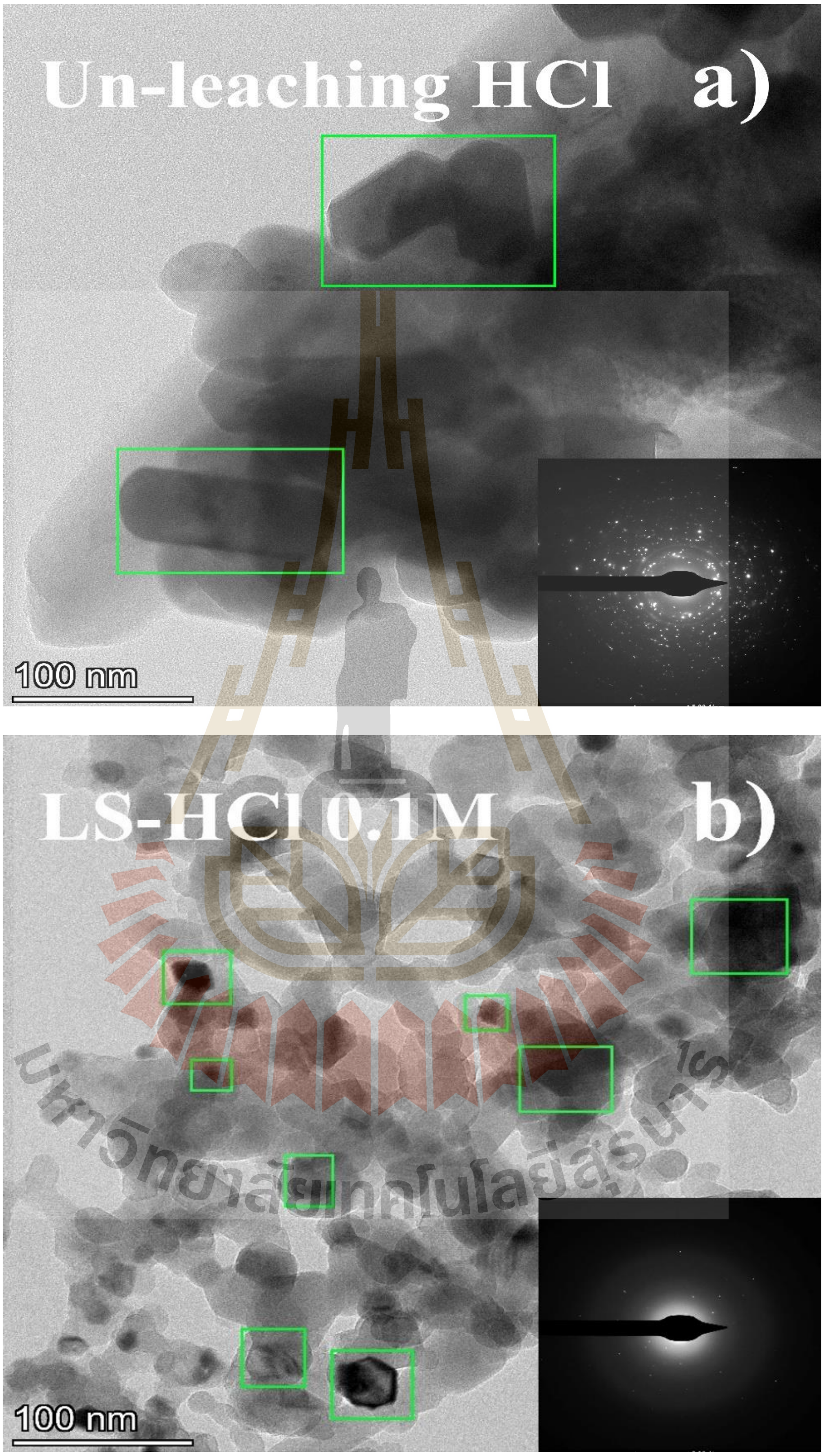

Figure 4.15 TEM image of SiO_2 nanoparticles a) LS-HCl 0.1M, b) LS-HCl 0.5M, c) LS-HCl 1M, d) LS-HCl 0.1M, and e) LS-HCl 5M.

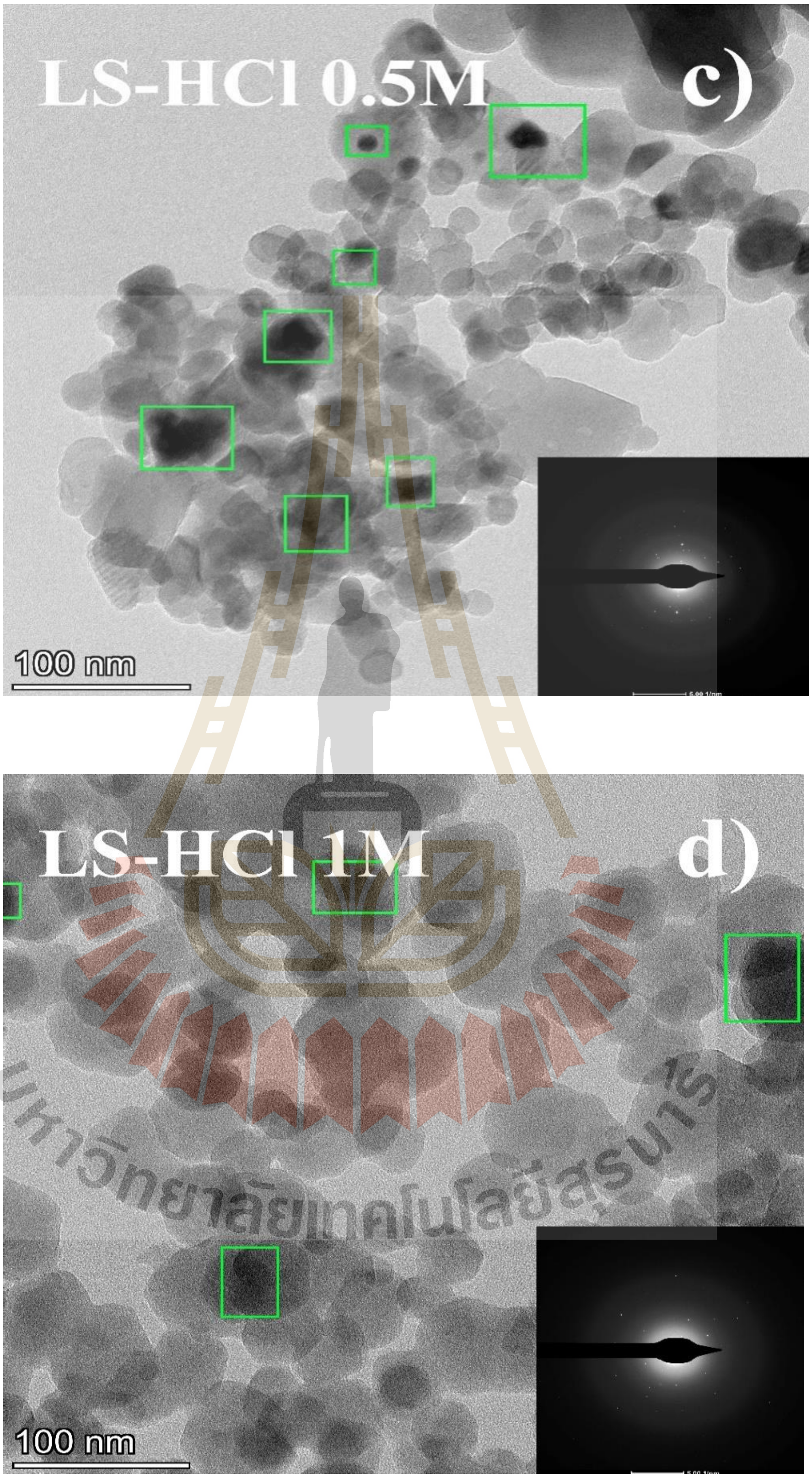

Figure 4.15 TEM image of SiO_2 nanoparticles a) LS-HCl 0.1M, b) LS-HCl 0.5M, c) LS-HCl 1M, d) LS-HCl 0.1M, and e) LS-HCl 5M (Continued).

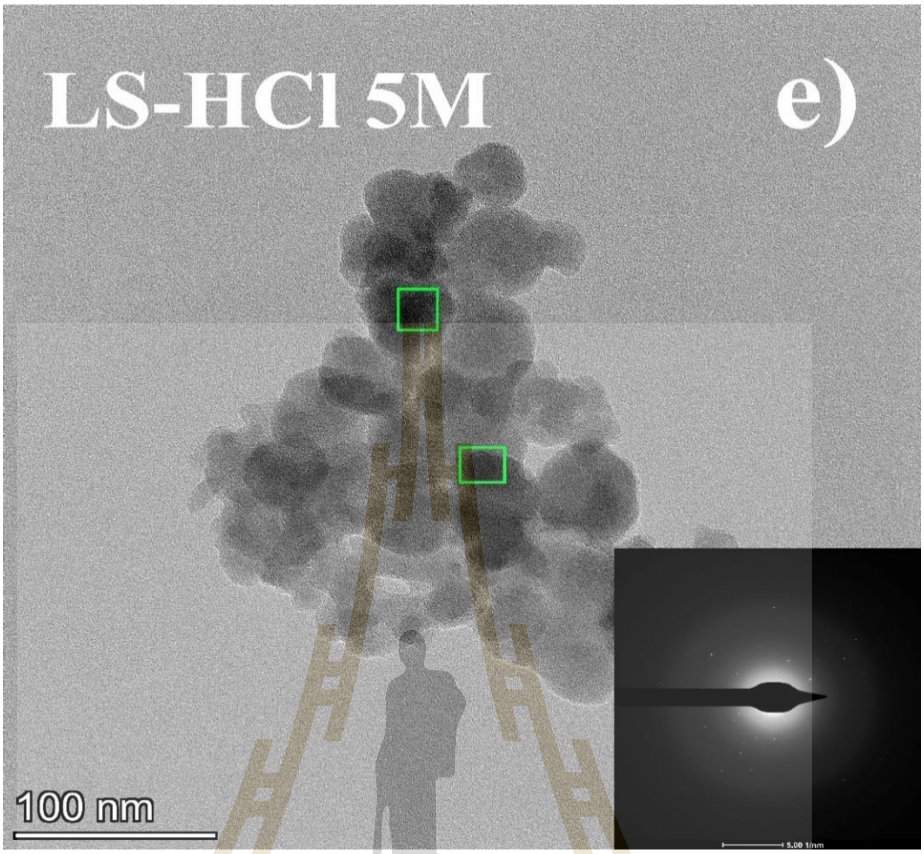

Figure 4.15 TEM image of SiO_2 nanoparticles a) LS-HCl 0.1M, b) LS-HCl 0.5M, c) LS-HCl 1M, d) LS-HCl 0.1M, and e) LS-HCl 5M (Continued).

The structural properties of SiO_2 nanoparticles at the atomic level were studied through the spectrum of absorption energy at the Si K-edge level. X-ray absorption revealed the characteristic of a tetrahedral SiO_2 cluster. The spectra disclosed information on energy absorption through two peaks. In 1994, Dien Li et al. reported the behavior of these two peaks, which describes the electron configuration state. The first peak, located at pre-edges, illustrates the transition of Si 1s to the Si 3s state, representing a dipole-forbidden transition zone. The second peak, situated at the rising edge zone, demonstrates the transition of an electron from the Si 1s state to the Si 3p state, which occurs in a dipole-allowed transition zone. Comparisons were made between the spectra of the samples and SiO_2 from the industries.

The spectral pattern of the HCl-etched sample closely resembles that of pure SiO_2 from industrial sources, as illustrated in Figure 4.16. The X-ray absorption near-edge structure (XANE) spectrum of the HCl-etched sample and 99.8% SiO_2 exhibits a weak intensity at the first peak in the Si K-edge XANE, attributed to the dipole-forbidden transition of Si 1s to a 3s-like state. Conversely, the second peak of the spectrum at the rising edge displays a very strong intensity due to the dipole-allowed transition of Si 1s to 3s. The second peaks of the HCl-etched sample and 99.8% SiO_2 are at 1847.5 and 1847.6 eV, respectively, as indicated in Figure 4.17b and Figure 4.17c. The positions of the spectra for the coupled samples are not distinct, indicating that the oxidation state of Si in the HCl-etched samples remains at 4+. However, in the unleached sample, the peak slightly shifts towards the left-hand side, possibly due to interference from neighboring atoms that are not Si. The energy absorption at the rising edge for the unleached sample is measured at 1846.4 eV (as seen in Figure 4.17a).

Furthermore, the absorption energy of HCl-etched samples exhibits variations in intensity, as observed in Figure 4.18, This difference in intensity can be attributed to variations in sample thickness during measurement. Variances in sample thickness affect the absorption energy as electrons from the beam interact differently within the samples. The difference of the thickness of samples will do the absorption energy after electron from beam interact electron in samples is difference. The position of rising edge of samples are slight shift of spectrum of absorption energy in gradient energy ± 0.2 eV as fitting data (see in Figure 4.19).

In 2021, Wataru Katayama et al. conducted a study on the first-principles XANES simulation for oxygen-related defects in Si-O amorphous material. They discovered that defects in oxygen within SiO_2 result in a peak shift in the spectrum. Therefore, the shift in the position of the rising edge of the samples may be attributed to the crystal field effect. This effect refers to variations in the local symmetry around the absorbing atom, which can influence the shift in edges observed in spectra.

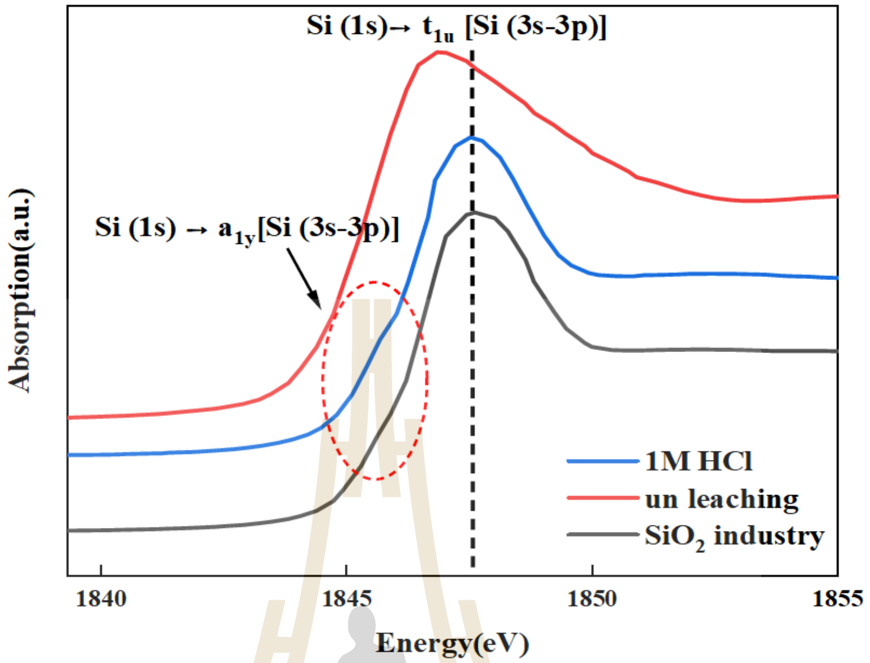

Figure 4.16 The absorption energy spectrum of un-leaching, LS-HCl 1M, and 99.8SiO_2 at 1835-1855 eV.

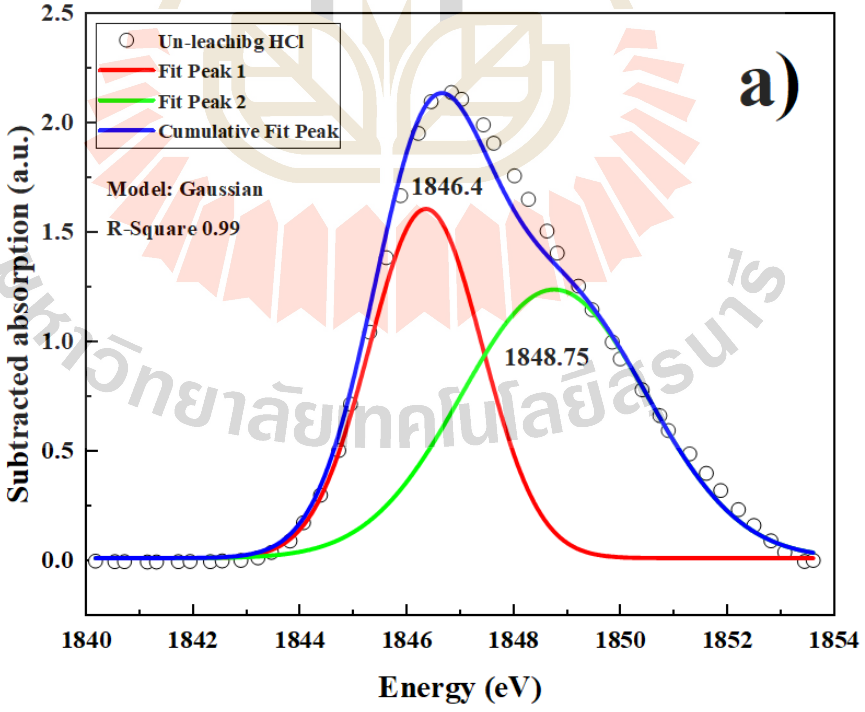

Figure 4.17 The fitting of absorption energy spectrum of a) un-leaching, b) LS-HCl 1M, and c) 99.8%SiO_2 at 1835-1855 eV.

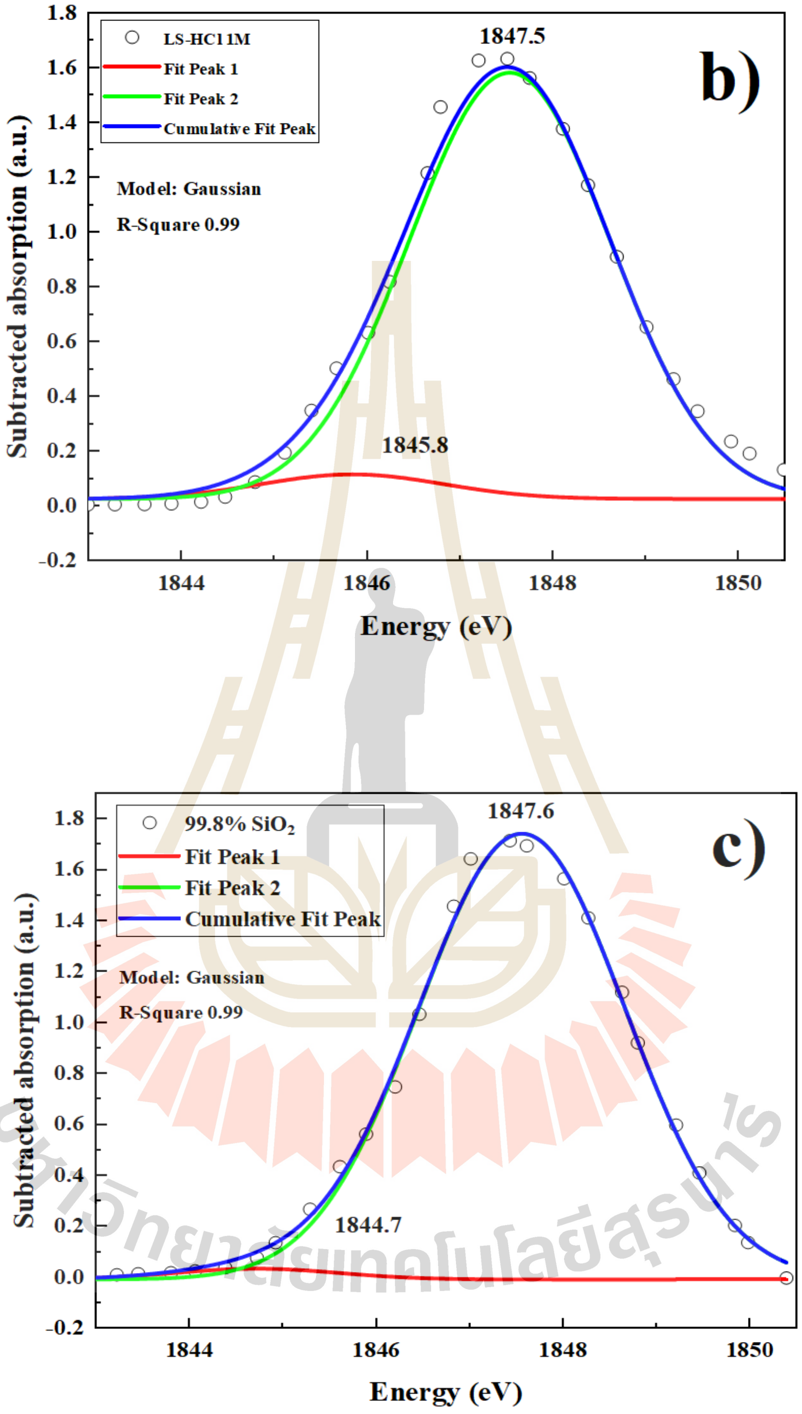

Figure 4.17 The fitting of absorption energy spectrum of a) un-leaching, b) LS-HCl 1M, and c) 99.8%SiO_2 at 1835-1855 eV. (Continued).

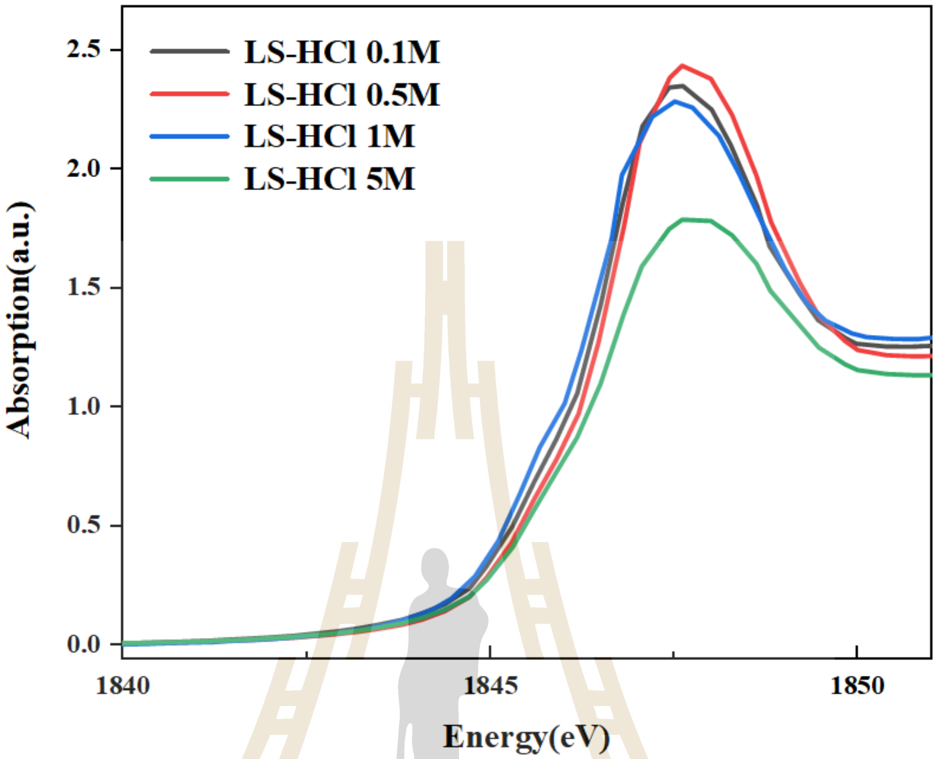

Figure 4.18 XANES spectrum of LS-HCl 0.1M, LS-HCl 0.5M, LS-HCl 1M, and LS-HCl 5M.

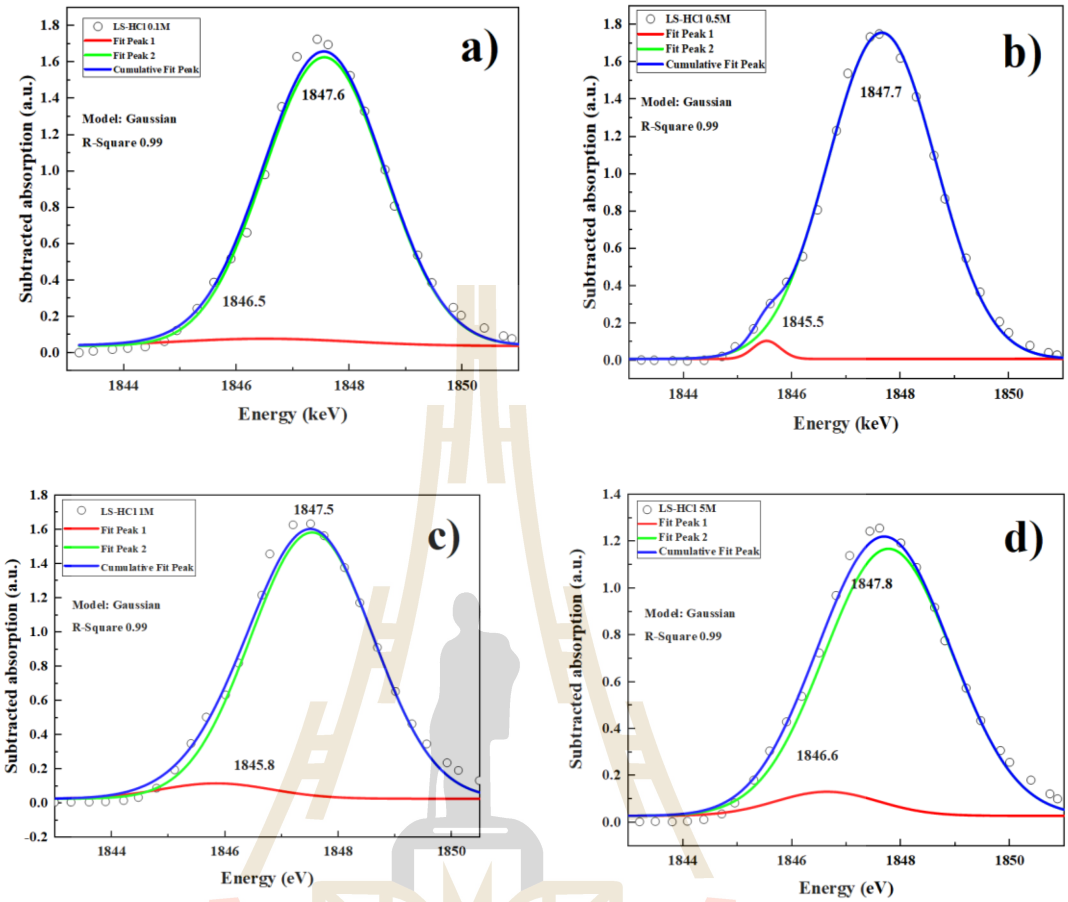

Figure 4.19 The fitting of absorption energy spectrum of LS-HCl 0.1M, LS-HCl 0.5M, LS-HCl 1M, and LS-HCl 5M.

Table 4.3 The peaks position of pre-edge (peak1) and rising-edge (peak2) of LS-HCl 0.1M, LS-HCl 0.5M, LS-HCl 1M, and LS-HCl 5M.

Position of absorption energy	Samples			
	LS-HCl 0.1M	LS-HCl 0.5M	LS-HCl 1M	LS-HCl 5M
Peak1	1846.5	1845.5	1845.8	1846.6
Peak2	1847.6	1847.7	1847.5	1847.8

4.4 Summary of the first methodology

Experiments of 1st HCl etching of our SiO_2 samples were performed to the synthesis of SiO_2. The concluding in this 1st methodology was summarized below:

TGA/DSC results:For study of the effect of thermal on sample, we found that water and moisture rapid evaporation in temperature range 30-200°C, hemicellulose, cellulose, nitrogen and hydrocarbon decompose over at 210-365°C. Moreover, in high temperature, thermal decompose at 635°C which is related to the cleavage of the C-C bond. In un-acid etching sample, the residual mass after calcination at 950°C is 50.8%. For acid etching samples, the residual mass is in range 23-32%.

XRD results: The crystallinity of un-none pattern found in un-acid etching sample that the pattern able to classified into 3 main patterns: potassium chloride (KCl), calcium manganese carbonate ($CaMn_2CO_6$), and SiO_2 (quartz). However, after etching samples with HCl, the samples exhibit amorphous pattern of SiO_2, which have no pattern of KCl and $CaMn_2CO_6$. Moreover, when increase HCl concentration for etching samples, the quartz and cristobalite appear in structure.

XRF results: The mass fraction from XRF measurement confirms the results from the XRD, which found that the un-acid etching sample have high percentage of mass that it has 3 elements: Ca, K, and Si in which percentage of mass is 13.31%(CaO), 8.84%(K_2O), and 53.18%(SiO_2). After HCl etching, Ca and K reduced in structure, which percentage of the mass in structure less than 2%. And we found that SiO_2 mass have higher than 93%.

FT-IR results: In samples, after calcination at 700°C for 3h, the samples have small peaks at 3627-3730 and 3760 cm^{-1} represent the free O-H group, C-H stretching and C-H bending of SiO_2 nanoparticles were corresponding to the peaks at 2800-3000 cm^{-1} and 1462 cm^{-1}. Wavenumber at 1090-1030 and 800 cm^{-1}, were corresponding of asymmetric stretching Si-O-Si and symmetric stretching Si-O-Si vibration, respectively. However, from FT-IR results, it is clear that HCl etching samples have strong Si-O-Si vibration of asymmetric and symmetric stretching more than un-acid etching sample, which confirm that the purity of HCl etching samples more than un-acid etching sample.

FE-SEM, EDS/mapping, TEM results: Morphology of SiO_2 nanoparticles is in the irregular shape after material etching with low concentration of HCl. After using high HCl concentration, lead to a spherical shape of particles, the size of SiO_2 nanoparticle less than 100 nm. The EDS spectra found that Si and O are increased and other elements decrease the intensity, indicating that the high purity of SiO_2 was obtained after HCl treated. Likewise, mapping images confirms that Si and O are good dispersion on surface of particles. TEM images show the irregular and sphere particles at low and high concentration of HCl, likewise FE-SEM results, as described above. Furthermore, selected area (electron) diffraction image, these images confirm non-crystalline structure of powders, which image exhibited in the form of amorphous.

XAS results: In results of XANES analysis, SiO_2 is slight shift of pre-edge and rising, which the position of edge is in range 1845.5-1846.5 kV (pre-edge) and 1847.6-1847.8 EV (rising -edge). So, the oxidation number of silicon in the experimental sample is the same as that in the factory sample.

CHAPTER V

RESULTS AND DISCUSSION (PART II): EFFECT OF HYDROCHLORIC AND NITRIC ON PURE SiO_2 NANOPARTICLE DERIVED FROM SILICON DIOXIDE ASH

To improve purity of SiO_2 from 96% to 99%, reflux process used for 2nd acid etching. In this experiment, the process classified into 2 subsections: 2nd HCl etching and 2nd acid etching. After experiment, the pure SiO_2 powder was characterized by XRF and XAS. Additionally, the morphology transformation of pure SiO_2 exhibits by FE-SEM and the growth mechanism of SiO_2 studied by TEM. For models of SiO_2 growth illustrated in diagram and simple models of Si-O bond by using an opensource program (Sketch Chemistry)

5.1 The production of pure SiO_2 nanoparticles via hydrochloric acid etching

In this experiment, after using reflux for 2nd HCl etching at 0.1-5M and calcination at 700°C for 3h, for study of SiO_2 structure divided into 4 samples: 0.1MDHCl, 0.5MDHCl, 1MDHCl, and 5MDHCl, as illustrated in Figure 5.1. SiO_2 purity after 2nd HCl etching, mass fraction of SiO_2 is about 99.7-99.8%, which increase 3% from SiO_2 ash sample. The element oxide in samples able to show in Table 5.1. For purity of SiO_2 increases due to the mass of alkaline and alkaline earth is reduced with HCl etching, which is in solution of solution form after reflux. Typically, we know that HCl acid is non interact with SiO_2. Because of SiO_2 is covalent compound, has high strong covalent bond, and strong crystalline structure. The acid reaction on Si-O bonds make it difficult for HCl to break the SiO_2 covalent compound.

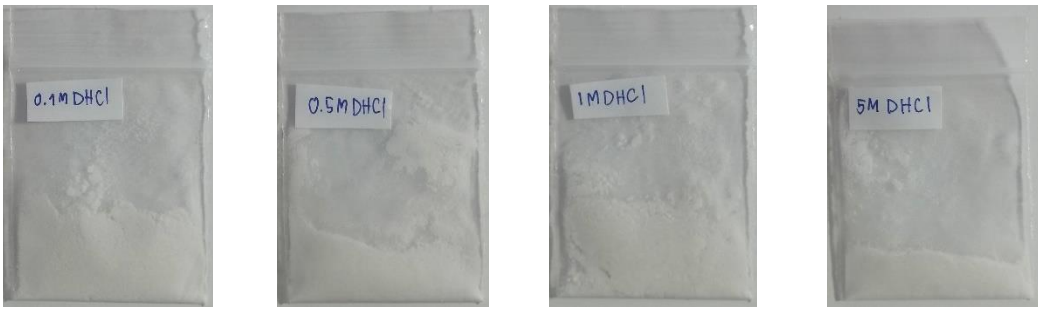

(a) (b) (c) (d)

Figure 5.1 White powders of SiO_2 of 0.1MDHCl, 0.5MDHCl, 1MDHCl, and 5MDHCl.

Table 5.1 The XRF results of 0.1MDHCl, 0.5MDHCl, 1M DHCl, and 5MDHCl

Samples	Mass fraction of the element and element oxide (%)							
	SiO_2	K_2O	CaO	P_2O_5	Fe_2O_3	MnO_2	SO_3	Cl
0.1M DHCl	99.80	0.08	0.04	0.00	0.01	0.02	0.02	-
0.5M DHCl	99.80	0.07	0.04	0.00	0.01	0.02	0.03	-
1M DHCl	99.75	0.07	0.07	0.00	0.03	0.03	0.02	-
5M DHCl	99.77	0.07	0.04	0.00	0.02	0.03	0.02	-

Hence, the SiO_2 does not change into solution form and does not react with HCl under normal conditions. However, without SiO_2, all element oxide was removed by filtration. The reaction of HCl etching able to follow in Equation (4.7).

$$XSiO_{2(s)}(ash) + H_2O(aq) + 2HCl(aq) \rightarrow SiO_{2(s)}(colloidal) + XCl(aq) + 2H_2O(aq) \quad (4.7)$$

Where X is alkaline and alkaline earth

For morphology size of SiO_2 increases more than 100nm due to acid and effect of thermal expansion, as illustrated in Figure 5.2a-5.2d. Moreover, the shape of SiO_2 in DHCl samples is in a sphere, likewise several reported sphere shapes of particles is one of pure SiO_2 (Cui, Liang et al., 2016, Kim, Park et al., 2021, Prabha, Durgalakshmi et al., 2021). In this experiment, when the concentration of HCl increases, the size distribution of SiO_2 nanoparticles is increases, which average size of particles revealed in Figure 5.3.

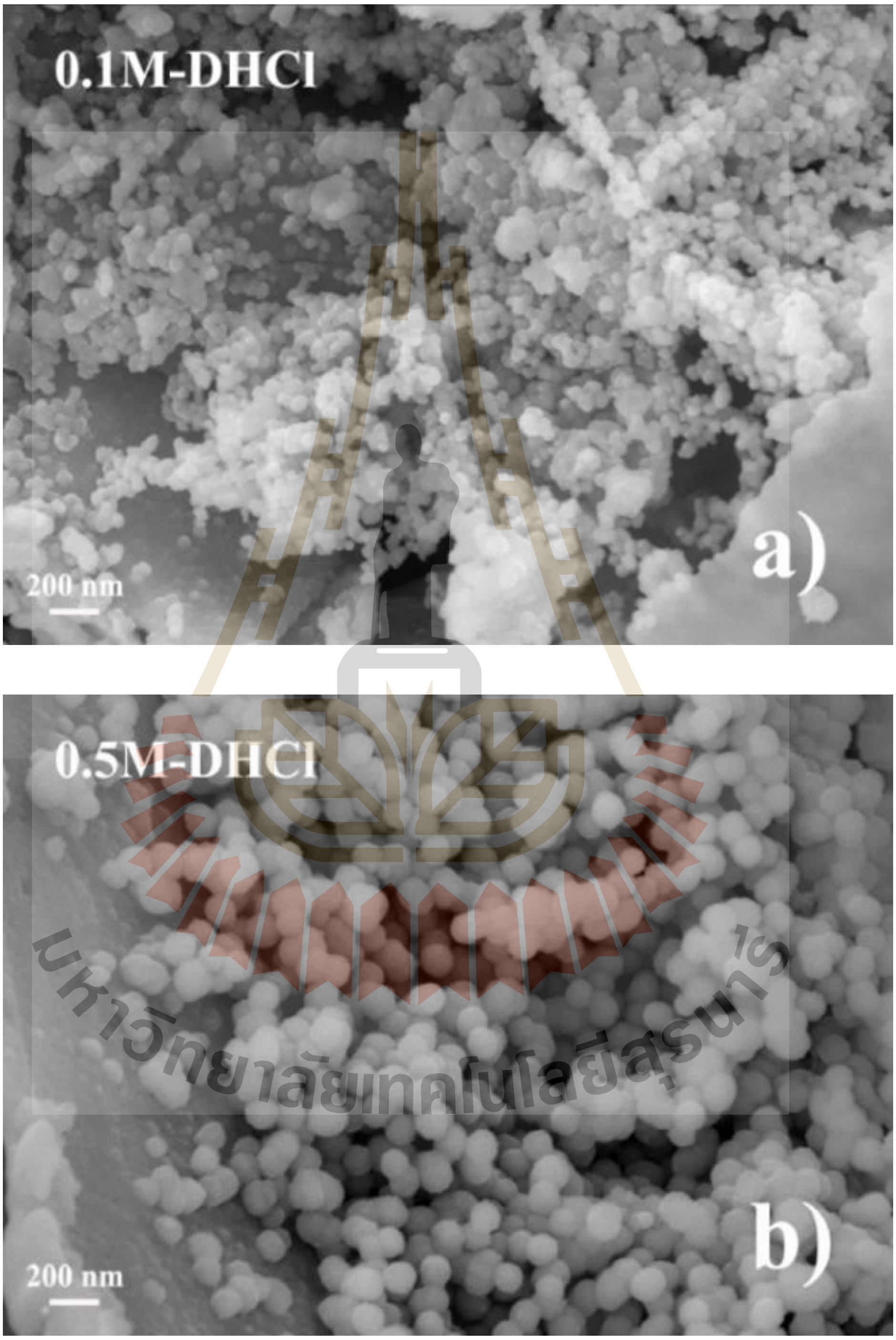

Figure 5.2 FE-SEM images of a) 0.1MDHCl, b) 0.5MDHCl, c) 1MDHCl, and d) 5MDHCl.

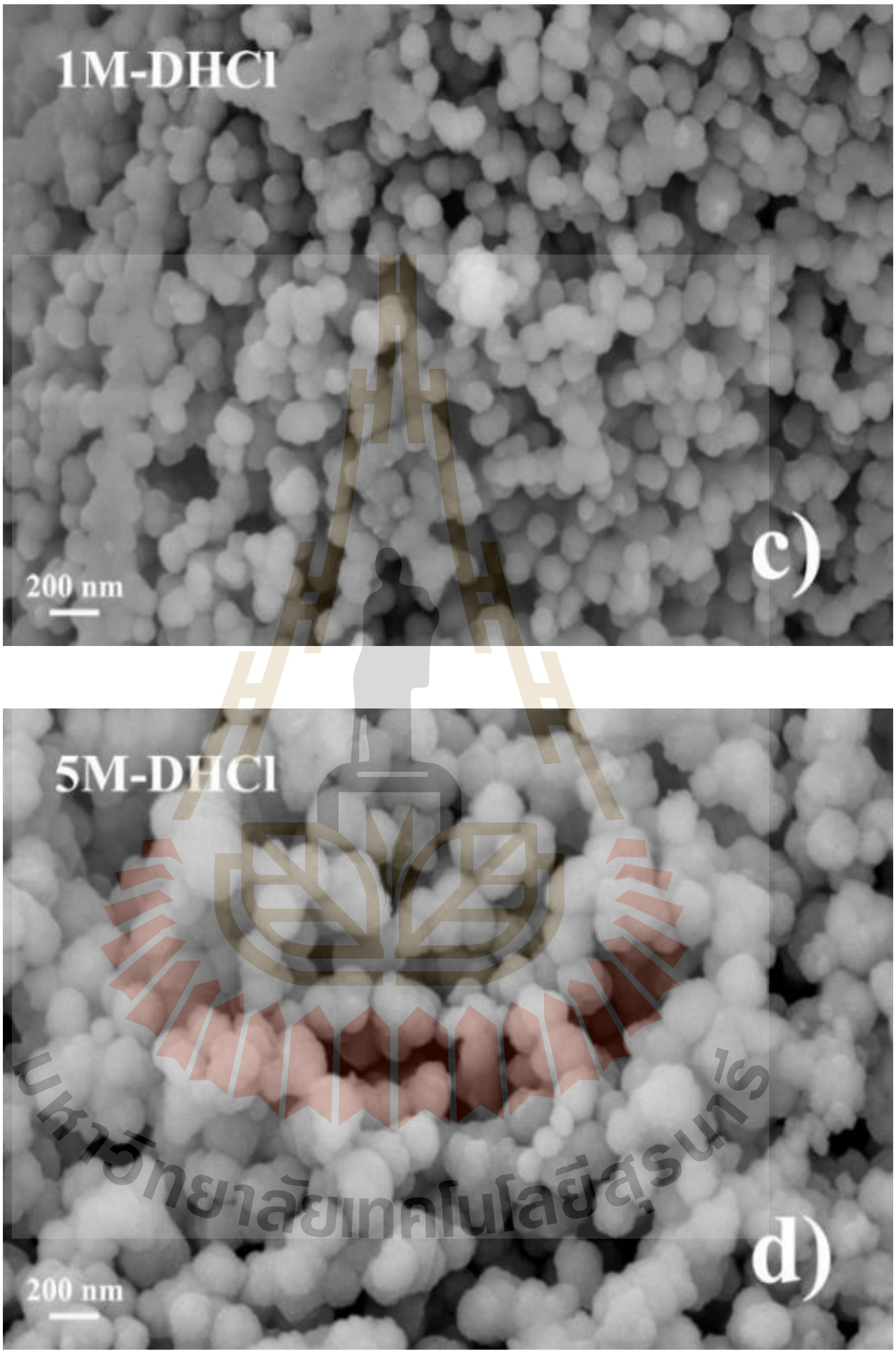

Figure 5.2 FE-SEM images of a) 0.1MDHCl, b) 0.5MDHCl, c) 1MDHCl, and d) 5MDHCl (Continued).

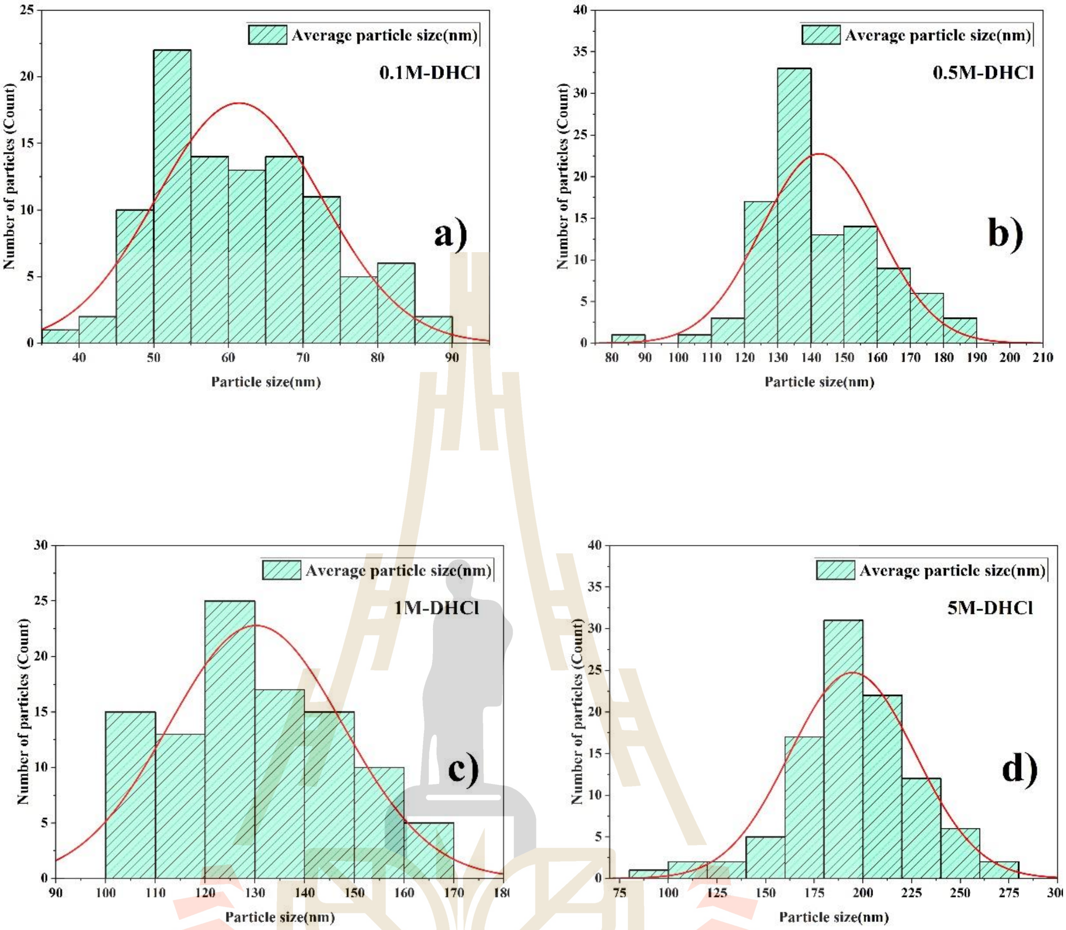

Figure 5.3 Average particle size of a) 0.1MDHCl, b) 0.5MDHCl, c) 1MDHCl, and d) 5MDHCl.

The average size of particles in this process is 50-60 nm (at 0.1M of HCl), 130-150 nm (at 0.5-1M of HCl), and the big size exhibited in 5M-DHCl sample, SiO_2 size is around 200 nm. Furthermore, the TEM image in Figure 5.4 shows the insight of SiO_2 nanoparticles of 0.1MDHCl (see in Figure 5.4a), 0.5MDHCl (see in Figure 5.4c), 1MDHCl (as observed in Figure 5.4e), and 5MDHCl (as seen in Figure 5.4g). From TEM images of samples, which found the reason for the average size of particles increases that the increase of particles depends on the agglomeration of small particles of SiO_2 after calcination. Likewise, the number of small particles of SiO_2 for agglomeration, it may be depended on the ability of HCl on SiO_2, which found the number of particles of sample at using high concentration of HCl, it will more than low the concentration, as depicted in TEM image of 5MDHCl sample.

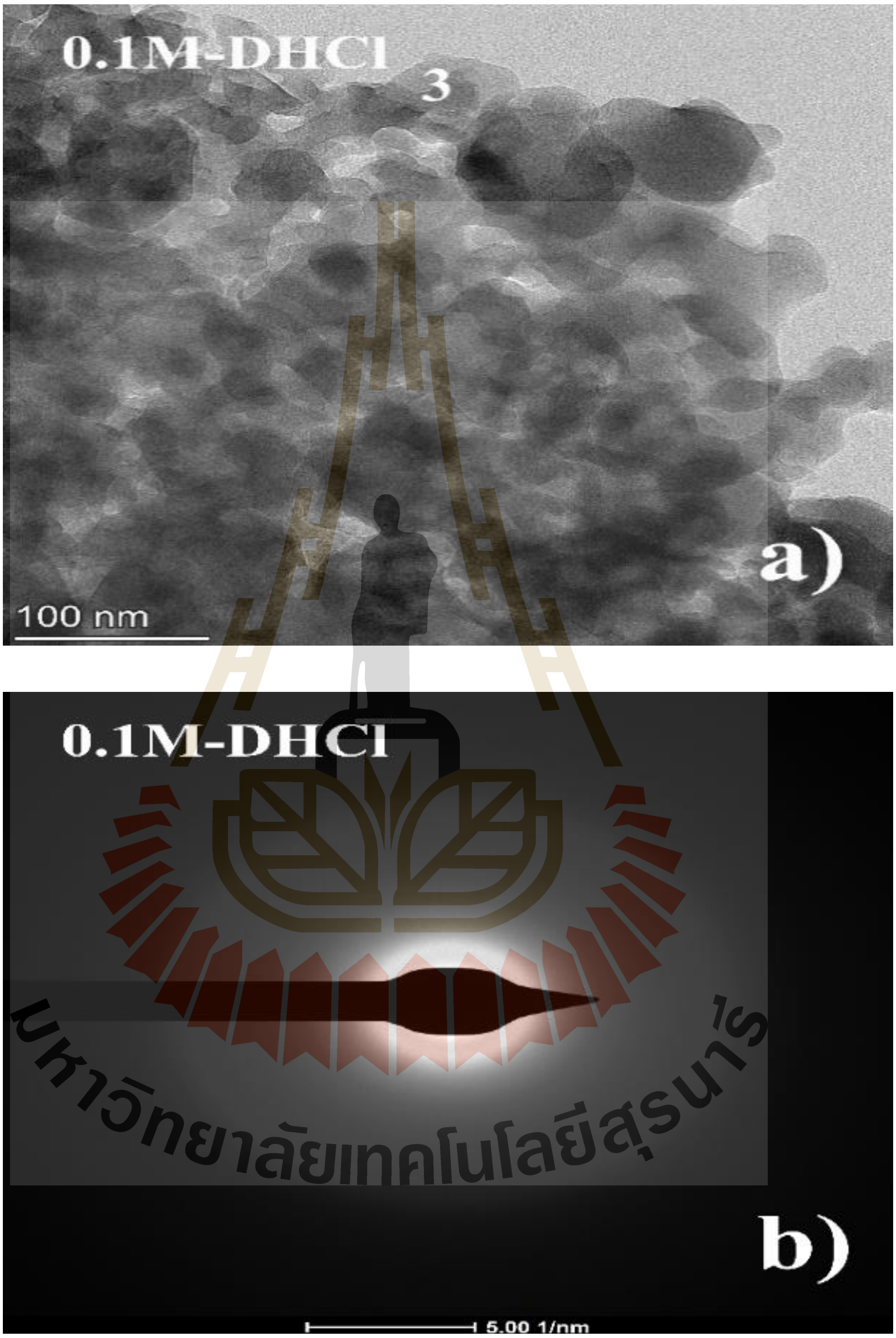

Figure 5.4 TEM and SEAD images of 0.1MDHCl (a, b), 0.5MDHCl (c, d), 1MDHCl (e, f), and 5MDHC (g, h).

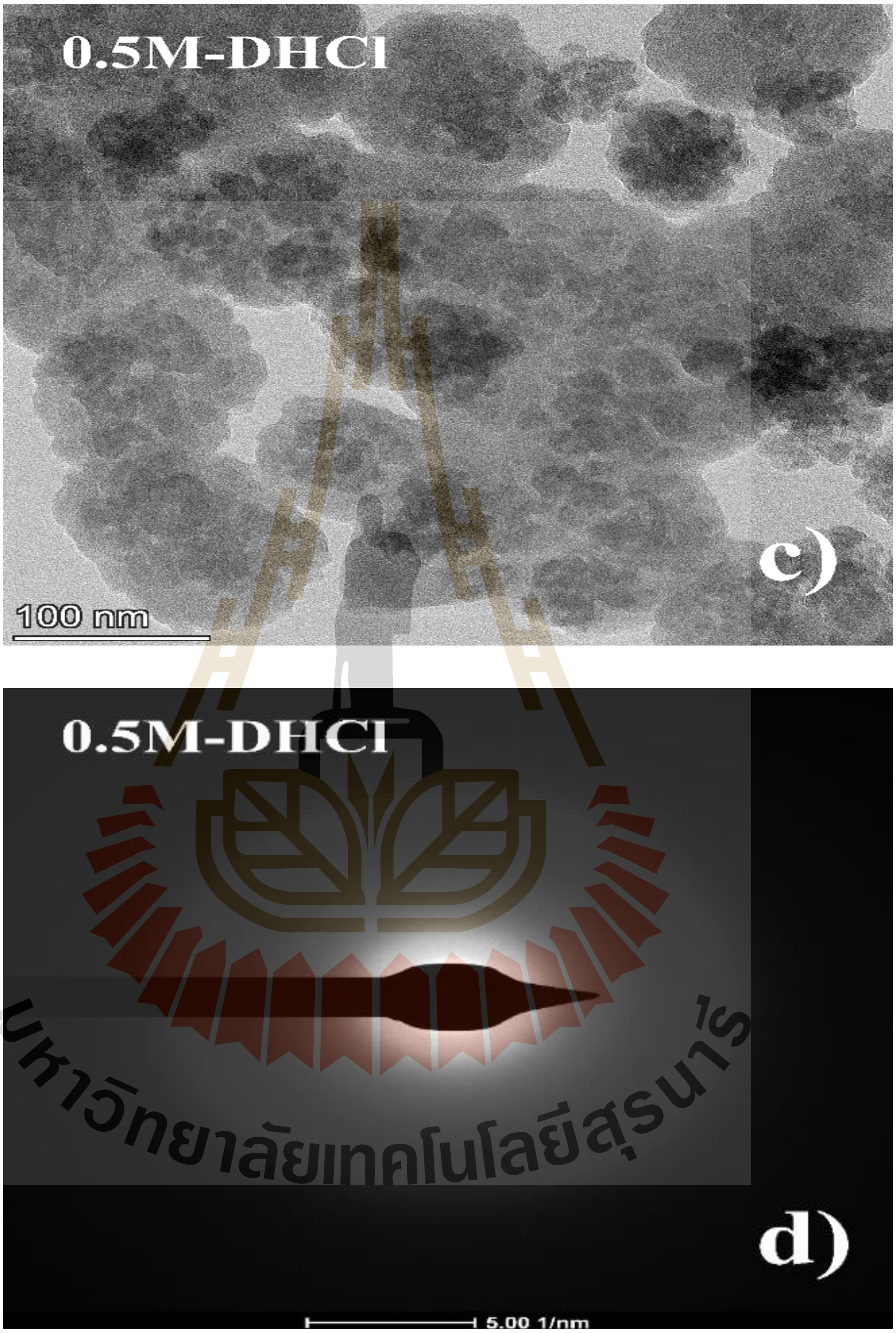

Figure 5.4 TEM and SEAD images of 0.1MDHCl (a, b), 0.5MDHCl (c, d), 1MDHCl (e, f), and 5MDHC (g, h) (Continued).

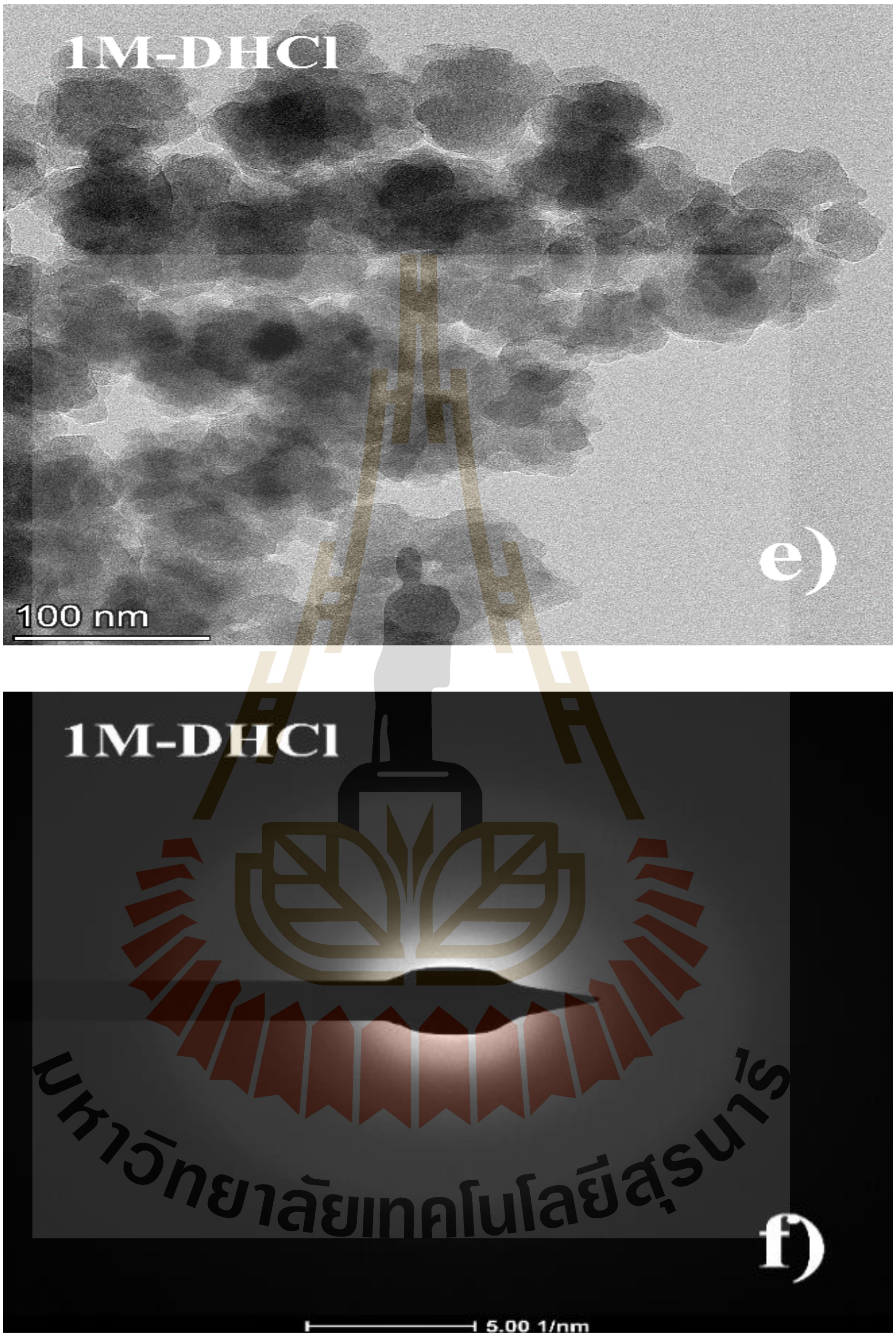

Figure 5.4 TEM and SEAD images of 0.1MDHCl (a, b), 0.5MDHCl (c, d), 1MDHCl (e, f), and 5MDHC (g, h) (Continued).

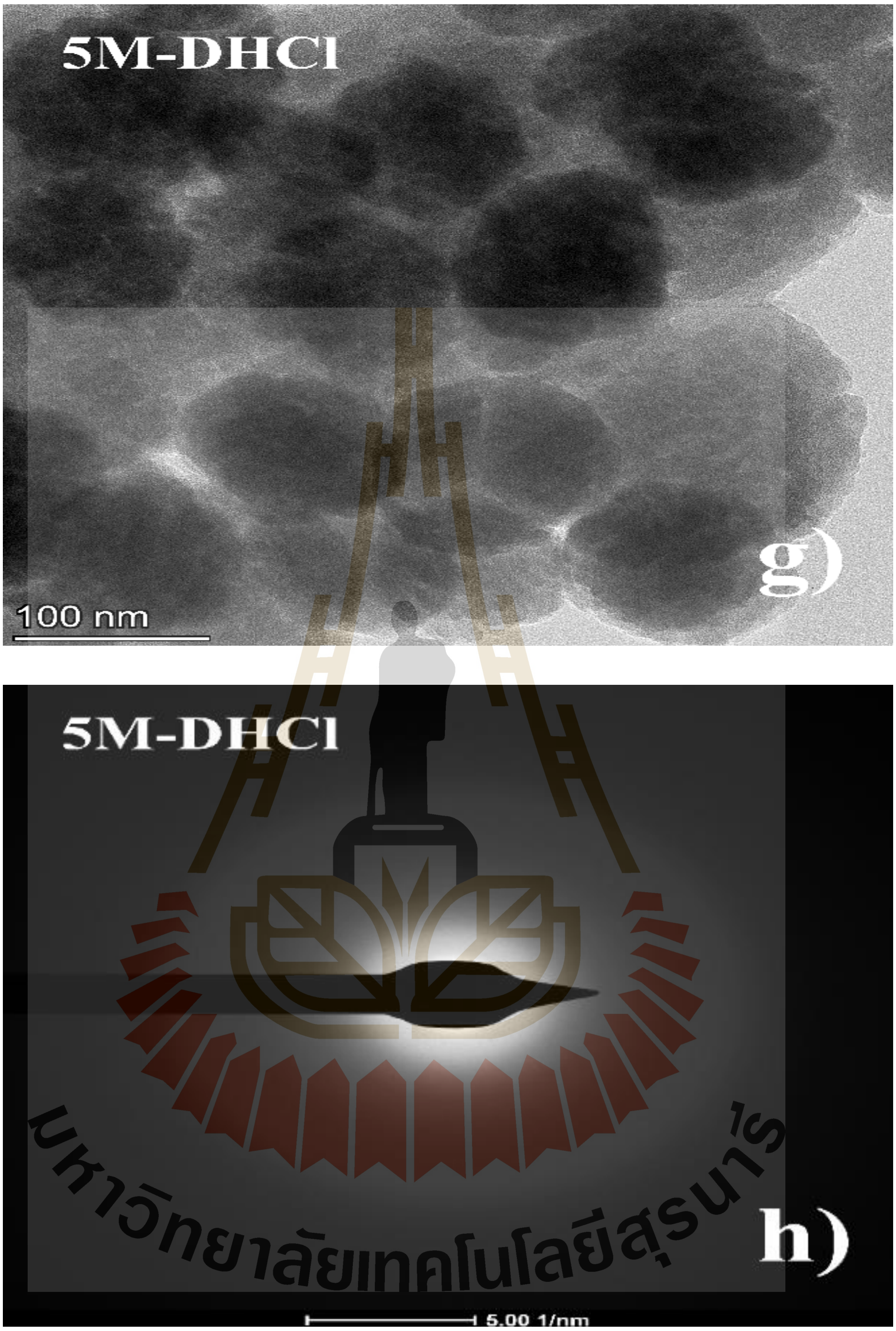

Figure 5.4 TEM and SEAD images of 0.1MDHCl (a, b), 0.5MDHCl (c, d), 1MDHCl (e, f), and 5MDHC (g, h) (Continued).

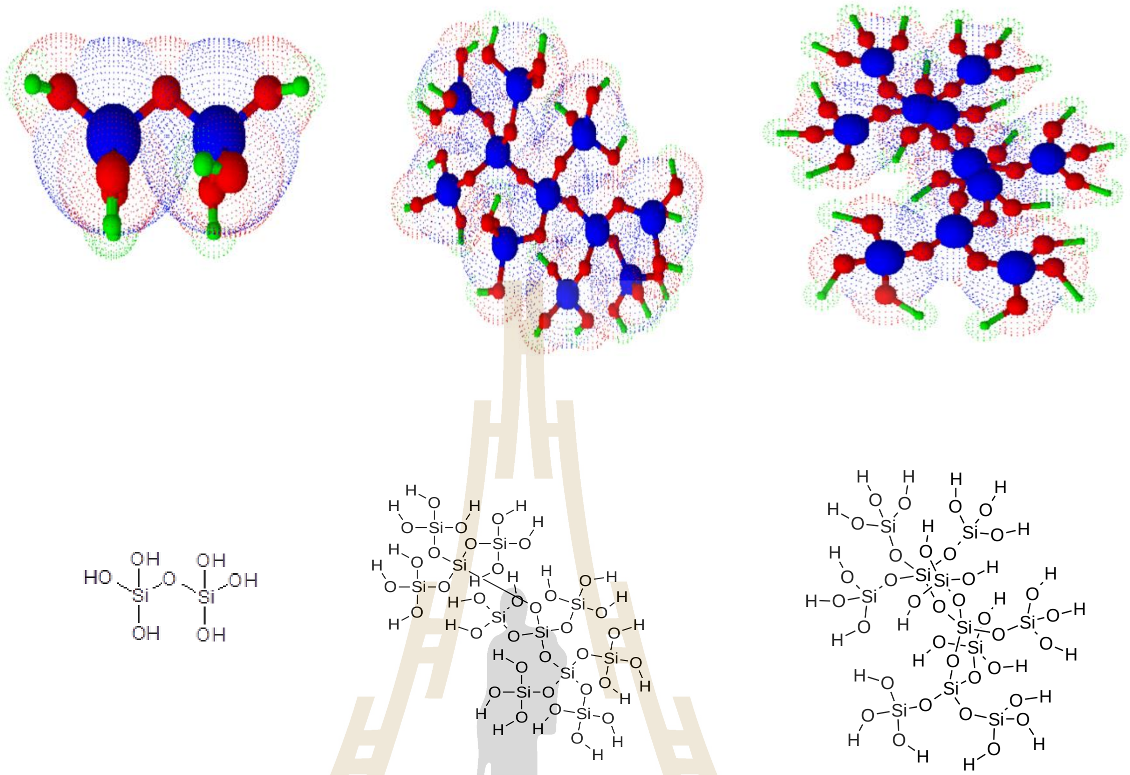

Figure 5.5 The SiO_2 models after 2nd HCl etching at 90°C for 3h.

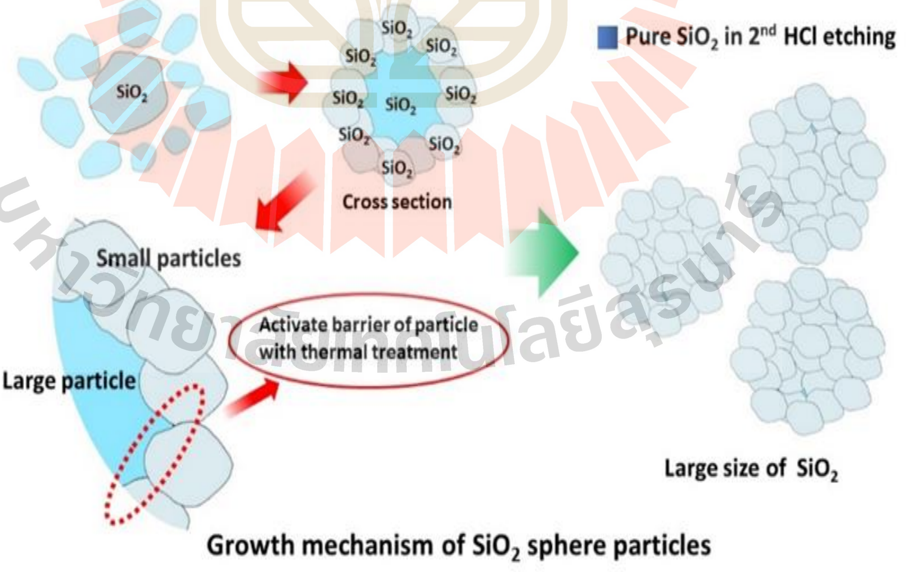

Figure 5.6 The growth mechanism of SiO_2 sphere particles after 2nd HCl etching at 90°C for 3h and calcined at 700°C.

For the reason of many small particles at high concentration more than low concentration, we have to back in the reaction of HCl etching process. In equation (4.7), final product of SiO_2 in this process is in solid that it is not react with HCl but in this experiment, the reaction of HCl and SiO_2 able to happen. But, SiO_2 and HCl reaction in this process will not direct happen. From initial materials, SiO_2 mass have 96-97% of purity of powder, which the structure of powder is in a compound.

Thereby, structure of powders able to write in $xSiO_2$ where x is another element, as described above. In the process, the break bond of X-Si-O structure able to happen by ability of HCl. During the process of break bond of X-Si-O, X element removed from bond, after that X bond with Cl. Likewise, the hydrochloric react with the Si-O again, in this process the hydrogen ions will react with the SiO_2 surface leading to the information of silicic acid (H_4SiO_4). This reaction can be represented follows ((4.8) (Rimstidt and Barnes, 1980).

$$SiO_2\ (s) + 4H^+\ (aq) \longrightarrow H_4SiO_4\ (aq) \qquad (4.8)$$

Moreover, The SiO_2 models of silicic acid can be illustrate in Figure 5.5. After reaction of SiO_2 and hydrochloric, SiO_2 size reduced. The small particle of SiO_2 will agglomerate, when using calcined again. SiO_2 structure able to simple agglomeration in which an agglomeration can contribute to an increase in particle size. Moreover, thermal effect is one reason of an increase in the particle size due to calcination process after the second HCl etching. The agglomeration of particle increases because high temperature has high thermal energy for particle to overcome rearrange atomic structure and activate barrier of particle. Hence, the second calcination caused to merge and form larger structure, as revealed the model in Figure 5.6

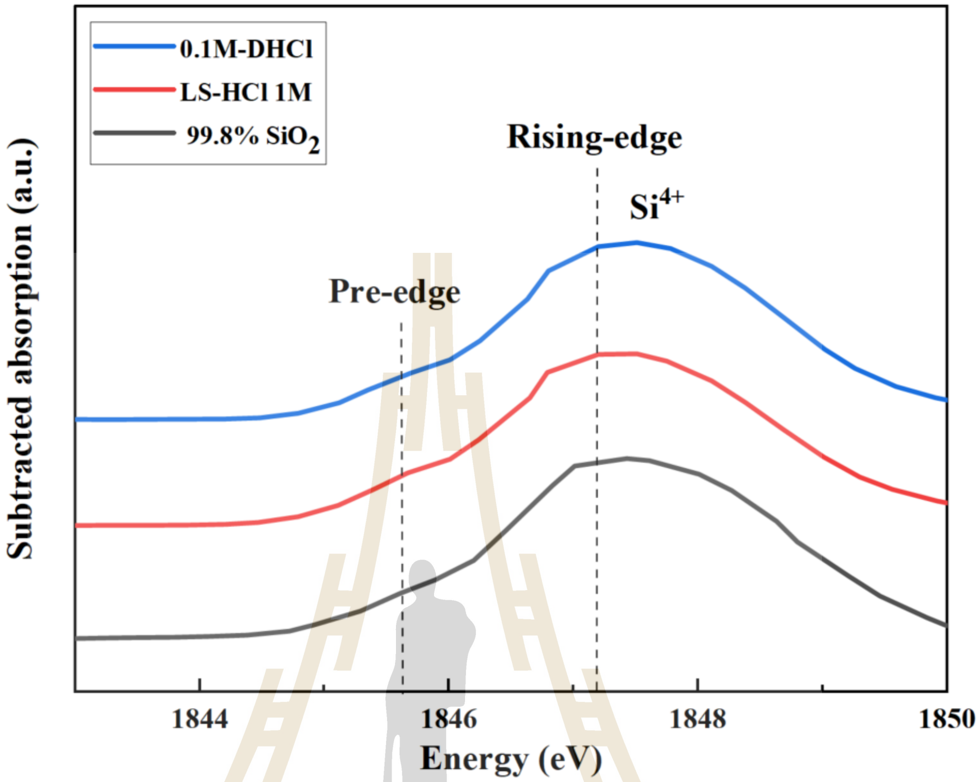

Figure 5.7 The absorption energy spectrum of LS-HCl 1M, 0.1MDHCl, and 99.8SiO$_2$ at 1835-1855 eV.

Comparison of the energy absorption characteristics of 99.8% SiO$_2$, LS-HCl 1M, and 0.1M DHCl revealed similarities in peak positions between the spectra of LS-HCl 1M and 99.8% SiO$_2$ samples, resembling that of the 0.1M DHCl sample when considering the pre-edge and rising-edge, as depicted in Figure 5.7. Upon fitting the pre-edge and rising-edge peaks of the 0.1M DHCl sample, values of 1845.9 and 1847.6 were obtained, respectively.

Consequently, no changes in peak positions of the 0.1M DHCl sample suggests a similarity in the oxidation state of the Si atom within its structure compared to the 99% SiO$_2$ and LS-1M HCl samples. Furthermore, an increase in the concentration of HCl for SiO$_2$ powder etching did not result in any observable changes in peak positions, as seen in Figure 5.8 and fitting data in Table 5.2.

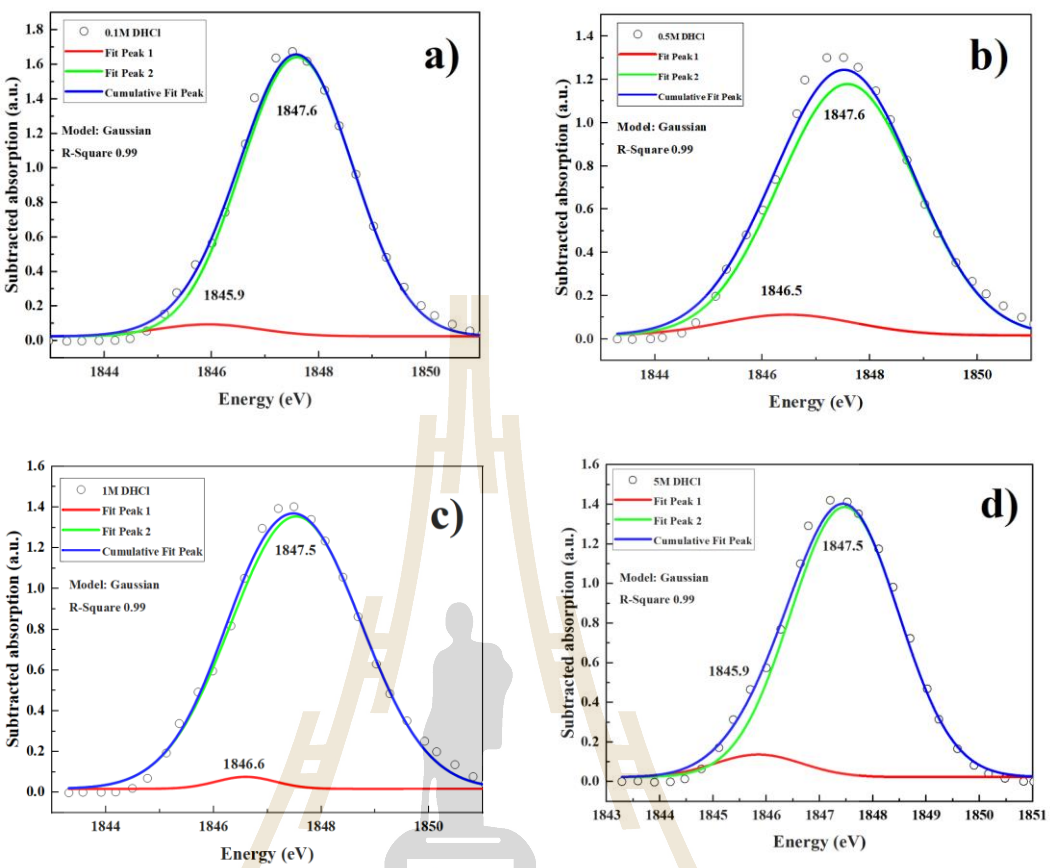

Figure 5.8 The fitting of absorption energy spectrum of 0.1MDHCl, 0.5MDHCl, 1MDHCl, and 5MDHCl.

Table 5.2 The peaks position of pre-edge (peak1) and rising-edge (peak2) of 0.1M DHCl, 0.5M DHCl, 1M DHCl, and 5M DHCl.

Position of absorption energy	Samples			
	0.1M DHCl	0.5M DHCl	1M DHCl	5M DHCl
Peak1	1845.9	1846.5	1846.6	1845.9
Peak2	1847.6	1847.6	1847.5	1847.8

5.2 The production of pure SiO_2 nanoparticles via nitric acid etching

In the work in the SiO_2 extraction from bio-source, the nitric acid is one of the strong acids like a hydrochloric for reduced impurity. In an experiment, researcher is interested in the effect of nitric for enhance purity of SiO_2 nanoparticles. Consequently, this work, using reflux for 2nd HNO_3 etching at 0.1-5M and calcination at 700°C for 3h, for study of SiO_2 structure divided into 4 samples: 0.1MDHNO_3, 0.5MDHNO_3, 1MDHNO_3, and 5MDHNO_3, as seen in Figure 5.9. The purity of SiO_2 yield after etching with nitric, mass fraction of SiO_2 is about 97.3%, which is increased 1-2% from SiO_2 ash sample. The SiO_2 yields able to show in Table 5.3. The effect of nitric is one reason of an increase impurity because when nitric mixed with pure water, the chemical reaction was produced hydronium ion (H_3O^+). This reaction can be represented follows Equation (4.9).

$$HNO_3\,(aq) + H_2O\,(aq) \longrightarrow H_3O^+\,(aq) + NO_3^- \tag{4.9}$$

The impurity of SiO_2 ash decreased from X-Si-O structure, when hydronium acid reacts with SiO_2 ash. The ability of hydronium acid able to break bond of X-Si-O. During the process, X element removed from bond, this process like a hydrochloric etching, as described above.

(a) (b) (c) (d)

Figure 5.9 White powders of SiO_2 of 0.1MDHNO_3, 0.5M DHNO_3, 1MDHNO_3, and 5M DHNO_3.

Table 5.3 The XRF results of 0.1MDHNO$_3$, 0.5M DHNO$_3$, 1M DHNO$_3$, and 5M DHNO$_3$.

Samples	Mass fraction of the element and element oxide (%)							
	SiO_2	K_2O	CaO	P_2O_5	Fe_2O_3	MnO_2	SO_3	Cl
0.1M DHNO$_3$	97.18	0.38	0.66	-	0.4	1.39	-	-
0.5M DHNO$_3$	97.00	0.44	0.70	-	0.67	1.68	-	-
1M DHNO$_3$	97.28	0.25	0.77	-	0.56	1.14	-	-
5M DHNO$_3$	97.07	0.44	0.74	-	0.37	1.39	-	-

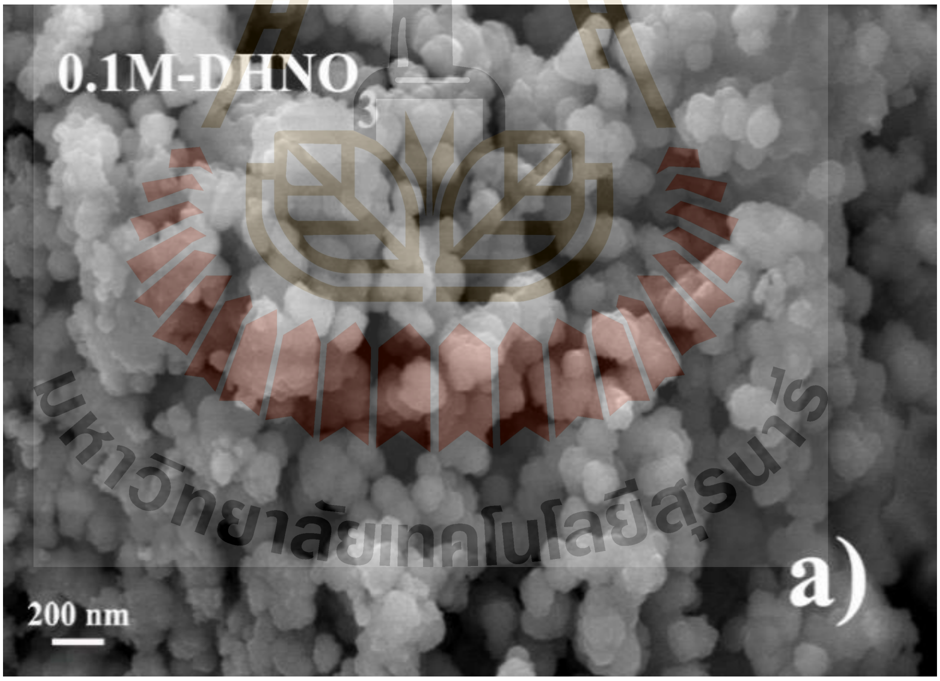

Figure 5.10 FE-SEM images of 0.1MDHNO$_3$, 0.5M DHNO$_3$, 1M DHNO$_3$, and 5M DHNO$_3$.

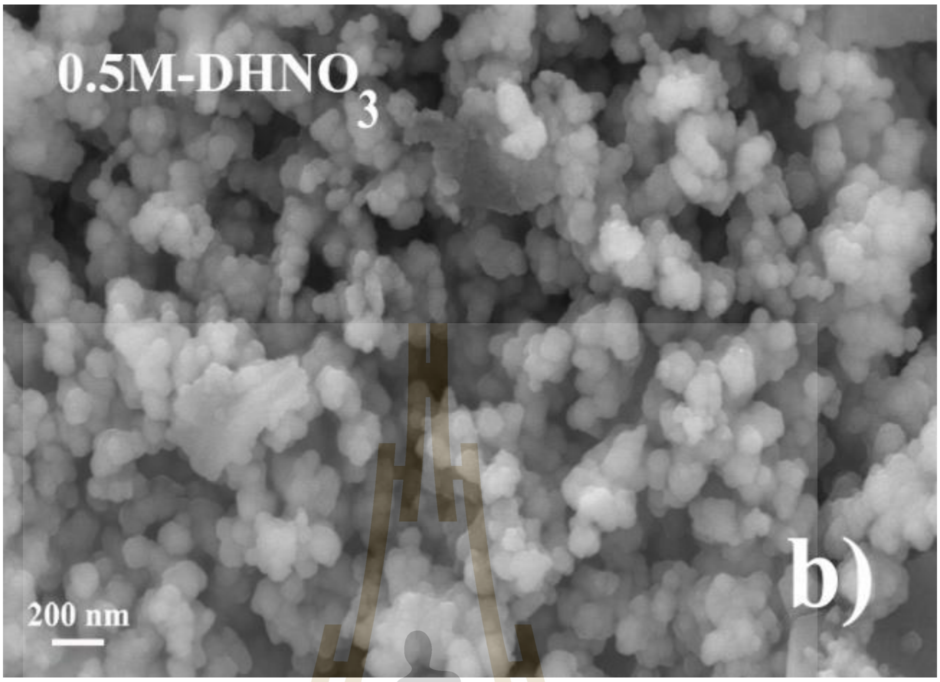

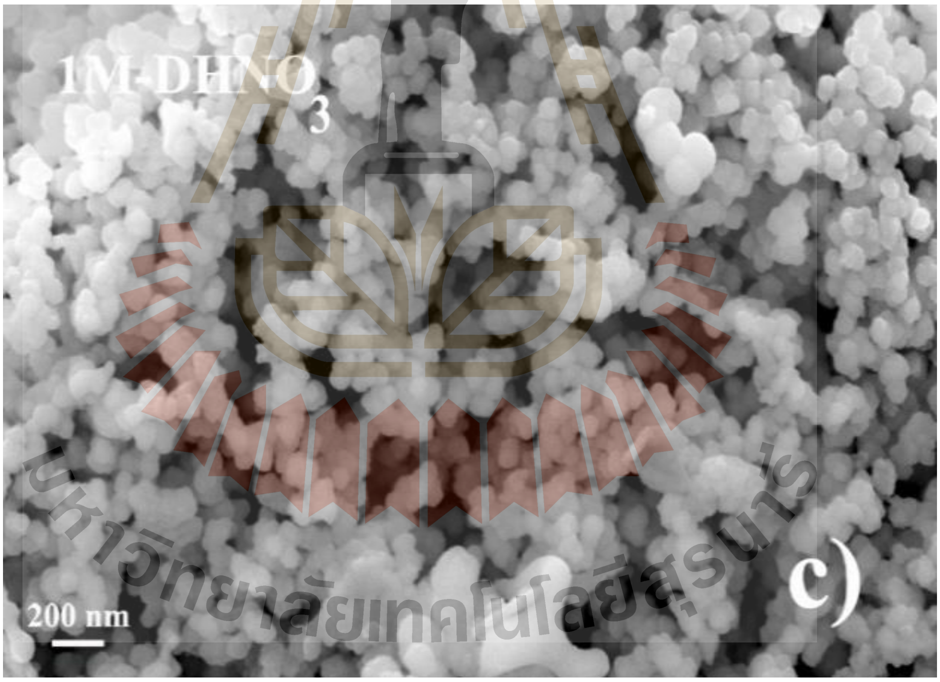

Figure 5.10 FE-SEM images of 0.1MDHNO$_3$, 0.5M DHNO$_3$, 1M DHNO$_3$, and 5M DHNO$_3$ (Continued).

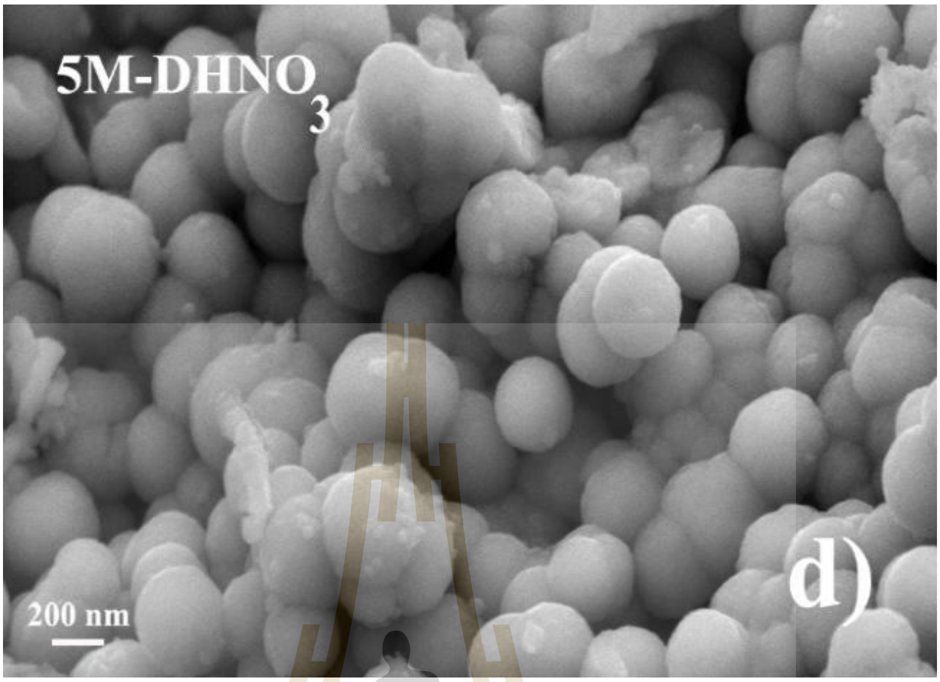

Figure 5.10 FE-SEM images of 0.1MDHNO$_3$, 0.5M DHNO$_3$, 1M DHNO$_3$, and 5M DHNO$_3$ (Continued).

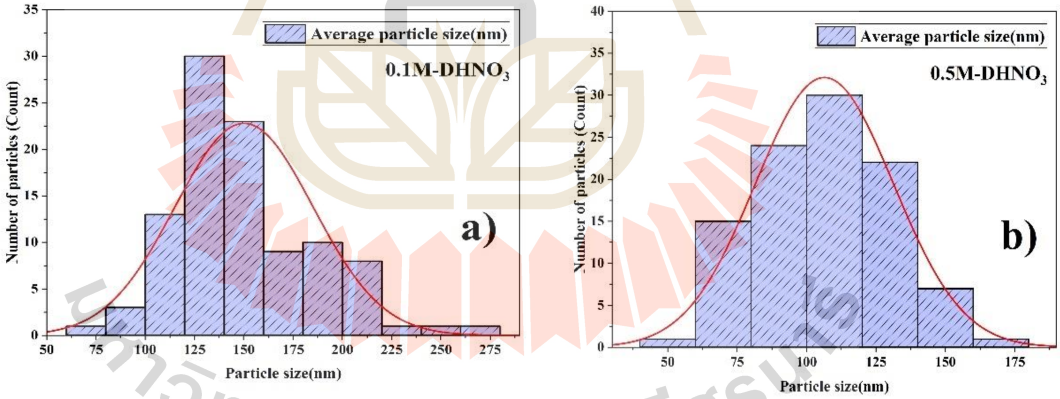

Figure 5.11 Average particle size of 0.1MDHNO$_3$, 0.5M DHNO$_3$, 1M DHNO$_3$, and 5M DHNO$_3$.

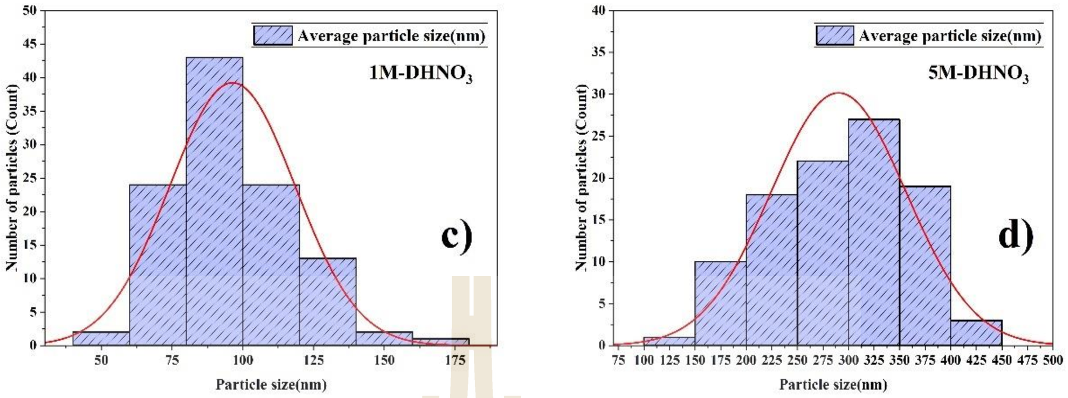

Figure 5.11 Average particle size of 0.1MDHNO$_3$, 0.5M DHNO$_3$, 1M DHNO$_3$, and 5M DHNO$_3$ (Continued).

The particles of DHNO$_3$ samples reveals the shape to be composed of sphere, the average size of particles in this process is 100-150 nm (at 0.1-1M of DHNO$_3$), and the big size exhibited in 5M-DHNO$_3$ sample, SiO$_2$ size is around 250 nm, as shown the sphere and average size of SiO$_2$ particle in Figure 5.10 and Figure 5.11, respectively. The increase in SiO$_2$ size is caused by chemical and thermal effects, including the treatment of SiO$_2$ ash with HCl, as demonstrated in the previous chapter. Moreover, the TEM image depicted in Figure 5.12, it is the insight of white powder of pure SiO$_2$ of 0.1MDHNO$_3$ (as shown in Figure 5.12a), 0.5MDHNO$_3$(as shown in Figure 5.12c), 1MDHCl (as shown in Figure 5.12e) and 5MDHNO$_3$(as shown in Figure 5.12g). Likewise, SAED images of 0.1MDHCl, 0.5MDHCl, 1MDHCl, and 5MDHCl were revealed in Figure 5.12b, Figure 5.12d, Figure 5.12f, and Figure 5.12h, respectively. From TEM image of samples, the insight of particles of samples are in a form of sphere and the particles separate into individual particles, which is difference from treatment SiO$_2$ with hydrochloric, as depicted above. The reason for the sphere shape of single particle, it may be depended on ability of HNO$_3$ for the chemical decomposition. we have to back in the reaction of HNO$_3$ etching process. In Equation (4.9), final product of HNO$_3$ decomposition is hydronium and salt of nitrate. As described above, while hydronium ion reacts with SiO_2 structure leading to the information of silicic acid (H_4SiO_4), as shown in Equation (4.8).

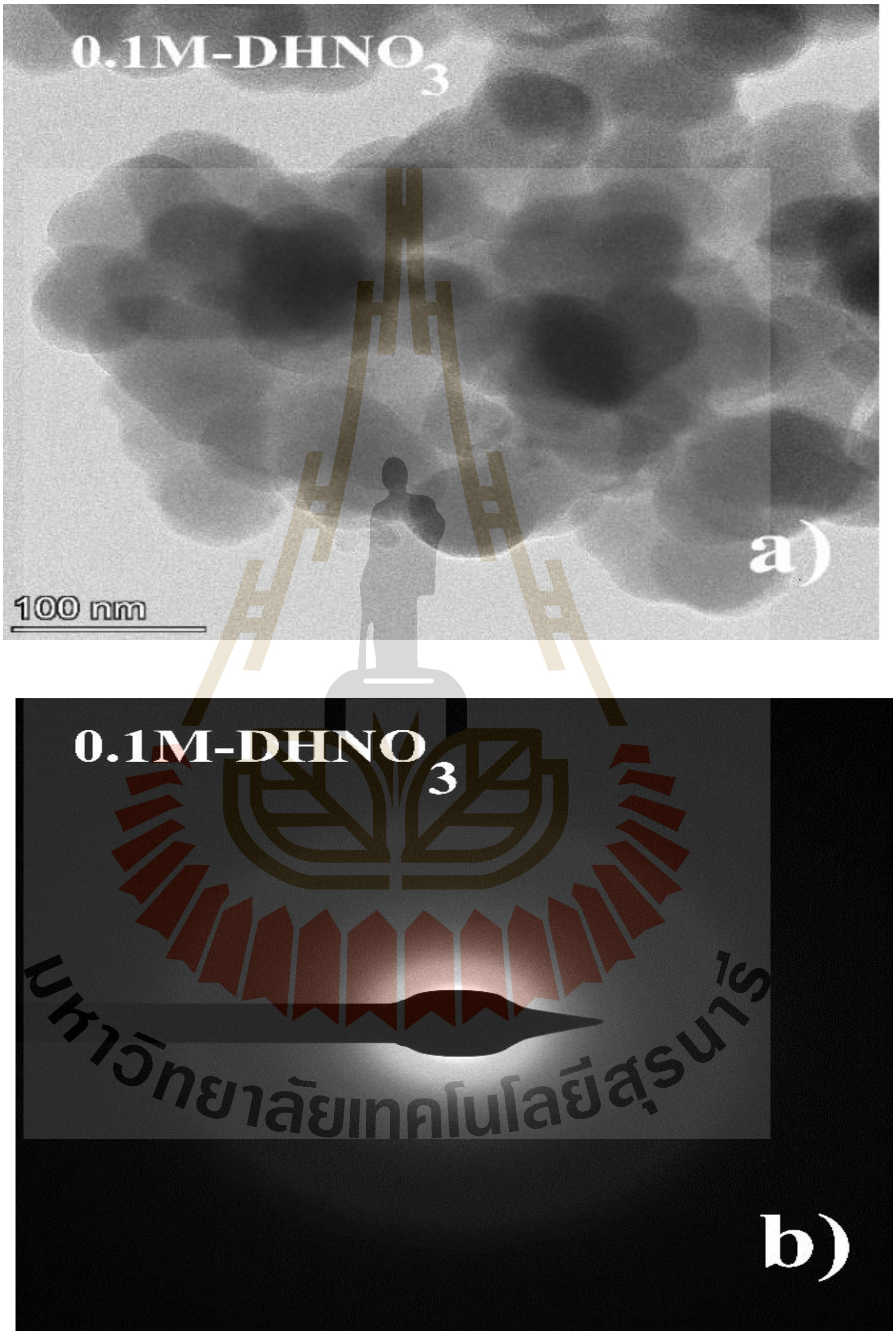

Figure 5.12 TEM and SEAD images of $0.1MDHNO_3$ (a, b), $0.5MDHNO_3$ (c, d), $1MDHNO_3$ (e, f), and $5MDHNO_3$ (g, h).

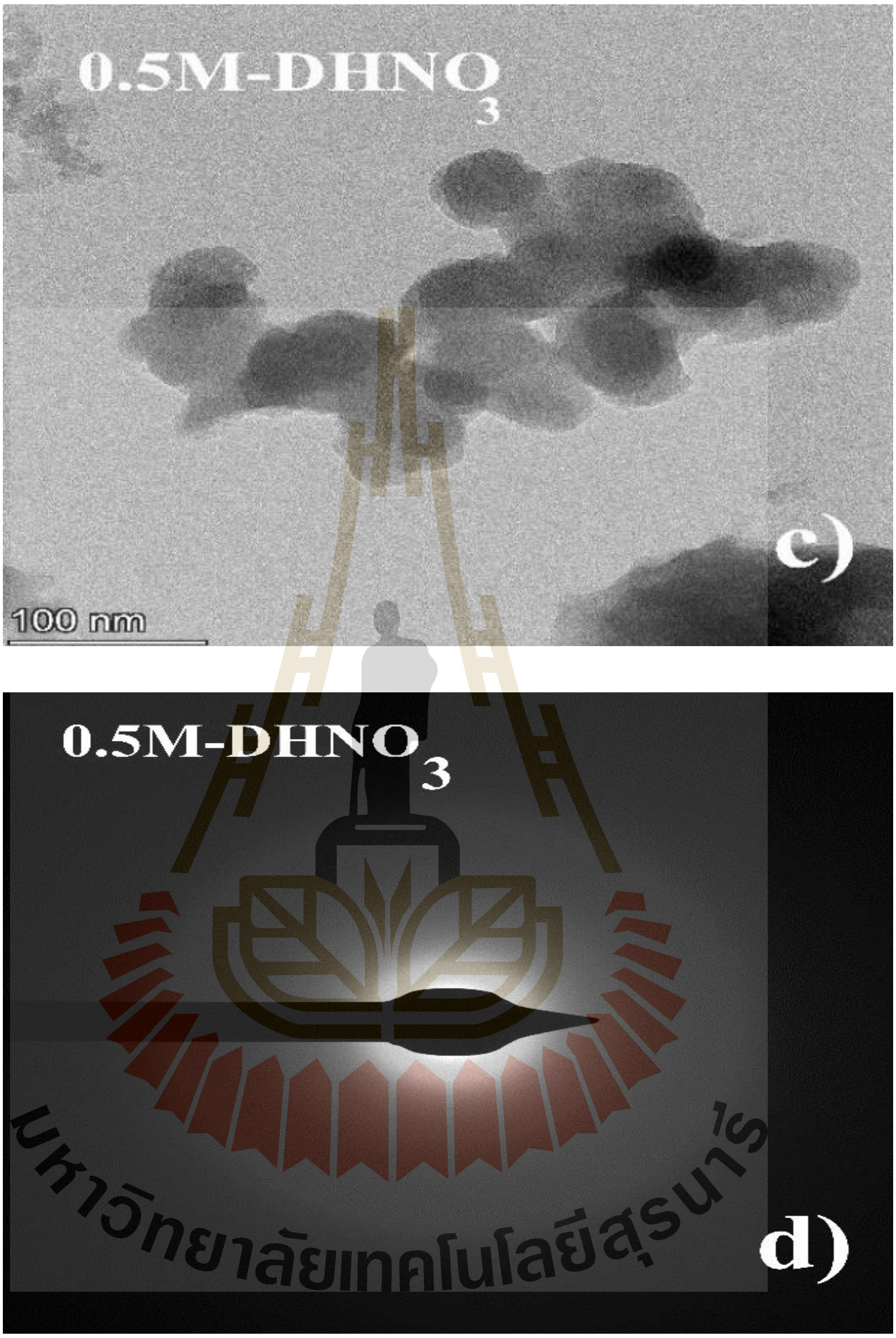

Figure 5.12 TEM and SEAD images of 0.1MDHNO$_3$ (a, b), 0.5MDHNO$_3$ (c, d), 1MDHNO$_3$ (e, f), and 5MDHNO$_3$ (g, h) (Continued).

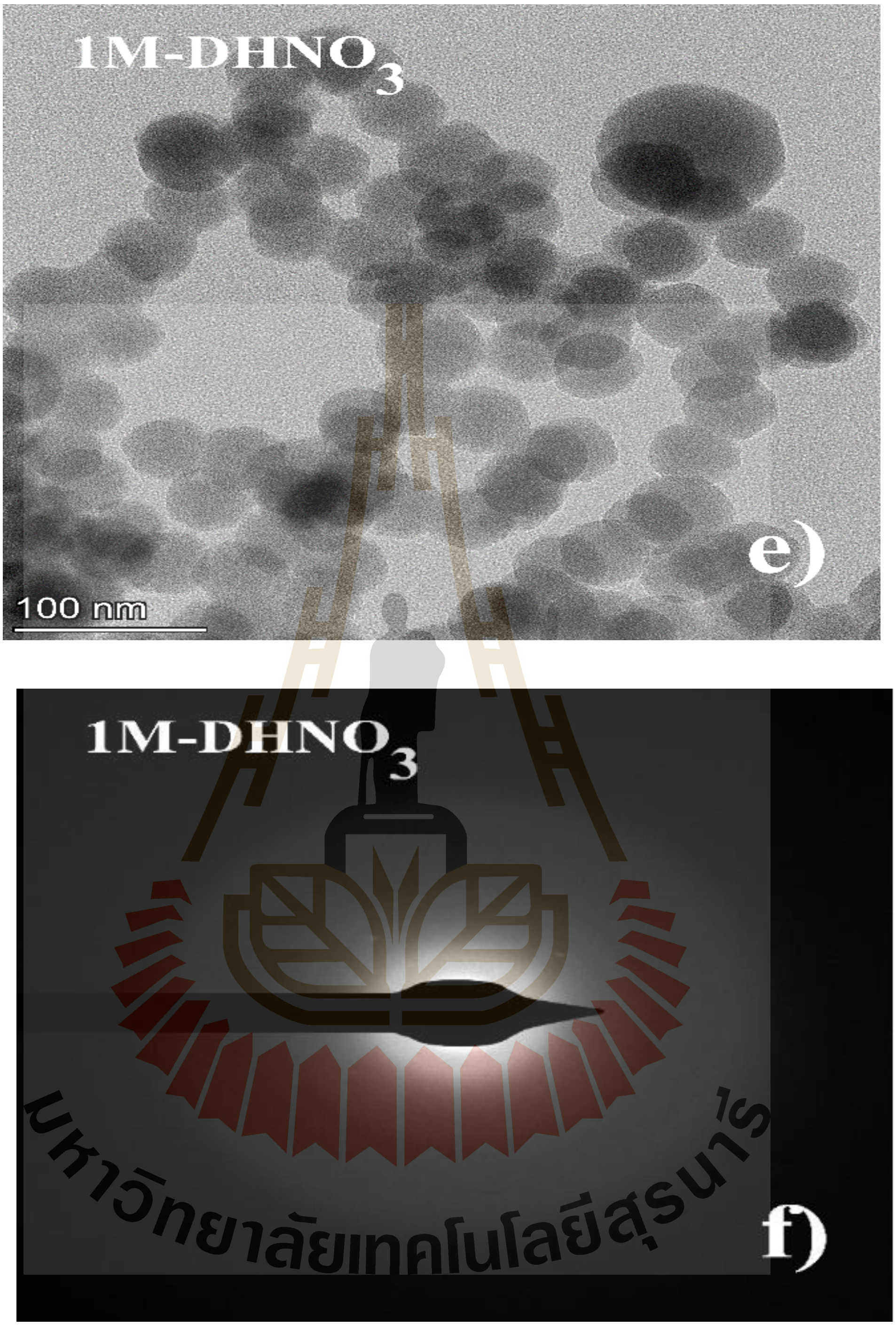

Figure 5.12 TEM and SEAD images of 0.1MDHNO$_3$ (a, b), 0.5MDHNO$_3$ (c, d), 1MDHNO$_3$ (e, f), and 5MDHNO$_3$ (g, h) (Continued).

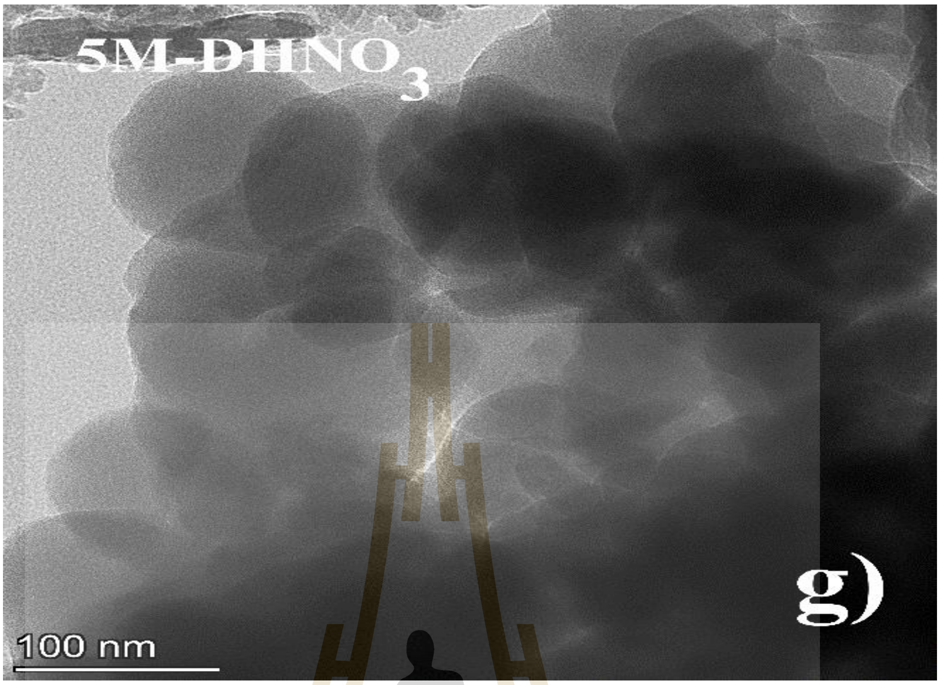

Figure 5.12 TEM and SEAD images of 0.1MDHNO$_3$ (a, b), 0.5MDHNO$_3$ (c, d), 1MDHNO$_3$ (e, f), and 5MDHNO$_3$ (g, h) (Continued).

Subsequently, H_4SiO_4 will react with NO_3^- lead to the formation of HN_3 and silicate species. This reaction can be represented follows Equation (4.10)

$$H_4SiO_4+3N^{-} \longrightarrow HN_3+\text{ silicate species} \qquad (4.10)$$

Following the calcination process, silicate species were formed into individual SiO_2 spheres, as depicted in Figure 5.12. Moreover, silicate species models after the interaction of silica with HNO_3, as shown in Figure 5.13. However, as illustrated in Figure 5.13, the nitrate was boning on the surface of silica, which is in the form of silicate species. The simple model of silicate species can be classified into two: silicate species1 and silicate species 2. Couple models were reported by N. A. Saliba et al., in 2001.

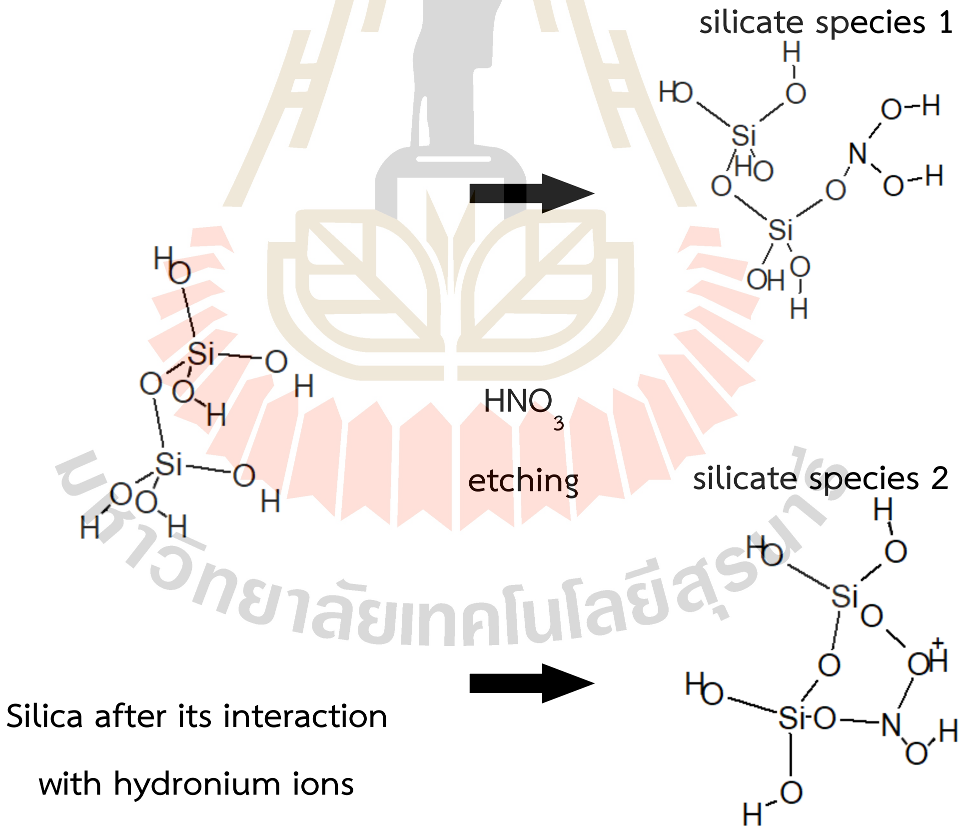

Figure 5.13 Model of reaction of HNO_3 on silicon dioxide after its interaction with hydronium ion (Saliba, Yang et al., 2001).

From the silicate species1 and silicate species 2, It aids in our understanding about SiO_2 growth mechanism, when treated SiO_2 ash with HNO_3. When particles are treated with nitric acid, it will lead to a nitrate covering forms on their surface, acting like a shell to prevent chemical reactions from occurring between the particles. Therefore, SiO_2 particles cannot bond with each other, lead to the production of single particle after calcination, as seen in TEM images. Furthermore, the simple model of nitrate shell on surface of SiO_2 can be seen in Figure 5.14.

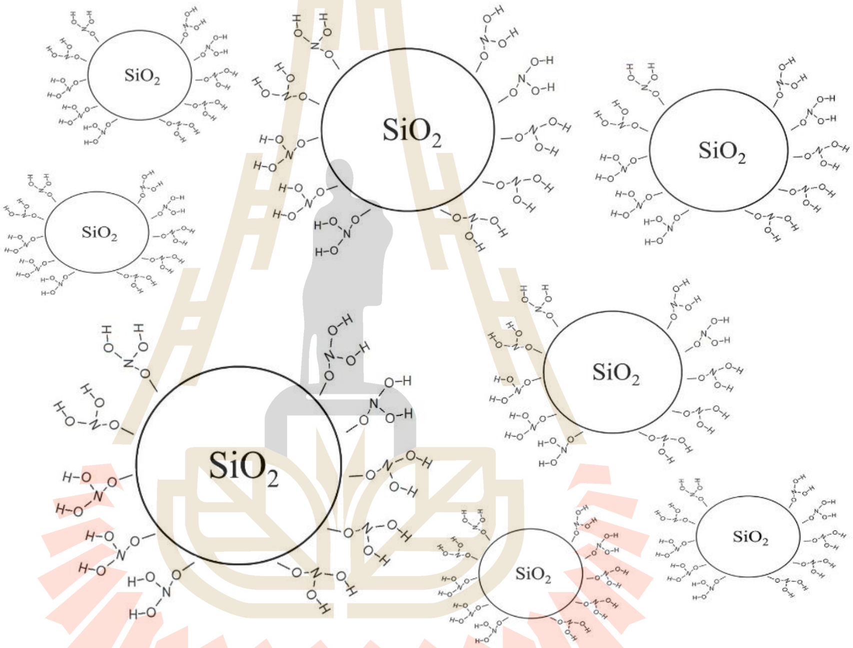

Figure 5.14 the simple model of nitrate shell on surface of SiO_2 after treated SiO_2 particle with HNO_3.

When comparison of the energy absorption of 99.8% SiO_2, LS-HCl 1M, and 0.1M $DHNO_3$ in range energy absorption from 1835 to 1850 eV revealed identity in peak positions of three samples, considering the pre-edge and rising-edge, as depicted in Figure 5.15. Upon calculating the pre-edge and rising-edge peaks of the 0.1M DHCl sample using Gaussian fitting, values of 1845.1 and 1847.5 were obtained, respectively.

Therefore, the absence of changes in peak positions of the 0.1M $DHNO_3$ sample suggests a similarity in the oxidation state of the Si atom within its structure compared to that of the 99% SiO_2 and LS-1M HCl samples. Moreover, an increase in the concentration of HNO_3 for SiO_2 powder etching did not lead to any observable changes in peak positions, as depicted in Figure 5.16 and data in Table 5.4.

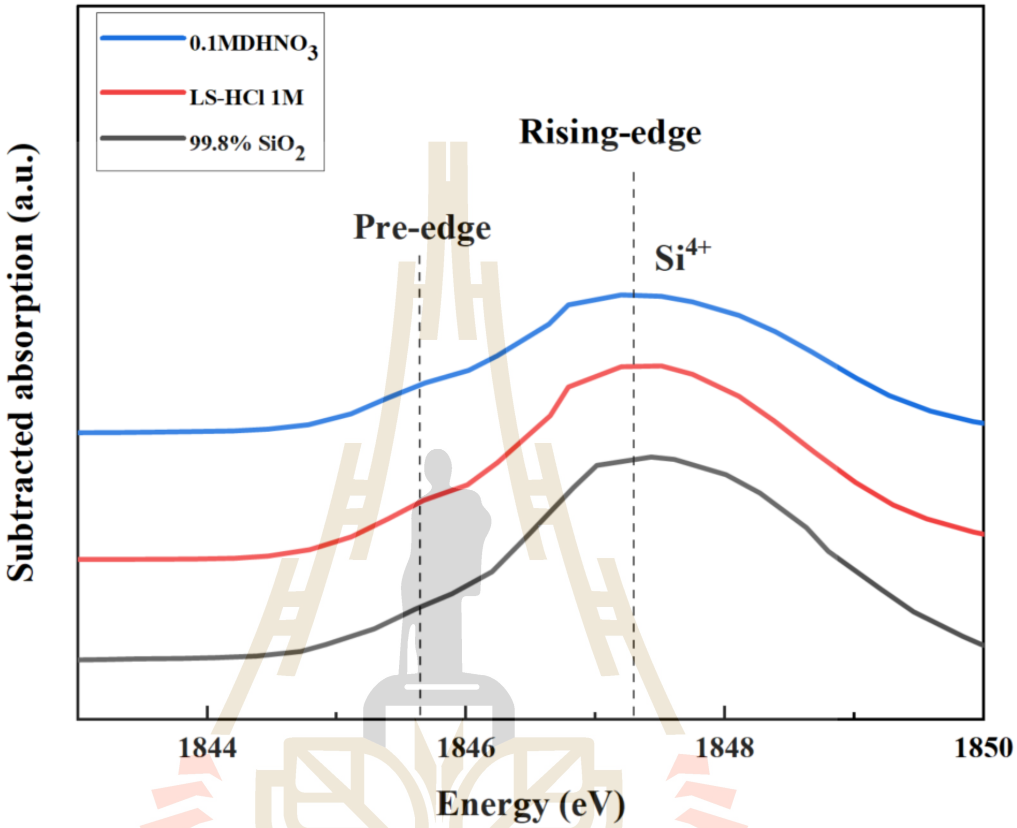

Figure 5.15 The absorption energy spectrum of LS-HCl 1M, 0.1MDHNO$_3$, and 99.8SiO$_2$ at 1835-1855 eV.

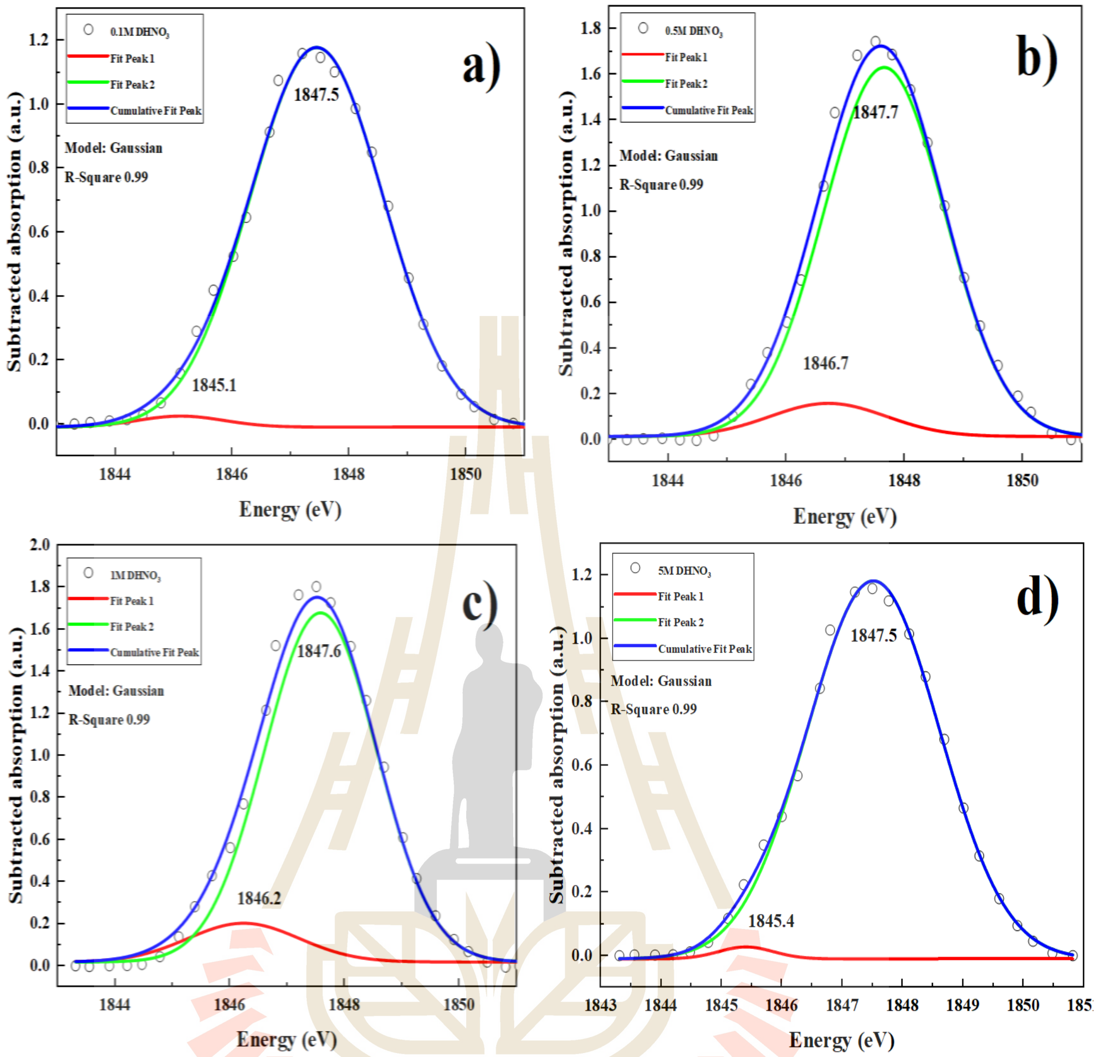

Figure 5.16 The absorption energy spectrum fit of 0.1MDHNO$_3$, 0.5M DHNO$_3$, 1M DHNO$_3$, and 5M DHNO$_3$.

Table 5.4 The peaks position of pre-edge (peak1) and rising-edge (peak2) of 0.1MDHNO$_3$, 0.5M DHNO$_3$, 1M DHNO$_3$, and 5M DHNO$_3$.

Position of absorption energy	Samples			
	0.1M DHNO$_3$	0.5M DHNO$_3$	1M DHNO$_3$	5M DHNO$_3$
Peak1	1845.1	1846.7	1846.2	1845.4
Peak2	1847.5	1847.7	1847.6	1847.5

5.3 Summary of the Second Methodology

Experiments, the synthesized pure SiO$_2$ samples using the second methodology able to draw the following conclusions:

XRF results: From the chemical reaction between H$^+$ (or H$_3$O$^+$) and SiO$_2$ ash, the material purity of SiO$_2$ is high when SiO$_2$ ash is treated with 0.1 HCl. It was found that the maximum SiO$_2$ purity is 99.7% for the 0.1MDHCl sample, as described above in chapter 5.1. Likewise, 97.2% of SiO$_2$ purity was obtained when SiO$_2$ ash is treated with 0.1M HNO$_3$, as shown result in chapter 5.2.

Fe-SEM results: The shape of SiO$_2$ particles when treated with HCl or HNO$_3$ appears to be spherical. The size of SiO$_2$ particles increases with the concentration of the acid, resulting in sizes ranging from approximately 60-200 nm for DHCl samples with concentrations of 0.1-1M, and approximately 100-150 nm for samples treated with HNO$_3$ (0.1-1M). The size of particles increases due to the chemical effect and thermal effects.

TEM results: As shown sphere shape of SiO$_2$ particles after treated with couple acids, the insight of particles observed a difference of particles shape. Treatment of SiO$_2$ ash particles with HCl, the shape of particle was seen that there is gathering of small SiO$_2$ particles for particles size increases. The opposite way, when SiO$_2$ particles is treated with HNO$_3$, the particles size increases, it is results in expanding the single crystal. Furthermore, the different crystal growth from the different acid etching results in SiO$_2$ particles having differences in surface of particles

XAS results: In results of XANES analysis, SiO_2 is not shift of pre-edge and rising, when comparing samples between LS-HCl 1M and 1M DHCl. Therefore, the oxidation state of DHCl 1M, acting like a LS-HCl sample.

CHAPTER VI

CONCLUSIONS AND RECOMMENDATIONS FOR FUTURE RESEARCH

6.1 Conclusions

Base on the results from chapter IV and chapter V, it has been shown that the SiO_2 ash able to obtain from Actinoscirpus Grossus via using HCl and HNO_3 etching that it is simplify method for synthesis. Furthermore, this method is significant for material purity, nanostructure, and the mechanism of material growth behavior of high-purity SiO_2 nanoparticles. The preprimary trend delineated in this work able to conclude follow below:

(1) The SiO_2 nanoparticles able to prosperous synthesis by employing first HCl acid etching method. With the addition of the HCl etching in the synthesis process, the morphology of SiO_2 nanoparticles is in amorphous form and has a size in the range of 50-100 nm, whereas the smallest obtainable size of particle was observed in low concentration of HCl acid. Furthermore, the effect of the first etching with 1M HCl for materials purity is investigated and it found that the SiO_2 nanoparticle has a high purity as high as 96% of SiO_2 mass fraction. The Si structure has the oxidation state to be 4+.

(2) The 97.0-99.8% of purity SiO_2 nanoparticles can be successfully formed by using second acid etching method. amongst the two acids etching, the effect of acid help to reduce an impurity on SiO_2 nanoparticles. The shape of particles is in the form of sphere and has a size in the range of 60-200 nm. Moreover, high concentration of acid and double calcination lead to a big SiO_2 nanoparticles in this process. The surface of SiO_2 nanoparticles has rough when treated with HCl and has smooth when treated with HNO_3. Moreover, in second etching, the effect of HCl acid and HNO_3 in the synthesis process caused the Si structure to be in the form of Si^{4+} which is the same oxidation state as compared with the results in first etching process.

The purity of SiO_2 nanoparticles in this process is the same purity as compared with the SiO_2 nano particles from industry.

Therefore, it can be seen from this work that the second etching is a critical process for synthesizing pure SNPs

6.2 Recommendations for further work

The number of interesting problems that still cannot be answered concerns the relationship between the growth mechanism rate and the nanostructure properties of SiO_2 after using the second acid etching. Hence, it is interestingly point for the further work. The suggestion of this problem has 6 parts:

(1) This works that still cannot control a size of SiO_2 nanoparticles through growth mechanism process after SiO_2 is treated with acid in second etching process.

(2) This works that still cannot answers the question:" how does the growth mechanism rate affect the nanostructure properties of SiO_2?"

(3) The cost of synthesizing 99.8% pure silica for this experiment remains high, as shown in the table in the appendix. This cost is a rough estimate, and the high price results from the preparation process, where a single firing can process only 50-100 grams of raw material. This limitation is due to the size of the furnace, which makes the cost per preparation high. To reduce the cost of synthesis, a larger furnace should be used.

(4) Further work on the nanostructure characterization (e.g., via BET and UV-VIS), especially focusing on the porosity and energy gap of SiO_2, is essential for trending to develop into innovation.

(5) Further work arising directly from this study should focus on the device production via high-pure SiO_2 particles (e.g., moiture sensor, light sensor, or/and gas sensor.

(6) Future work, if possible, should further focus on transforming the SiO_2 structure into SiC and/or SiN.

REFERENCES

REFERENCES

Abualnoun Ajeel, S., K. A., and Zedin, N. K. (2020). Extraction of high purity amorphous silica from rice husk by chemical process. *IOP Conference Series: Materials Science and Engineering. 881*(1), 012096.

Al-Baldawi, I. A., Abdullah, S. R. S., Anuar, N., and Idris, M. (2013). Phytotoxicity test of Scirpus grossus on diesel-contaminated water using a subsurface flow system. *Ecological Engineering. 54*, 49-56.

Al-Baldawi, I. A., Abdullah, S. R. S., Anuar, N., Suja, F., and Mushrifah, I. (2015). Phytodegradation of total petroleum hydrocarbon (TPH) in diesel-contaminated water using Scirpus grossus. *Ecological Engineering. 74*, 463-473.

Alemdar, A., Güngör, N., Ece, O., and Atici, O. (2005). The rheological properties and characterization of bentonite dispersions in the presence of non-ionic polymer PEG. *Journal of Materials Science. 40*(1), 171-177.

Almaamary, E. A. S., Abdullah, S. R. S., Hasan, H. A., Rahim, R. A. A., and Idris, M. (2017). Treatment of methylene blue in wastewater using Scirpus grossus. *Malaysian Journal of Analytical Sciences. 21*(1), 182-187.

Almaamary, E. A. S., Abdullah, S. R. S., Hasan, H. A., Rahim, R. A. A., and Idris, M. (2019). Extraction of high-purity silica from rice husk via hydrochloric acid leaching treatment. *Turkish Journal of Chemistry. 43*(5), 1258-1269.

Azizi, S. N. and M. Yousefpour (2008). Spectroscopic Studies of Different Kind of Rice Husk Samples Grown in North of Iran and the Extracted Silica by Using XRD, XRF, IR, AA and NMR Techniques. *Eurasian Journal of Analytical Chemistry. 3*(3).

Bakhat, H. F., Bibi, N., Zia, Z., Abbas, S., Hammad, H. M., Fahad, S., and Saeed, S. (2018). Silicon mitigates biotic stresses in crop plants: A review. *Crop Protection. 104*, 21-34.

Belskaya, O. B., Danilova, I. G., Kazakov, M. O., Mironenko, R. M., Lavrenov, A. V., and Likholobov, V. A. (2012). FTIR spectroscopy of adsorbed probe molecules for analyzing the surface properties of supported Pt (Pd) catalysts. *Infrared Spectroscopy in Materials Science, Engineering and Technology, PT Theophile, Ed., ed: InTech, Croatia*, 149-178.

Boguta, P., Sokołowska, Z., and Skic, K. (2017). Use of thermal analysis coupled with differential scanning calorimetry, quadrupole mass spectrometry and infrared spectroscopy (TG-DSC-QMS-FTIR) to monitor chemical properties and thermal stability of fulvic and humic acids. *Public Library of Science. 12*(12), e0189653.

Boonsuk, P., Sukolrat, A., Bourkaew, S., Kaewtatip, K., Chantarak, S., Kelarakis, A., and Chaibundit, C. (2021). Structure-properties relationships in alkaline treated rice husk reinforced thermoplastic cassava starch biocomposites. *International Journal of Biological Macromolecules. 167*, 130-140.

Bortolotto Teixeira, L., Guzi de Moraes, E., Paolinelli Shinhe, G., Falk, G., and Novaes de Oliveira, A. P. (2021). Obtaining biogenic silica from sugarcane bagasse and leaf ash. *Waste and Biomass Valorization. 12*, 3205-3221.

Budak, S., Parker, R., Smith, C., Muntele, C., Heidary, K., Johnson, R. B., and Ila, D. (2013). Superlattice multinanolayered thin films of SiO_2/SiO_2+Ge for thermoelectric device applications. *Journal of Intelligent Material Systems and Structures. 24*(11), 1357-1364.

Chaklader, A. and A. L. Roberts (1961). Transformation of quartz to cristobalite. *Journal of the American Ceramic Society. 44*(1), 35-41.

Chandrasekhar, P., Dubey, A., Reza, K. M., Hasan, M. N., Bahrami, B., Komarala, V. K., and Qiao, H. (2018). Higher efficiency perovskite solar cells using Au@SiO_2 core–shell nanoparticles. *Sustainable Energy and Fuels. 2*(10), 2260-2267.

ChemEssen. (2019). Structure of Silicic Acid (H_4O_4Si). Retrieved from https://www.molinstincts.com/structure/SILICIC-ACID-cstr-CT1001088833.html.

Chen, C., Jia, Z., Wang, X., Lu, H., Guan, Z., and Yang, C. (2015). Micro characterization and degradation mechanism of liquid silicone rubber used for external insulation. *IEEE Transactions on Dielectrics and Electrical Insulation. 22*(1), 313-321.

Corporation, C. L. S. (2022). Silicon Dioxide Powder. Retrieved from https://www.indiamart.com/proddetail/silicon-dioxide-powder 17951127855. html.

Cui, J., Liang, Y., Yang, D., and Liu, Y. (2016). Facile fabrication of rice husk based silicon dioxide nanospheres loaded with silver nanoparticles as a rice antibacterial agent. *Scientific Reports. 6*(1), 21423.

Currie, H. A. and C. C. Perry (2007). Silica in plants: biological, biochemical and chemical studies. *Annals of Botany. 100*(7), 1383-1389.

D.A.Simpson, G. (2017). Actinoscirpus grossus. Retrieved from https://powo.science.kew.org/taxon/962435-1.

Davy, H. (1808). XXIII. Electro-chemical researches, on the decomposition of the earths; with observations on the metals obtained from the alkaline earths, and on the amalgam procured from ammonia. *Philosophical Transactions of the Royal Society of London.* (98), 333-370.

Deshmukh, P., Bhatt, J., Peshwe, D., and Pathak, S. (2012). Determination of silica activity index and XRD, SEM and EDS studies of amorphous SiO2 extracted from rice husk ash. *Transactions of the Indian Institute of Metals. 65*, 63-70.

Farmer, A., Collings, A., and Jameson, G. (2000). The application of power ultrasound to the surface cleaning of silica and heavy mineral sands. *Ultrasonics Sonochemistry. 7*(4), 243-247.

Fernández, J. M., Hockaday, W. C., Plaza, C., Polo, A., and Hatcher, P. G. (2008). Effects of long-term soil amendment with sewage sludges on soil humic acid thermal and molecular properties. *Chemosphere. 73*(11), 1838-1844.

Firdaus, M. Y. N., Osman, H., Metselaar, H. S., and Rozyanty, A. R. (2016). A simple method for the production of pure crystalline silica from lemon grass. *BioResources. 11*(1), 1270-1279.

Fischer, H. (2015). X-Ray Fluorescence Spectroscopy (XRF) – Basics. Retrieved from https://xrf-spectroscopy.com.

Fleischer, M. (1953). Recent estimates of the abundances of the elements in the earth's crust: US Department of the Interior, Geological Survey.

Ganapathi, S. C., Holla, R., Shankara, S., Mundugaru, R., Sunilkumar, K., Rajagopal, R., and AlAnsari, A. (2021). Protective effect of ethanolic extract of Actinoscirpus grossus tubers against ethanol induced liver toxicity in albino rats. *Journal of King Saud University-Science. 33*(1), 101253.

Gay-Lussac, J. L. & Thénard, L. J. (1811). *Recherches Physico-Chimiques, Faites Sur La Pile; Sur La Préparation Chimique Et Les Propriétés Du Potassium Et Du Sodium; Sur La Décomposition De L'acide Boracique; Sur Les Acides Fluorique, Muriatique Et Muriatique Oxigéné; Sur L'action Chimique De La Lumière*; Sur L'analyse Végétale Et Animale, Etc. Paris, Deterville.

Ghasemi, Z. and H. Younesi (2011). Preparation and characterization of nanozeolite NaA from rice husk at room temperature without organic additives. *Journal of Nanomaterials. 2011*(1), 858961.

Ghasemi, Z., Younesi, H., and Kazemian, H. (2011). Synthesis of nanozeolite sodalite from rice husk ash without organic additives. *The Canadian Journal of Chemical Engineering. 89*(3), 601-608.

Goetghebeur, P. and D. Simpson (1991). Critical notes on actinoscirpus, bolboschoenus, isolepis, phylloscirpus and amphiscirpus (Cyperaceae). *Kew Bulletin*, 169-178.

Gustafsson, M. (1996). Spectroscopic Studies of Tissue using Near-Infrared Raman Microscopy. Lund Reports in Atomic Physics.

Har, N. P., Irzaman, I., and Irmansyah, I. (2019). Crystallinity and electrical properties of silicon dioxide (SiO_2) from rice straw. *AIP Conference Proceedings,* AIP Publishing.

Hartley, S. E., Fitt, R. N., McLarnon, E. L., and Wade, R. N. (2015). Defending the leaf surface: intra-and inter-specific differences in silicon deposition in grasses in response to damage and silicon supply. *Frontiers in Plant Science. 6*, 35.

Holm, L., Pancho, J. V., Herberger, J. P., and Plucknett, D. L. (1979). *A geographical atlas of world weeds,* John Wiley and Sons. the East-West Center by the University Press of Hawaii.

Holmquist, S. (1961). Conversion of quartz to tridymite. *Journal of the American Ceramic Society. 44*(2), 82-86.

Hornung, P. (2018). *Brazilian yam and turmeric native starches: characterization, modification and application*, Department of Food and Human Nutritional Sciences, Food Engineering Winnipeg.

Hossain, S. S., Mathur, L., and Roy, P. (2018). Rice husk/rice husk ash as an alternative source of silica in ceramics: A review. *Journal of Asian Ceramic Societies. 6*(4), 299-313.

Huabcharoen, P., Wimolmala, E., Markpin, T., and Sombatsompop, N. (2017). Purification and characterization of silica from sugarcane bagasse ash as a reinforcing filler in natural rubber composites. *BioResources. 12*(1), 1228-1245.

Ibrahim, I., Yunus, S., and Hashim, M. (2013). Relative performance of isopropylamine, pyrrole and pyridine as corrosion inhibitors for carbon steels in saline water at mildly elevated temperatures. *International Journal of Scientific & Engineering Research. 4*(2), 1-12.

Imtiaz, M., Rizwan, M. S., Mushtaq, M. A., Ashraf, M., Shahzad, S. M., Yousaf, B., and Mehmood, S. (2016). Silicon occurrence, uptake, transport and mechanisms of heavy metals, minerals and salinity enhanced tolerance in plants with future prospects: a review. *Journal of Environmental Management. 183*, 521-529.

Int, C. q. s. (2019). Silicon Dioxide (Fused Quartz) Sputtering Targets and Applications. Retrieved from https://www.qsiquartz.com/silicon-dioxide-fused-quartz-sputtering -targets-and-applications/.

Irzaman, Oktaviani, N., and Irmansyah. (2018). Ampel bamboo leaves silicon dioxide (SiO_2) extraction. *IOP Conference Series: Earth and Environmental Science. 141*, 012014.

Jamil, N. H. and N. S. M. Zarib (2019). Extraction of silica from rice husk via acid leaching treatment. *European Proceedings of Social and Behavioural Sciences*.

Jinadasa, K., Tanaka, N., Mowjood, M., and Werellagama, D. (2006). Effectiveness of Scirpus grossus in treatment of domestic wastes in a constructed wetland. *Journal of Freshwater Ecology. 21*(4), 603-612.

Jinadasa, K., Tanaka, N., Mowjood, M., and Werellagama, D. (2006). Free water surface constructed wetlands for domestic wastewater treatment: a tropical case study. *Chemistry and Ecology. 22*(3), 181-191.

Ju, S., Wang, L., Zhang, C., Yin, T., and Shao, S. (2017). Alleviatory effects of silicon on the foliar micromorphology and anatomy of rice (Oryza sativa L.) seedlings under simulated acid rain. *PloS One. 12*(10), e0187021.

Jungho, J.-H., 이정호, 이광렬, Mehmet Emin Kilic (2021). KIST Virtual Analysis Center : User's Manual. Retrieved from https://wikidocs.net/book/4915.

Jusnes, K. F., Tangstad, M., and Ringdalen, E. (2018). Phase transformations from quartz to cristobalite. Extraction 2018: *Proceedings of the First Global Conference on Extractive Metallurgy, Springer*, 717-727.

Kaiser, M. and G. Knör (2015). Synthesis, characterization, and reactivity of functionalized trinuclear iron–sulfur clusters–A new class of bioinspired hydrogenase models. *EuropeanJournal of Inorganic Chemistry*. (25), 4199.

Kantawanichkul, S., Somprasert, S., Aekasin, U., and Shutes, R. B. E. (2003). Treatment of agricultural wastewater in two experimental combined constructed wetland systems in a tropical climate. *Water Science and Technology. 48*(5), 199-205.

Key-Schwartz, R. J., Baron, P. A., Bartley, D. L., Rice, F. L., and Schlecht, P. C. (2003). *Chapter R, Determination of airborne crystalline silica. NIOSH Manual of Analytical Methods*, 4th ed., 3rd Suppl. Cincinnati, OH: US Department of Health and Human Services, Public Health Service, Centers for Disease Control and Prevention, National Institute for Occupational Safety and Health, DHHS (NIOSH) Publication, (2003-154).

Khalifa, M., Hajji, M., and Ezzaouia, H. (2012). Impurity removal process for high-purity silica production by acid leaching. *European Physical Journal Web of Conferences, EDP Sciences. 29*, 00014.

Khan, A., Khan, A. L., Muneer, S., Kim, Y.-H., Al-Rawahi, A., and Al-Harrasi, A. (2019). Silicon and salinity: Crosstalk in crop-mediated stress tolerance mechanisms. *Frontiers in Plant Science. 10*, 1429.

Kim, S., Park, J. Y., Gu, Y. M., Jang, I.-S., Park, H., Oh, K. K., and Chun, J. (2021). Eco-friendly and facile synthesis of size-controlled spherical silica particles from rice husk. *Nanoscale Advances. 3*(24), 6965-6973.

Kosmachev, P., Vlasov, V., and Skripnikova, N. (2017). Technological Aspects of Obtaining SiO2 Nanoparticles. *American Institute of Physics Conference Proceedings. 1800*(1), 020016.

Kostermans, A., Wirjahardja, S., and Dekker, R. (1987). The weeds: description, ecology and control. *Weeds of Rice in Indonesia*. 24-565.

Kuhlmann, A. (1963). The second most abundant element in the earth's crust: Frank J. Tone Award Address. *Journal of The Minerals, Metals and Materials Society. 15*(7), 502-505.

Kumar, S., Soukup, M., and Elbaum, R. (2017). Silicification in grasses: variation between different cell types. *Frontiers in Plant Science. 8*, 438.

Le Pevelen, D. (2010). Small molecule X-ray crystallography, theory and workflow. encyclopedia of spectroscopy and spectrometry, *Encyclopedia of Spectroscopy and Spectrometry*. 624-639.

Lee, T., Othman, R., and Yeoh, F.-Y. (2013). Development of photoluminescent glass derived from rice husk. *Biomass and Bioenergy. 59*, 380-392.

Li, J., Luo, G., He, L., Xu, J., and Lyu, J. (2018). Analytical approaches for determining chemical oxygen demand in water bodies: a review. *Critical Reviews in Analytical Chemistry. 48*(1), 47-65.

Li, L., Liao, L., Ding, Y., and Zeng, H. (2017). Dithizone-etched CdTe nanoparticles-based fluorescence sensor for the off–on detection of cadmium ion in aqueous media. *Royal Society of Chemistry Advances. 7*(17), 10361-10368.

Liang, Y., Ouyang, J., Wang, H., Wang, W., Chui, P., and Sun, K. (2012). Synthesis and characterization of core–shell structured SiO_2@ YVO_4: Yb^{3+}, Er^{3+} microspheres. *Applied Surface Science. 258*(8), 3689-3694.

Liou, T.-H. (2004). Preparation and characterization of nano-structured silica from rice husk. *Materials Science and Engineering: A. 364*(2), 313-323.

Lu, H. and K.-b. Liu (2003). Phytoliths of common grasses in the coastal environments of southeastern USA. *Estuarine, Coastal and Shelf Science. 58*(3), 587-600.

Maddalena, R., Hall, C., and Hamilton, A. (2019). Effect of silica particle size on the formation of calcium silicate hydrate [CSH] using thermal analysis. *Thermochimica Acta. 672*, 142-149.

Majrashi, A., Bakar, B. B., Khandaker, M. M., Boyce, A. N., and Muniandy, S. (2013). Fractal analysis of rhizome growth patterns of Scirpus grossus L. on peat and paddy soils. *Bulgarian Journal of Agricultural Science. 19*(6), 1319-1326.

Manurung, R., Siregar, H. d., and Zuhri, R. R. S. (2019). Synthesis and characterization of K-Silica catalyst based bamboo-leaves for transesterification reaction. *American Institute of Physics Conference Proceedings. 2085*(1), 020069.

Market, D. b. (2021). Global Rice Husk Ash Market – Industry Trends and Forecast to 2028. from https://www.databridgemarketresearch.com/reports/global-rice-husk-ash-market.

Matori, K., Haslinawati, M., Wahab, Z., Sidek, H., Ban, T., and Ghani, W. (2009). Producing amorphous white silica from rice husk. *MASAUM Journal of Basic and Applied Sciences. 1*(3), 512-515.

Merck (2021). Water for COD - Chemical Oxygen Demand. Retrieved from https://www.merckmillipore.com/TH/en/water-purification/learning-centers/applications/environment-water-analysis/cod/CLqb.qB.BIMAAAFAZwsQWTdi,nav?ReferrerURL=https%3A%2F%2Fwww.google.com%2F and bd=1.

Miller, S. (2021). 4 Ways Nitrogen Benefits Plants and How to Spot Deficiencies. Retrieved from https://www.foodcycler.com/post/4-ways-nitrogen-benefits-plants-how-to-spot-deficiencies.

Mitani, N., Ma, J. F., and Iwashita, T. (2005). Identification of the silicon form in xylem sap of rice (Oryza sativa L.). *Plant and Cell Physiology. 46*(2), 279-283.

Mohan, V. M., Shimomura, M., and Murakami, K. (2012). Improvement in performances of dye-sensitized solar cell with SiO_2-coated TiO_2 photoelectrode. *Journal of Nanoscience and Nanotechnology. 12*(1), 433-438.

Montazeri-Pour, M., Ataie, A., and Nikkhah-Moshaie, R. (2008). Synthesis of nano-crystalline barium hexaferrite using a reactive co-precipitated precursor. *IEEE Transactions on Magnetics. 44*(11), 4239-4242.

Mowla, D., Karimi, G., and Ostadnezhad, K. (2008). Removal of hematite from silica sand ore by reverse flotation technique. *Separation and Purification Technology. 58*(3), 419-423.

Mukashev, B., Abdullin, K. A., Tamendarov, M., Turmagambetov, T., Beketov, B., Page, M., and Kline, D. (2009). A metallurgical route to produce upgraded silicon and monosilane. *Solar Energy Materials and Solar Cells. 93*(10), 1785-1791.

Nash, D. A. H., Abdullah, S. R. S., Hasan, H. A., Idris, M., Othman, A. R., Al-Baldawi, I. A., and Ismail, N. I. (2020). Utilisation of an aquatic plant (Scirpus grossus) for phytoremediation of real sago mill effluent. *Environmental Technology and Innovation. 19*, 101033.

Nayak, P. and A. Datta (2021). Synthesis of SiO2-nanoparticles from rice husk ash and its comparison with commercial amorphous silica through material characterization. *Silicon. 13*(4), 1209-1214.

Nayak, P. P., Nandi, S., and Datta, A. K. (2019). Comparative assessment of chemical treatments on extraction potential of commercial grade silica from rice husk. *Engineering Reports. 1*(2), e12035.

Norsuraya, S., Fazlena, H., and Norhasyimi, R. (2016). Sugarcane bagasse as a renewable source of silica to synthesize Santa Barbara Amorphous-15 (SBA-15). *Procedia Engineering. 148*, 839-846.

Nuruddin, M. F., Saad, S., Shafiq, N., and Ali, M. (2016). Effect of Pretreatment Soaking Duration to Characteristic of Ultrafine Treated Rice Husk Ash (UFTRHA) as Supplementary Cementing Material (SCM). *Procedia Engineering. 11*, 7596-7600.

Odunlami, O. A., Agboola, O., Odiakaose, E. O., Olabode, O. O., Babalola, O., Abatan, O. G., and Owoicho, I. (2022). Treatment of Contaminated Water from Niger Delta Oil Fields with Carbonized Sisal Fibre Doped with Nanosilica from Ofada Rice Husk. *Journal of Ecological Engineering. 23*(9), 297–308.

Park, K., Kim, Y., and Lee, K. J. (2019). Analysis of deuterated water contents using FTIR bending motion. *Journal of Radioanalytical and Nuclear Chemistry. 322*(2), 487-493.

Pauling, L. (1960). *The nature ofthe chemical bond*. Cornell University Press, Ithaca, NY. 6.

Phomketjan, S. and T. Wongprayoon (2020). *Environmentally friendly dehumidifying product using silica extracted from bamboo leaves*. Rajamangala University of Technology Phra Nakhon, Bangkok.

Piperno, D. R. and H.-D. Sues (2005). Dinosaurs dined on grass. *Science. 310*(5751), 1126-1128.

Popovich, A., Nikiforov, P., Onishchenko, D., Tsvetnikov, A., and Kuryavyi, V. (2008). Preparation of nanodispersed silicon powder for implementing anodic composite matrices based on C-Si systems. *Theoretical Foundations of Chemical Engineering. 42*(5), 603-605.

Prabha, S., Durgalakshmi, D., Rajendran, S., and Lichtfouse, E. (2021). Plant-derived silica nanoparticles and composites for biosensors, bioimaging, drug delivery and supercapacitors: a review. *Environmental Chemistry Letters. 19*(2), 1667-1691.

Pratt, K. (2015). *Exposure Assessment to Respirable Crystalline Silica Particles Durring Airfield Maintenance Concrete Operations*. Montana Tech of the University of Montana, United States.

Radzali, O., Farah, J., and Pinang'MALAYSIA. 2011. Development of Borosilicate Glass Using Rice Straw Ash, *Journal of Microscopy*. *7*, 181-184.

Raman, V., Parashar, V., and Dhakate, S. (2002). Synthesis of silicon carbide whiskers from substituted silicon alkoxides and rayon fibres. *Journal of Sol-gel Science and Technology. 25*, 175-179.

Rashid, I., Daraghmeh, N. H., Al Omari, M. M., Chowdhry, B. Z., Leharne, S. A., Hodali, H. A., and Badwan, A. A. (2011). Magnesium silicate. Profiles of drug substances, excipients and related methodology, *Profiles of Drug Substances, Excipients and Related Methodology*. 36, 241-285.

Reig, F. B., Adelantado, J. G., and Moreno, M. M. (2002). FTIR quantitative analysis of calcium carbonate (calcite) and silica (quartz) mixtures using the constant ratio method. Application to geological samples. *Talanta. 58*(4), 811-821.

Rimstidt, J. D. and H. Barnes (1980). The kinetics of silica-water reactions. *Geochimica et Cosmochimica Acta. 44*(11), 1683-1699.

Salavati-Niasari, M. and J. Javidi (2012). Sonochemical synthesis of silica and silica sulfuric acid nanoparticles from rice husk ash: a new and recyclable catalyst for the acetylation of alcohols and phenols under heterogeneous conditions. *Combinatorial Chemistry & High Throughput Screening. 15*(9), 705-712.

Saliba, N., Yang, H., and Finlayson-Pitts, B. (2001). Reaction of gaseous nitric oxide with nitric acid on silica surfaces in the presence of water at room temperature. *The Journal of Physical Chemistry A. 105*(45), 10339-10346.

Savchenko, D., Vorliček, V., Kalabukhova, E., Sitnikov, A., Vasin, A., Kysil, D., Nazarov, and A. (2017). Infrared, raman and magnetic resonance spectroscopic study of SiO2:C nanopowders. *Nanoscale Research Letters. 12*(1), 1-12.

Setiadji, S., Sundari, C. D. D., Lala, E., Nurbaeti, D. F., Novianti, I., Suhendar, D., and Ivansyah, A. L. (2018). The increased use value of bamboo leaves as silica source for t-type zeolite synthesis. *Materials Science, Engineering and Chemistry Web of Conferences. 197*, 05003.

Shiva, M., Golmohammadi, M., and Nouroozi, F. (2023). Extraction of silica from rice husk for rubber-cord adhesion systems of tire industry. *Biomass Conversion and Biorefinery. 14*(15), 17717-17729.

Simpson, D. A., Muasya, A. M., Alves, M. V., Bruhl, J. J., Dhooge, S., Chase, M. W., and Hodkinson, T. R. (2007). Phylogeny of Cyperaceae based on DNA sequence data–a new rbcL analysis. Aliso: A, *Journal of Systematic and Floristic Botany. 23*(1), 72-83.

Souri, Z., Khanna, K., Karimi, N., and Ahmad, P. (2021). Silicon and plants: current knowledge and future prospects. *Journal of Plant Growth Regulation. 40*, 906-925.

Tangahu, B. V. (2016). Growth rate measurement of scirpus grossus plant as preliminary step to apply the plant in wastewater treatment using reedbed system. *Journal of Civil Engineering and Environmental Sciences. 5*(6), 1000192.

Tangahu, B. V., Ningsih, D. A., Kurniawan, S. B., and Imron, M. F. (2019). Study of BOD and COD removal in batik wastewater using Scirpus grossus and Iris pseudacorus with intermittent exposure system. *Journal of Ecological Engineering. 20*(5), 130–134.

Terzioğlu, P., Yucel, S., Rabagah, T. M., and Özçimen, D. (2013). Characterization of wheat hull and wheat hull ash as a potential source of SiO_2. *BioResources. 8*(3), 4406-4420.

Tilli, M. and A. Haapalinna (2020). Properties of silicon. Handbook of silicon based MEMS materials and technologies, *Micro and Nano Technologies*, 3-17.

Tipsotnaiyana, N., Jarupan, L., and Pechyen, C. (2012). Synthesized silica powder from rice husk for printing raw materials application. *Advanced Materials Research. 506*, 218-221.

TOGWT (2014, 2022 21 Frebruary). Automotive Silica Coatings. Retrieved from http://togwt1980.blogspot.com/2014/10/automotive-silica-coatings.html.

Trompowsky, P. M., de Melo Benites, V., Madari, B. E., Pimenta, A. S., Hockaday, W. C., and Hatcher, P. G. (2005). Characterization of humic like substances obtained by chemical oxidation of eucalyptus charcoal. *Organic Geochemistry. 36*(11), 1480-1489.

Tubaña, B. S. and J. R. Heckman (2015). Silicon in soils and plants. Silicon and Plant Diseases, 7-51.

Wise, N. (2012). Why Your Plants Need Phosphorus: Advantages And Disadvantages. Retrieved. Retrieved from https://www.holganix.com/.

Wu, B., Sun, T., You, Y., Meng, H., Morales, D. M., Lounasvuori, M., and Hu, B. (2023). *In Situ X‐ray Absorption Spectroscopy of Metal/Nitrogen‐doped Carbons in Oxygen Electrocatalysis*. Angewandte Chemie International Edition: e202219188.

Wu, C. F., Wei, T. R., Sun, F. H., and Li, J. F. (2017). Nanoporous PbSe–SiO_2 thermoelectric composites. *Advanced Science. 4*(11), 1700199.

Wylezich, B. (2022). Silicon in Electronics and Casting Applications. Retrieved from https://www.thomasnet.com/articles/chemicals/Silicon-Electronics-Casting-Applications/.

Yalcin, N. and V. Sevinc (2001). Studies on silica obtained from rice husk. *Ceramics International. 27*(2), 219-224.

Yan, F., Jiang, J., Chen, X., Tian, S., and Li, K. (2014). Synthesis and characterization of silica nanoparticles preparing by low-temperature vapor-phase hydrolysis of SiCl4. *Industrial & Engineering Chemistry Research. 53*(30), 11884-11890.

Yu, H., Du, C., Huang, Q., Yao, X., Hua, Y., Zhang, W., and Liu, H. (2018). Effects of extraction methods on anti-mould property of bamboo strips. *BioResources. 13*(2), 2658-2669.

Zhang, Y., Du, J., Zhang, F., Yu, Y., and Zhang, J. (2011). Chemical characterization of humic substances isolated from mangrove swamp sediments: The Qinglan area of Hainan Island, China. *Estuarine, Coastal and Shelf Science. 93*(3), 220-227.

Zhou, M., Ma, J., Wang, D., and Chen, W. (2022). Epidemiological study of respiratory diseases among dust exposed workers. *Encyclopedia of Respiratory Medicine*, 438-449.

Zurowski, W., Zepchło, J., Krzyzak, A., Gevorkyan, E., Rucki, M., Siek, E., and Białkowska, A. (2021). Wear resistance Si of the glass-fiber reinforced polymer composite with the addition of quartz filler, *Materials. 14*(14), 3825.

APPENDIX

APPENDIX

RAW MATERIALS AND FINISHED PRODUCT

Initial raw materials for SiO_2 synthesis

Untreated and acid-treated samples before calcination

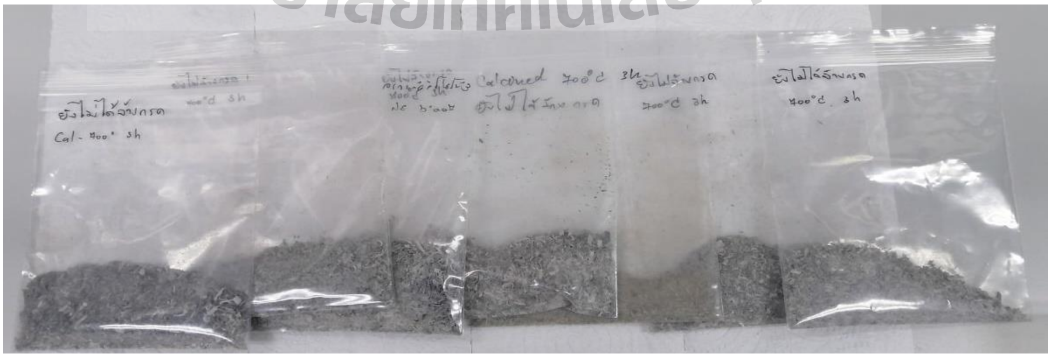

Untreated acid sample after calcined at 700°C 3h

Sediment from samples treated with acid after calcined at 700°C 3h

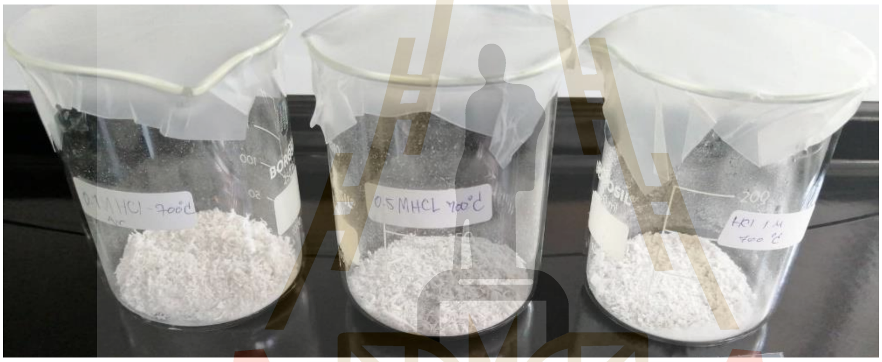

Ash powders from samples treated with acid after calcined at 700°C 3h

Ash powders from samples treated with acid after calcined at 700°C 3h

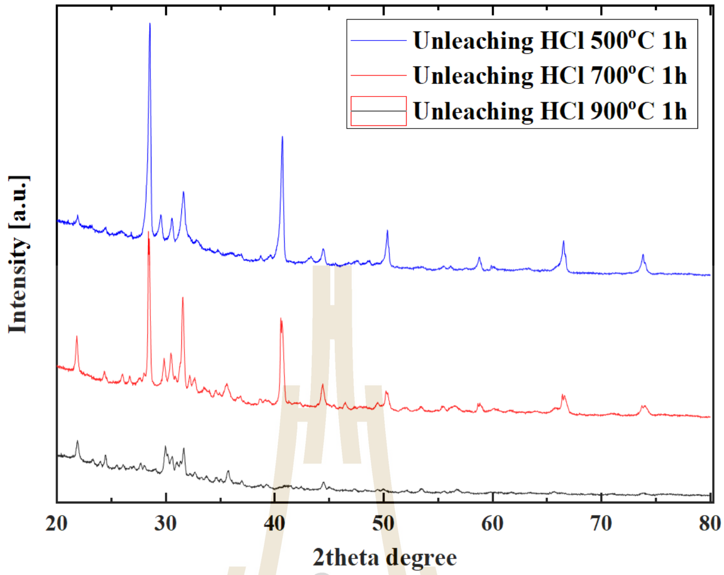

XRD spectra of unleaching samples via employing calcined at 500, 700, and 900°C

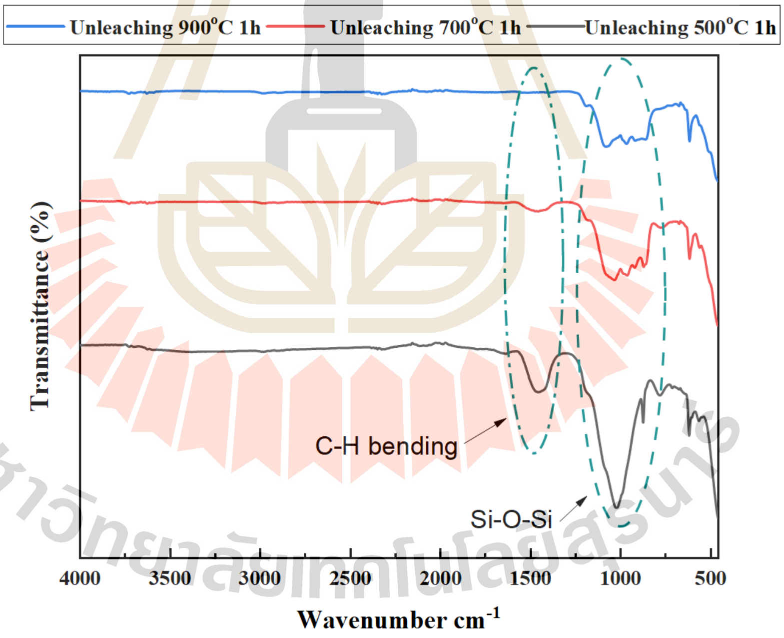

FTIR results of unleaching samples via employing calcined at 500, 700, and 900°C

The XRF results of the mass of SiO_2 in the samples of Un-leaching HCl-500°C, Un-leaching HCl-700°C and Un-leaching HCl-900°C.

Samples	Mass fraction of element oxide									
	SiO_2	K_2O	CaO	P_2O_5	Fe_2O_3	MnO_2	SO_3	MgO	Na_2O	Cl
Un-leaching calcination at 500°C	18.51	32.23	38.78	-	-	6.72	-	-		3.56
Un-leaching calcination at 700°C	22.15	30.27	35.55	-	-	6.61	-	-	-	5.30
Un-leaching calcination at 900°C	34.39	16.06	38.75	-	-	9.44	-	-	-	0.49

The XRF results of the mass of SiO_2 in the samples of 1M HCl boiling at 60°C, 1M HCl boiling at 70°C, and 1M HCl boiling at 90°C

Samples	Mass fraction of element oxide									
	SiO_2	K_2O	CaO	P_2O_5	Fe_2O_3	MnO_2	SO_3	MgO	Na_2O	Cl
1M HCl boiling at 60°C	90.07	1.23	2.53	2.63	0.52	0.38	0.08	0.71	1.84	0.001
1M HCl boiling at 70°C	91.02	1.53	3.99	1.83	0.40	0.40	0.02	0.18	0	0.03
1M HCl boiling at 90°C	96.24	0.32	0.24	1.08	0.03	0.07	0.32	-	-	-

The percentages of elemental oxide components in all samples derived from AGL ash via HNO_3 etching

Samples	Mass fraction of element oxide									
	SiO_2	K_2O	CaO	P_2O_5	Fe_2O_3	MnO_2	SO_3	MgO	Na_2O	Cl
LS-HNO_3 0.1M	92.02	0.37	3.62	2.92	0.53	0.55	-	-	-	-
LS-HNO_3 0.5M	93.47	0.46	2.55	2.52	0.48	0.47	0.07	-	-	-
LS-HNO_3 1M	90.45	1.46	5.57	0.52	0.32	0.79	0.89	-	-	-
LS-HNO_3 5M	95.60	0.61	2.95	-	0.17	0.58	0.10	-	-	-

The cost of materials used in the experiment

Materials	Price 1	Price 2	Price 3
Actinoscirpus grossus 1kg	5 B	10 B	15 B
Acid	Price of acid		
37%HCl (2.5l)	896 B		
70%HNO_3(2.5l)	1200 B		
Furnace size 8l	5kW		

The cost of preparing 2 grams of silica for the experiment with 99.8% SiO_2

Materials	Price 1	Price 2	Price 3
Actinoscirpus grossus (50g)	0.25	0.5	0.75
Acid / time	33	33	33
Electricity cost	60	60	60
Total cost (B)	93.25	93.5	93.75

CURRICULUM VITAE

Name-Surname : Anuchit Sawangprom

Date of Birth : 6 June 1992

Province : Mahasarakham

Education : B.S. (Physics), Khonkean university, Khonkean (2014).
M.S (Physics), Khonkean university, Khonkean (2018).

Scholarship : Ph.D. scholarship from External Grants and Scholarships for Graduate Students, Suranaree university of technology, Nakhon Ratchasima.

Publications:

1. **A. Sawangprom**, K Duangsa and A Tangtrakarn, “Effect of calcination temperature on the conductivity of Sm and Cu co-doped ceria”, Conference Series. 2018. IOP Publishing.

International Conferences:

1. **A. Sawangprom**, T. Jampreecha, and S. Maensiri, “Structure and Characterization of High Purity Amorphous SiO_2 Nanoparticles Derived from Greater Club Rush”, The 3rd Materials Research Meeting (MRM2023) The 24th IUMRS-International Conference in Asia (IUMRS-ICA2023), Kyoto, Japan, 2023.